Università degli Studi di Milano

Dipartimento di Chimica

Ph.D. in Chemistry – XXIX Cycle

DISORDER AT THE NANOSCALE IN PEROVSKITE TITANATES AND DOPED CERIA: MULTIPLE APPROACHES TO MODELLING TOTAL SCATTERING DATA

(CHIM/02, CHIM/03)

Stefano Checchia

R10437

Supervisor: Dr. Marco Scavini

Coordinator: Prof. Emanuela Licandro

A.A. 2016-2017

Table of Contents

Abstract

DISORDER AT THE NANOSCALE IN PEROVSKITE TITANATES AND DOPED CERIA: MULTIPLE APPROACHES TO MODELLING TOTAL SCATTERING DATA

Crystal structures can take a number of forms and their relationship with the physics of a solid lends itself to an even greater number of interpretations. Ferroelectricity, for example, can be predicted to occur in certain symmetries, but sometimes it can be hidden in the response to an electric field, in a peculiar electron- or nuclear-spin resonance, in the unfolding of a phase transition, or else. In any of these cases, the emergence of ferroelectricity is intimately related to subtle changes in the atomic positions with respect to a high-symmetry parent structure. As is the case with many other physical properties, this often implies that the crystal structure is disordered *locally* (as opposed to *on average* or *long-range*), but the magnitude and the time- and length-scales of disorder can vary dramatically between different materials.

This work combines multiple X-ray and neutron powder diffraction techniques to try to capture the most of the structural complexity hidden in the bulk of materials. First, reciprocal-space analysis by the Rietveld method allowed drawing the crystallographic phase diagram of a novel perovskite solid solution, praseodymium-doped strontium titanate (SPTO). SPTO is a perovskite that combines a centrosymmetric antiferrodistortive (AFD) structure and a large, diffuse dielectric response at room temperature, prompting the question of whether AFD and ferroelectric (FE) distortions coexist in the material. Subsequently, the Pair Distribution Function (PDF) of SPTO, representing the instantaneous spatial arrangement of the atoms in the material, was analysed using multiple approaches. X-ray PDF was fitted with structural models obtained by evaluating possible polar and rotational distortions of the cubic perovskite phase. The most accurate, a tetragonal structure derived from the long-range phase, showed a huge AFD distortion that could also be consistent with a local FE mode. To get a better insight into the local structure, neutron PDF data were collected and modelled by i) fitting the distorted tetragonal model over successive ranges in real space ('box-car' refinements) and ii) atomistic simulations using the Reverse Monte Carlo (RMC) method. This led to a model in which FE

distortion caused by Pr-doping at the perovskite A-site spreads to the AFD framework of octahedra, resulting in distorted coordination of both A and B cations.

Neutron PDF data of undoped strontium titanate was also used in the development of another approach to PDF modelling, in which structural models representing a unique soft-mode distortion are evaluated statistically against the experimental neutron PDF. This symmetry-adapted approach evidenced that four soft modes among those suggested by theoretical phonon dispersion are active distortions in $SrTiO_3$, and have signatures in the local structure determined experimentally. This approach is aimed at obtaining an unbiased local structural model of strontium titanate, in that symmetry lowerings are inferred directly from the amplitudes of the individual soft modes refined against the PDF instead of assessing the goodness of fit of an arbitrarily chosen model.

Whereas all these methods focused on a length scale of 10 Å (1 nm), the last approach to PDF modelling presented in this work studies the coherence length of lower-symmetry nanometric domains in a solid solution by evaluating structural parameters up to 600 Å (60 nm). Instead of titanates, though, this study involved yttrium-doped ceria: thanks to the extremely high structural coherence of crystalline ceria and owing to the high angular resolution of the instrument used, the data collected lend themselves very well to analysing the PDF well beyond the short range. The aim of this approach is to obtain a structural model for every slice of real space analysed, in order to describe in terms of order parameters how the local structure coalesces into the average crystallographic phase.

:Chapter 1:

Distortions in Perovskites

1.1 The perovskite structure of $SrTiO_3$

The perovskite structure is adopted by many solids of general formula ABX_3 and consists of a cubic close-packed array of cations of type A and twelve coordinated anions of type X, with layers stacking along the <111> direction. Cations of type B are six-coordinated by anions and occupy one quarter of the octahedral holes. Alternatively, the same structure can be visualized as a framework of corner-sharing BX_6 octahedra, with A cations occupying the 12-coordinated interstices (shaped as cuboctahedra). The A and B sites of the perovskite structure can accommodate a wide range of cations of varying size and charge. Consequently, there are astonishingly many perovskites; these include ternary oxides, fluorides, cyanides, halides, and sulfides of alkaline, alkaline-earth, and transition metals and rare-earths, mixed-occupancy double perovskites ($AA'BB'X_6$), and also metal-organic perovskites, like, for instance, $(CH_3NH_3)PbX_3$, in which the A site is populated by methylammonium molecules and X can be a iodide or a chloride (Clearfield, 1963; Peschel et al., 2000; Hoenle et al., 1988; De Jongh & Miedema, 1974). Only a handful of naturally occurring elements in the periodic table are not observed in atomic perovskite compounds: boron, beryllium, phosphorus, and all noble gases - though boron may be found as borohydride anion. Despite many feasible combinations of cations at the perovskite A and B sites, a guiding principle for structural stability for a given composition is expressed by the Goldschmidt tolerance factor τ (Goldschmidt, 1926):

$$\tau = \frac{r_A + r_X}{\sqrt{2}(r_B + r_X)}$$

Here r_A, r_B and r_X represent the ionic radii of the ions in the perovskite. Ionic radii are available as published by Shannon (1976) or can be obtained from bond-valence calculations (Brese & O'Keeffe, 1991; Lufaso and Woodward, 2001). The definition of τ follows from bond distance considerations in an ideally close-packed structure: the cell edge is two B-X bond distances long; the length of one face diagonal is two A-X bond distances, but it also equals the length of one edge times $\sqrt{2}$. Thus, τ measures the fit of the A cation into the cuboctahedral site for a given BO_6 framework: tolerance factors lower than 1 result from A cations smaller than the cuboctahedral interstice and, therefore, undercoordinated; values of τ greater than 1 correspond to a large A or a small B cation and may give rise to cation off-centering (Megaw, 1968; Zhong and Vanderbilt, 1995). Values of τ between 1.07 and 0.78 have been observed for perovskites (Woodward, 1997b). Already at $\tau \approx 1$, the structure tends to hexagonal polytypes, while near the lower limit the $FeTiO_3$ (ilmenite) type structure becomes favourable.

With the exception of Chapter 6, the main theme of this work is the structure of strontium titanate ($SrTiO_3$). Figure 1.1 shows its primitive cubic cell (space group *Pm*-3*m*, Z=1), as close to ideality as a perovskite can be (τ ~1.0). The A cation sits in the centre of the cube delimited by eight Ti atoms at the corners; in the setting used throughout this work, the six-coordinated

Ti atom is placed in the origin of the unit cell (0, 0, 0). Both the Sr and Ti sites (*1b* and *1a* in Wyckoff notation) are one-fold special positions, i.e. they lie on the highest-symmetry elements of the space group. O atoms lie in lower-symmetry special positions with multiplicity 3 (*3d*); therefore, three positions in the unit cell are independent by symmetry.

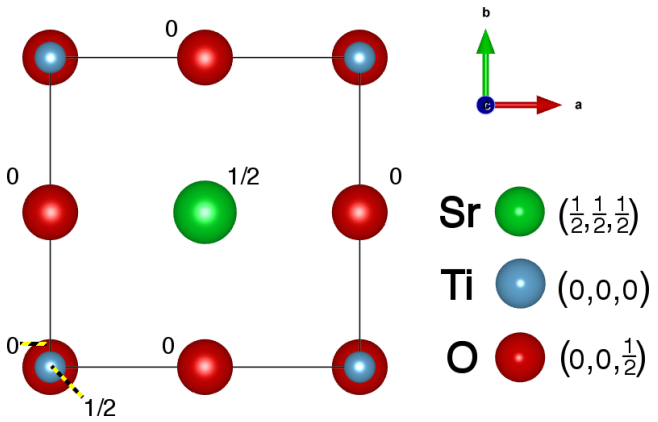

Figure 1.1: The cubic phase of the perovskite $SrTiO_3$. The numbers next to atoms are the respective fractional coordinates along the c-axis. All the structure drawings, in this chapter and in the following ones, were obtained using the program VESTA (Momma and Izumi, 2011).

Unlike many perovskite oxides, whose crystallographic structures deviate from simple cubic already at room temperature, the cubic structure of $SrTiO_3$ (τ ~1.0) persists down to 105 K temperature; below 105 K, the structure of $SrTiO_3$ is described by the centrosymmetric tetragonal space group *I*4/*mcm* (Z=4). As reported in Table 1.1, listing cell parameters and atomic positions for the two phases of $SrTiO_3$, there are two distinct O sites in the *I*4/*mcm* structure. An important distinction must be made between the *axial* O atoms of the octahedron (O1), i.e. those bonded to Ti along the *c*-axis, and *equatorial* O atoms (O2), i.e. whose bonds to Ti are parallel to the <110> direction and its equivalents. The O2 atom has no four-fold symmetry and its *x* coordinate is the only positional degree of freedom in tetragonal $SrTiO_3$.

Table 1.1: List of the atomic positions, site symmetries, and cell parameters for the cubic and for the tetragonal phases of strontium titanate. Cell parameters are taken from the structures published by Mitchell et al. (2000) and by Tsuda & Tanaka (1995).

	Cubic - *Pm*-3*m* (#221)					**Tetragonal - *I*4/*mcm* (#140)**				
	Z = 1; *a* = *b* = *c* = 3.9053 Å					*Z* = 4; *a* = *b* = 5.5110 Å; *c* = 7.7960 Å				
	Wyckoff	**Symmetry**	**x**	**y**	**z**	**Wyckoff**	**Symmetry**	**x**	**y**	**z**
Sr	*1b*	m-3m	0.5	0.5	0.5	*4b*	-42m	0	0.5	0.25
Ti	*1a*	m-3m	0	0	0	*4c*	4/m . .	0	0	0
O1	*3d*	4/m m . m	0	0	0.5	*4a*	422	0	0	0.25
O2	--	--	--	--	--	*8h*	m.2 m	*x* (~0.25)	*x*+0.5	0

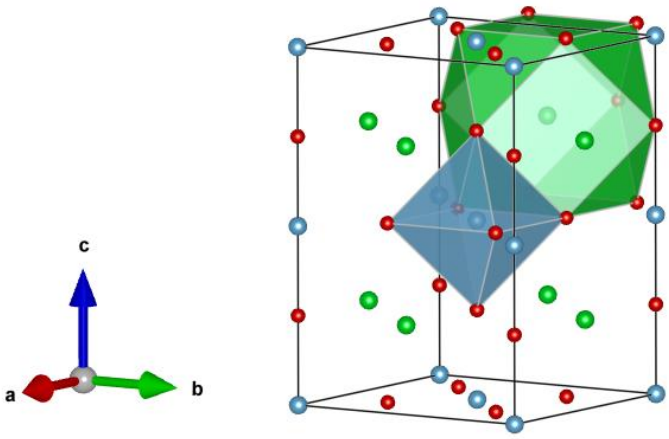

Figure 1.2: The tetragonal unit cell of $SrTiO_3$, showing the of the low-temperature phase. Ti atoms are in blue, Sr atoms are in green, O atoms are in red. One TiO_6 octahedron and one neighbouring SrO_{12} cuboctahedron are highlighted with solid faces.

1.2 Octahedral tilting

1.2.1 Overview

The phase transition from cubic to tetragonal structure in $SrTiO_3$ involves the doubling of the cell along the *c*-axis, while the tetragonal cell parameters *a* and *b* are taken as face diagonals of the parent cubic cell. A compact way to write the group-subgroup relation is the transformation matrix *P*, which relates the lattice parameters of the space groups *I*4/*mcm* and *Pm*-3*m*:

$$(a', b', c')_{I4|mcm} = P(a, b, c)_{Pm-3m}$$

$$P = \begin{pmatrix} 1 & 1 & 0 \\ -1 & 1 & 0 \\ 0 & 0 & 2 \end{pmatrix}$$

with no origin shift between the two groups. It can be demonstrated that the doubling of the unit cell along *c* is implied by the periodicity of the distortion correlating the supergroup *Pm*-3*m* and its subgroup *I*4/*mcm*. As shown in Figure 1.3, the displacement of the atom O2 causes the rigid rotation ('tilting') of TiO_6 octahedra about the *c*-axis, corresponding to the <001> direction. Conservation of the connectivity between corner-sharing octahedra requires that

neighbouring octahedra along the directions <100> and <010> (i.e. perpendicular to the rotation axis) rotate in opposite sense; along the rotation axis, successive octahedra are also tilted out of phase, so that a rotation by +5° (or -5°) is repeated every second octahedron along the *c*-axis. This precise tilt pattern determines the periodicity of the framework of *tilted* octahedra that defines uniquely the *I*4/*mcm* space group. Since this is one of the 23 fundamental tilt systems identified by Glazer (1972; 1975), tilt classification is presented in some detail in the next paragraph.

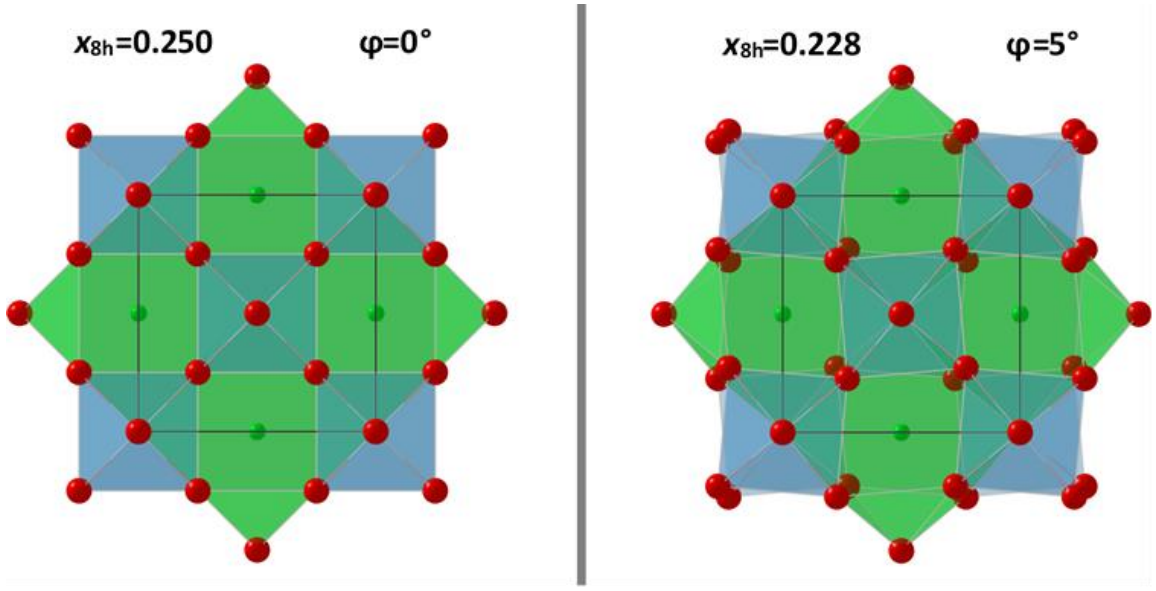

Figure 1.3: View along the c-axis of the tetragonal unit cell of strontium titanate (all octahedra and cuboctahedra highlighted with solid faces) in the absence of octahedral tilt (left panel) and after applying an arbitrary tilt angle of φ=5° (right panel).

Figure 1.3 also evidences that octahedral rotations leave the coordination environment of B cations unchanged while that of A cations is strongly distorted. This reflects not only that the more electronegative B atom forms B-X bonds stronger than A-X interactions, but also that octahedral tilt is linked to the undercoordination of A cations - as can be predicted for tolerance factor values lower than 1. Since the A cation is smaller than the cuboctahedral site provided by an ideal cubic packing, the framework of octahedra distorts so as to improve the anion coordination around the A cation, i.e. by shortening some A-O distances and lengthening some others. For instance, in the case of the tilt determining the *I*4/*mcm* symmetry, axial O atoms are fixed while two parallel planes of equatorial O atoms above and below the A atom are displaced as a result of octahedral rotations. While B-O distances are left unchanged, the 12 once-identical A-O distances split into four short, four long, and four intermediate distances; this results in a lower anion coordination or, in terms of bond-valence sum, an increase in the

average bond valence[1]. The four medium A-O distances alone determine a square-planar coordination of the A cation, while the four closest distances define a distorted tetrahedron with A-O distances and angles strongly dependent on tilt angle (Woodward, 1997b).

The relatively simple tilt pattern in the *I*4/*mcm* symmetry already reveals a considerable rearrangement in the coordination environment of the A cation. Tilting of the octahedra is in fact an important factor determining the long-range structure of perovskites. It was shown, most notably by Megaw (1967, 1973), that the distortion of a lower-symmetry perovskite ('hettotype') with respect to the ideal structure ('aristotype') can be broken down into three distinct contributions: cation displacements within the octahedra, distortion of the octahedra, and tilting of the octahedra. Cation displacements can be either ferroelectric (in-phase) or antiferroelectric (out of phase) and, like distortions of the octahedra, originate from electronic instabilities of the B cation (Woodward, 1997). Notable examples include the ferroelectric displacement of Ti and Nb in $BaTiO_3$ and $KNbO_3$, respectively (Shirane, 1957, 1954; Megaw, 1967) and octahedral distortions driven by the Jahn-Teller effect in $KCuF_3$ (Okazaki and Suemune, 1961). The effect of octahedral tilt is, however, predominant in the phase transitions of many perovskites, including $SrTiO_3$. But while octahedral tilt can be expected from basic geometrical considerations when synthesizing a perovskite compound, it is harder to predict what the exact A-site environment is going to be and, in turn, what tilt pattern this will generate.

1.2.2 Classification of tilt systems

This paragraph explains why the tilt pattern shown in Figure 1.3 implies the *I*4/*mcm* symmetry in $SrTiO_3$ and, more generally, which features of octahedral tilting influence space group symmetry. The relationship between long-range symmetry and pattern of octahedral rotations in perovskite compounds was first defined by Glazer and Megaw (1972) and subsequently systematized by Glazer (1972). This was later re-examined by Woodward (1997, 1997b) and by Howard and Stokes (1998), and it also served as a tool for predicting crystal structures of perovskite compounds with rigid-octahedra frameworks (Lufaso & Woodward, 2001; Barnes et al., 2006).

Glazer's classification is based on the decomposition of octahedral tilting into three components along the [100], [010], [001] pseudocubic axes. The amplitude of the component tilts along these axes are indicated, respectively, as *a*, *b*, *c*, for the general case in which three tilts are unequal; otherwise, letters are repeated if two tilts have the same amplitude. Each symbol has a superscript indicating the relative direction of tilting of neighbouring octahedra

[1] Though outside the scope of this work, the bond-valence method and its application to tilted-octahedra systems are discussed in great length by Barnes et al., (2006), Brown (1981, 1992), Lufaso & Woodward (2001), O'Keeffe (1989).

along an axis: i) "0", if the octahedra are not tilted; ii) "-", if the tilt angles have opposite sign; iii) "+", if the tilt angles have the same sign. The tilt systems allowed in Glazer's classification, including zero tilt (*Pm*-3*m*), are 23, each denoting a different space group. This follows from a geometrical evidence common to all tilt systems, which is exemplified by Figure 1.4. Tilting of the octahedra decreases the bond distances between octahedron centres perpendicular to the tilt axis (this will return with a vengeance in Chapter 3 in the evolution of the cell parameters of $SrTiO_3$, both undoped and doped with Pr). Since the distance between two B cations corresponds to a pseudo-cubic cell parameter, an increase in tilt angle along one specified direction (say, [001]) must be accompanied by cell shrinking in both perpendicular directions ([100], [010]). The extent of shrinking of each pseudocubic cell parameter is thus determined by the amplitude of tilt along that direction. The same tilt angle for two axes, for example, results in the corresponding cell parameters being equal; more generally, this shows how the crystal system of the compound (but not, at least directly, the actual value of the cell parameter) is related to the tilt pattern.

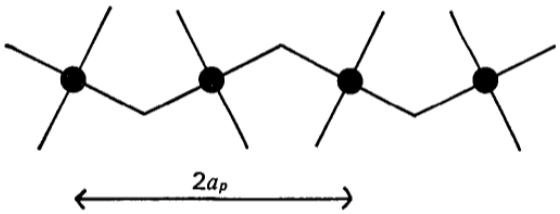

Figure 1.4: Schematic representation of the bonds between B cations along one direction perpendicular to the tilt axis. Figure from Glazer (1975).

An important consequence of the sense of rotation along an axis is that a 0 or + relation implies the existence of a mirror plane perpendicular to that axis (Glazer, 1972). Accordingly, $a^0a^0c^-$ and $a^0a^0c^+$ tilts require two mutually perpendicular mirror planes normal to *a* and *b*; this, combined with the two equal axis lengths due to a^0 tilts, describes tetragonal space groups (namely, *I*4/*mcm* and *P*4/*mbm* in the revised list by Woodward, 1997). Similarly, orthogonal axes can be inferred for the two-tilt systems $a^0b^+c^+$ and $a^0b^+b^+$, where the latter is also tetragonal by virtue of the equal tils along [010] and [001]. Two out-of-phase tilt components (- superscript), instead, require that the corresponding pseudo-cubic axes be inclined relative to each other (the demonstration can be found in Glazer, 1972), giving rise to monoclinic and rhombohedral space groups for two- and three-tilt systems.

It is now clear why the one-tilt, anti-phase tilt system of $SrTiO_3$, named $a^0a^0c^-$, invokes the space group symmetry *I*4/*mcm*. Importantly, all this can be identified by powder diffraction measurements. In fact, not only the repeat period of two octahedra determines the doubling of the unit cell along the corresponding directions of tilting (Figure 1.4), but also results in

different sets of superlattice reflections for different tilt systems, as rationalized by Glazer in his second paper[2] (1975). The most powerful consequence is that the Bragg reflections related to (+) tilts change completely from those arising from (-) tilts and, as discussed further in section 1.3, this relates to their origin at different critical points of the reciprocal space, thus, in different structural modes.

On top of this latter conclusion, Howard and Stokes (1998) re-examined the correspondence between tilt system and space group symmetry based on group-subgroup analysis. They found that only 15 of the 23 structures originally found by Glazer are uniquely generated by octahedral tilting (they are shown in Figure 1.5). Namely, they considered only the tilt systems attainable as linear combinations of six basic component tilts originating from the mixing of the three possible (+) one-tilt systems with the three analogous (-) tilts, or, in terms of representations, the 6-dimensional sum of the irreducible representations (irrep) M3+ and R4+ (Miller and Love, 1967).

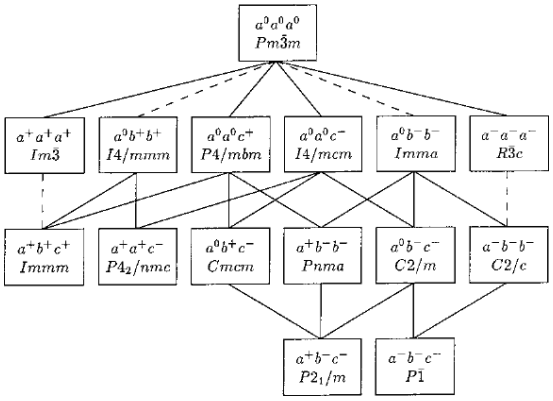

Figure 1.5: Figure from Howard and Stokes (1998). Diagram of the single-irrep, group-subgroup relations between the 15 isotropy subgroups of the aristotype Pm-3m. Dashed lines indicate which phase transitions are necessarily first-order.

Every possible phase transition between these 15 space group symmetries can be seen as the condensation of the 6-dimensional order parameter corresponding to one linear combination thus obtained. The main point here is that each subgroup of *Pm*-3*m* is defined by a subspace of the 6-dimensional order parameter space. Therefore, it can be shown that the representation of the *I*4/*mcm* space group is one-dimensional since it is obtained by a single component-tilt of the R4+ irrep; if this one-dimensional order parameter was directed along two or three axes, the resulting space groups would be *Imma* and *R*-3*c* (shown experimentally by inelastic neutron scattering, e.g. by Shirane and Yamada, 1969). The notation introduced by Howard and Stokes allows one to visualize at once dimensionality and direction of the order parameter; for these

[2] Note that the original attribution of space group (*F*4/*mmc*) and supercell (2×2×2) to the $a^0a^0c^-$ tilt pattern of $SrTiO_3$ made by Glazer in these papers (1972, 1975) was later rectified by Woodward (1997).

three space groups, respectively, the order parameters are (00000*c*), (0000*bb*), and (000*aaa*). This will be used again in the symmetry decomposition of $SrTiO_3$ presented in Chapter 5.

1.3 Other types of lattice instability

1.3.1 Soft modes

The diversity of physical properties in perovskites owes in many cases to two kinds of distortions from the cubic aristotype: octahedral tilts, which we just covered, and polar displacements of cations, which we cover below. In the previous section, octahedral tilting was considered only in terms of geometric distortion. Now it is convenient to think of structural distortions in terms of frequency of soft modes. Any kind of distortion is driven by the lattice instability with respect to certain soft modes associated with the centre point (Γ) or to boundary points (M, R, X) of the cubic Brillouin zone (Figure 1.6). It is useful to recall that a soft mode is a normal vibrational mode whose frequency tends to zero (i.e. it becomes unstable) as a phase transition is approached, and whose eigenvector contains both the atomic displacements relative to the lattice sites involved and the periodicity of the distortion through the lattice.

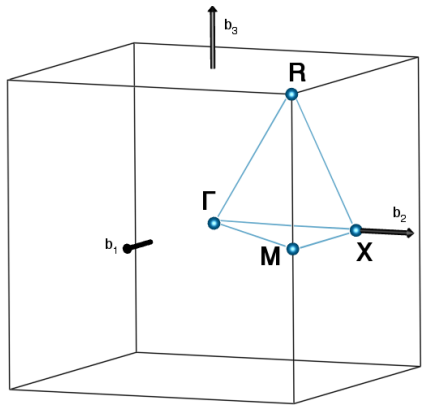

Figure 1.6: First Brillouin zone of a primitive cubic lattice, with the corresponding lattice vectors (b_1, b_2, b_3) and critical points (with wavevectors) Γ (0,0,0), R (½,½,½), M (½,½,0), X (0,½, 0). Created with VESTA (Momma & Izumi, 2011).

Above a phase transition, for example, a soft mode corresponds to the lowest-frequency phonon with the same symmetry. Vibrations slow down on cooling until the phonon frequency drops to zero. At this point, conventionally taken as the phase transition temperature (T_C), the atomic displacements prescribed by the eigenvector of the frozen mode become static. Below T_C, the frequency of lattice vibrations increases again, but the phonon now represents vibrations around the atomic positions of the lower-symmetry phase (Fleury, 1976). If the same transition is observed from the low-temperature side, the evolution of the structural distortion from static to dynamic is gauged by the amplitude of an order parameter going continuously to zero (for

example, octahedral tilt angle or ferroelectric displacement of a cation). Although there may be a discontinuity in the order parameter near T_C (partial first-order character), the existence of a temperature dependence of the order parameter for $T<T_C$ implies an overall second-order character of the phase transition.

1.3.2 Lattice instabilities in $SrTiO_3$

Having defined the general case for a second-order phase transition, we can describe in greater detail the possible distortions of the *Pm*-3*m* cubic perovskite. To introduce the irreducible representations of the distortions we use the notation introduced by Howard and Stokes (1998) and group-subgroup relations obtained using the program ISODISTORT (Campbell et al., 2006). A basic phonon dispersion curve for $SrTiO_3$ is shown in Figure 1.7. The two soft phonons transform like the R4+ and Γ4- irreducible representations. While the former phonon, a non-polar zone-boundary mode, has negative frequencies and is therefore static at zero temperature (hence the *I*4/*mcm* low-temperature structure of $SrTiO_3$), the latter, zone-centre mode never condenses into a long-range phase, so there is no matching phase transition. Low-frequency modes are also observed at the points M and X, namely, M3+ (64 cm^{-1}) and X5- (103 cm^{-1}).

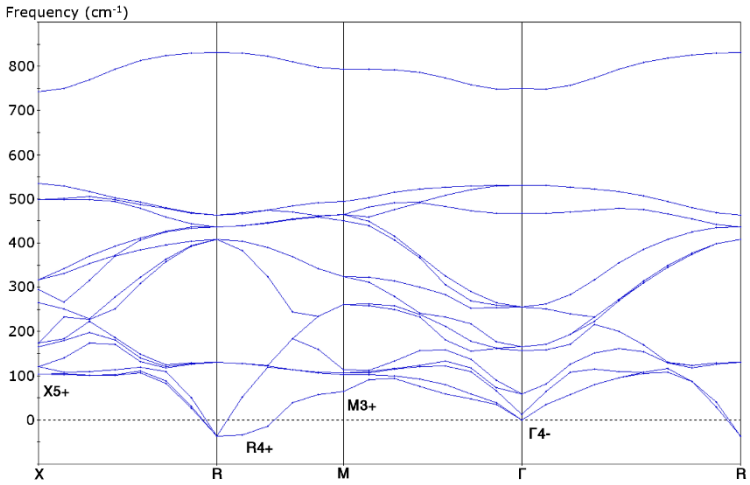

Figure 1.7: Zero-temperature phonon dispersion curve for $SrTiO_3$ calculated using CASTEP (Clark et al., 2005); the input structure was taken from Meyer et al (1978).

Ferroelectric (FE) displacements are associated with Γ-point phonon modes with wavevector (0,0,0): this implies that the displacement is repeated in every successive unit cell, and that the number of atoms in the unit cell is not changed by the would-be transition; hence, the unitary propagation period. The simplest displacive FE phase transition attainable in the cubic

perovskite involves the Γ4- soft mode with a one-dimensional order parameter[3] directed along one, two, or three pseudo-cubic axes [(a,0,0), (a,a,0), (a,a,a)]. This gives rise to the polar space groups *P*4*mm*, *Amm*2, and *R*3*m*, respectively, with atom displacements allowed along the [100], [110], or [111] directions with respect to parent the cubic cell. Figure 1.8 shows an example of FE displacement represented by the order parameter (a,a,a). Other phase transitions are possible within the Γ4- irrep, through two-dimensional order parameters (leading to the monoclinic *Pm*, *Cm*), or breaking all symmetry through a three-dimensional set of displacements (*P*1).

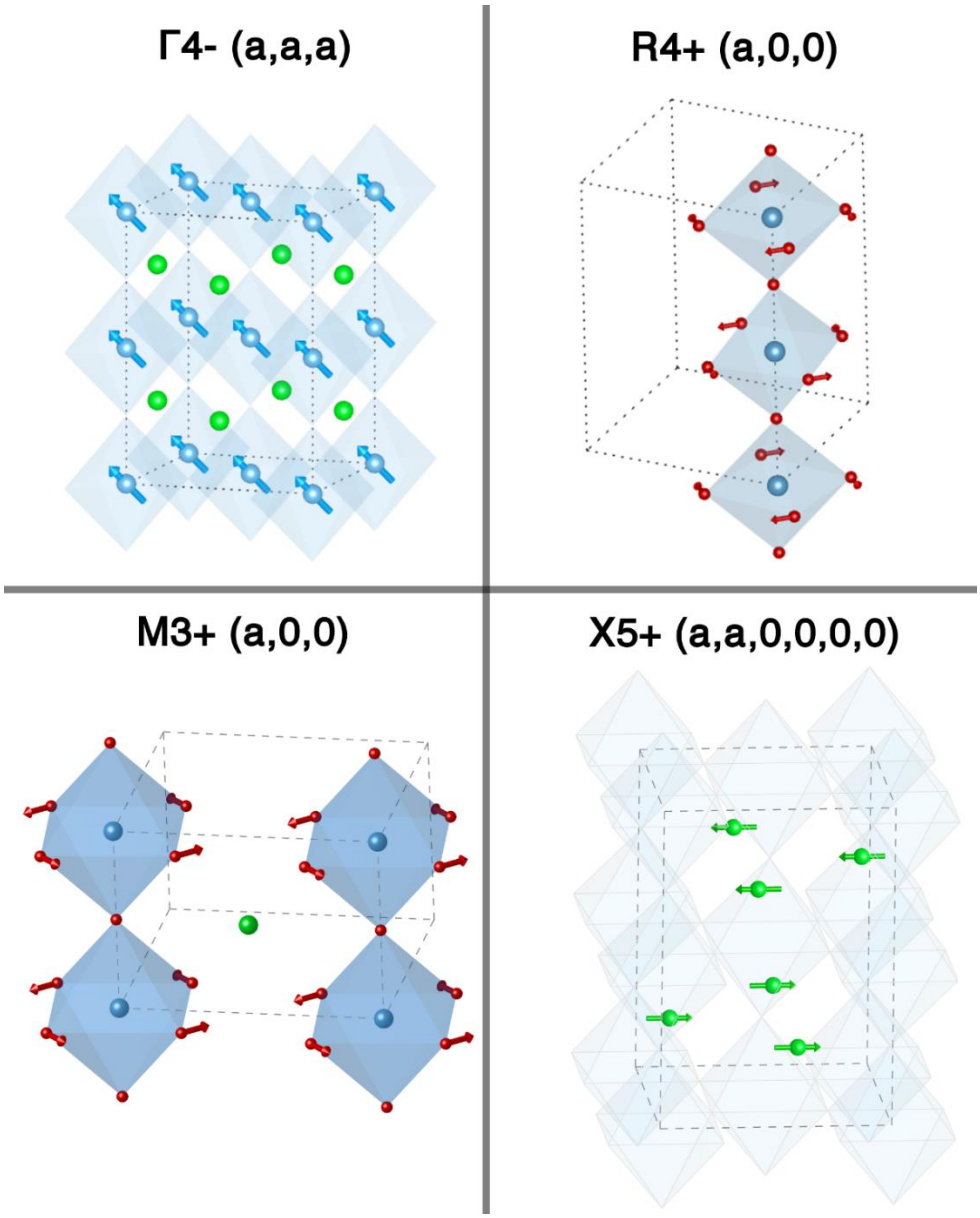

Figure 1.8: Schematic illustration of the lowest-frequency modes in $SrTiO_3$.

[3] A single magnitude of atom displacement indicated by the same letter for every component direction, in analogy with the tilt order parameters (paragraph 1.2.2). In this notation, a three-dimensional order parameter is (a,b,c).

The soft-mode distortion mediated by the R4+ irrep (Figure 1.8) corresponds to the octahedral tilt system $a^0a^0c^-$, which was discussed in great length in the previous section. This is the mode responsible for the phase transition in $SrTiO_3$ at 105 K and normally referred to as 'antiferrodistortive' (AFD) (Zhong and Vanderbilt, 1995). Note that the cell doubling brought about by octahedral tilt is also expressed by the wavevector (½,½,½). The low-frequency M3+ mode, which does not condense at any temperature in $SrTiO_3$, plays an important role in compounds with *Pnma* symmetry, the most recurring space group in perovskites. As shown in the M3+ panel of Figure 1.8, the octahedral tilts in two successive layers along the *c*-axis are in phase, described by the tilt system is $a^0a^0c^+$ as opposed to $a^0a^0c^-$. The last panel in Figure 1.8 shows the antiferroelectric (AFE) displacement of Sr atoms along a direction parallel to the cubic [110]. This mode belonging to the X5+ irrep is also important in the interplay between lattice instabilities in orthorhombic perovskites (see below).

The relationship between AFD and FE modes in perovskites has long been studied. The observation that AFD instability is not present in FE perovskites (e.g. $BaTiO_3$, $KNbO_3$) holds true in many cases, leading to the conclusion that the two types of instabilities compete with each other. This can be also expected by considering the opposite tendencies of undercoordinated and oversized A cations, respectively, toward octahedral tilting and cation off-centering (see section 1.2). Zhong and Vanderbilt (1995) showed by Monte-Carlo calculations that AFD and FE instabilities coexist in a very large number of perovskite compounds, and that in many cases - including $SrTiO_3$ - an AFD phase transition should be followed by a FE transition at lower temperature. By artificially switching the amplitudes of the soft FE and AFD modes in $SrTiO_3$, however, they demonstrated that the AFD and FE instabilities actually suppress each other. Namely, their results show that, in absence of the rival interaction, each mode would soften in milder conditions than experimentally observed: the AFD phase transition would occur at a higher temperature (about 130 K), while a FE phase transition, forbidden[4] in $SrTiO_3$, would be observed below 70 K. This picture was recently revisited by Aschauer and Spaldin (2014), who used density functional theory (DFT) to compute the energy gain due to a FE as a function of the amplitude of the AFD mode. The

[4] As to the FE phase transition in $SrTiO_3$, it was briefly mentioned that the zone-centre Γ mode softens but never condenses in $SrTiO_3$, resulting in the 'quantum paraelectric' definition (Müller & Burkard, 1979). The softening of the FE modes results in a huge increase of the dielectric permittivity (still consistent with a Curie-Weiss behaviour) on cooling. But while a divergence and, consequently, a FE phase transition would be expected at T=37 K, the dielectric permittivity stabilizes and remains constant down to the lowest accessible temperatures (Müller et al., 1991). This critical point (T_q=37 K) represents an anomaly in the continuous soft-mode behaviour, as first revealed by Müller et al. (1968) by EPR measurements and by Riste et al. (1971) by inelastic neutron scattering. The 'anomalous' regime below T_q is characterized by perturbations of the atomic positions called quantum fluctuations, which are of the same order of magnitude as the potential FE displacements. This practically suppresses the FE transition by preventing the weak Γ phonon from condensing (Müller & Burkard, 1979; Courtens et al., 1993). Residual ferroelectricity, however, was reported by many authors to show up as electric field-dependent response (Hegenbarth, 1964; Grupp & Goldman, 1999), nano-sized FE clusters (Hemberger et al., 1996; Blinc et al., 2005), and order-disorder component of the AFD phase transition (Bruce et al., 1979; Zalar et al., 2005; Bussmann-Holder et al., 2007).

latter was represented by octahedral tilting about the *c*-axis (tilt system $a^0a^0c^-$) and by different types of lattice strain; the FE mode considered was an (a,0,0) displacement of any atom. For small octahedral rotations ($0°<\phi<5°$), they confirmed that AFD and FE modes are competitive; namely, that the small energy gain (-0.5 meV) due to Ti displacement at $\phi=0°$ decreases linearly with tilt angle, as the charge transfer from anti-bonding Ti-O orbitals opposes Ti off-centering. After a threshold tilt angle ($\phi<5.7°$), however, this trend is reversed: the energy change on displacing Ti off-centre becomes negative again and the two instability now cooperate. Interestingly, in their calculations a large octahedral tilt optimizes the coordination of both A and B cations, as Sr displacement changes sign in the cooperative regime. In addition, the cooperative model only works in the presence of a considerable strain that increases the tetragonality of the cell (increasing *c*/*a* ratio).

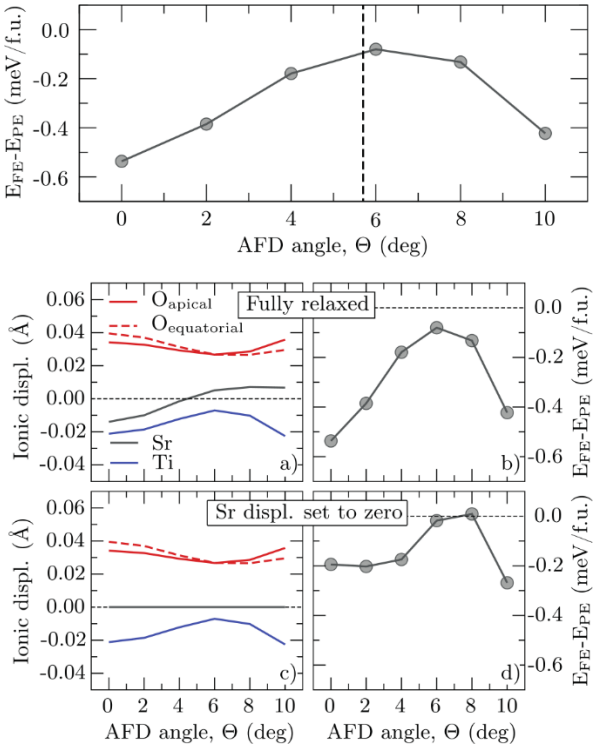

Figure 1.9: Figure from Aschauer and Spaldin (2014). The top panel shows the difference between the computed energy of a fully relaxed FE state (i.e. octahedral tilt and all displacements allowed) and that of a paraelectric state (octahedral tilt only). The bottom group of panels shows the FE atomic displacements associated to the same energy gain (A and B) and the analogous plots for a phase with fixed Sr atoms.

A different picture emerged from the work by Benedek and Fennie (2013), who analysed by DFT the case of the lower-symmetry *Pnma* perovskites. This structure befits particularly the study of the AFD/FE interplay, since it results from the superposition of two tilt modes (transforming like the irreps M3+ and R4+) while the zone-centre instability (seen for cubic

perovskites) is absent. This is shown in their survey of perovskites with *Pnma* and *Pm*-3*m* ground states (Figure 3 in their paper), which shows that only in the latter a decrease of the tolerance factor enhances the FE instability; in *Pnma*, conversely, the frequency of the FE mode is always positive, even in the case of severely underbonded A cations. It was demonstrated that in none of the *Pnma* perovskites simulated the combined tilts ($a^0a^0c^+$, $a^-a^-c^0$) are responsible for suppressing the FE mode. Instead, antiferroelectric displacements of the A cations (the X5+ mode in Figure 1.8), allowed by the *Pnma* symmetry, always contribute to optimize the A-O coordination, making the FE displacement of A cations redundant and unfavourable; hence, the positive frequency of the FE mode.

1.4 Lattice instabilities in doped strontium titanate

1.4.1 Overview of A-site dopants

These few examples already showed how the coexistence of FE and AFD instabilities can have very different outcomes depending on subtle properties of the space group symmetry. Having shown that the ground state of cubic $SrTiO_3$ is relatively close to a ferroelectric state, it is interesting to review a few examples in which chemical doping was used to alter the AFD state, and, in some cases, achieve ferroelectricity. Since the main part of this work concerns the substitution of Sr with Pr at the A-site, this paragraph outlines the properties of a few solid solutions with formula $Sr_{1-x}A_xTiO_3$.

A = Ba

Ba can replaces Sr at any concentration ($0<x<1$) and, since Ba^{2+} has a larger ionic radius than Sr^{2+} (1.61 Å vs 1.44 Å), the tolerance factor of Ba-doped $SrTiO_3$ is always slightly above 1.0. Expectedly, the long-range structure exhibits successive pseudo first-order phase transitions driven by the Γ4- instability, in analogy with pure $BaTiO_3$, and no sign of tilting instability for any Ba concentration larger than x=0.200. Dielectric permittivity spectra also show increasingly sharp peaks as Ba concentration increases, albeit smeared by the mixed character of the phase transition (Lemanov et al., 1996). The structure on the other side of the phase diagram (x<0.200) is described by the *I*4/*mcm* space group up to x=0.094 (Menoret et al., 2002), with octahedral tilt angles around ϕ=2.0° (at T=2 K) and a critical temperature (T_C~100 K) very close to those in $SrTiO_3$; coherently, dielectric permittivity peaks first become very broad (down to x=0.040) and then switch to a sloping Curie-Weiss behaviour similar to that of $SrTiO_3$ (Lemanov et al., 1996). Spontaneous polarization, setting in at x=0.094 and increasing linearly for higher Ba concentrations, is largest in the <111> direction (Menoret et al., 2002); this

matches the rhombohedral-like distribution of off-centre Ti displacements observed in the local structure by Levin et al. (2014) in samples with 20% and 50% Ba at the A-site.

A = Sn

Tin induces a FE state close to that of $PbTiO_3$. Contrary to Ba^{2+}, the Sn^{2+} ion is smaller than its cuboctahedral hole and does not favour an off-centering of the B cation. But the stereochemically-active pair of 5*s* electrons makes Sn-doped $SrTiO_3$ polarizable due to A-site off-centering. In fact, it shows a maximum of dielectric permittivity for concentrations as low as x=0.020 (Suzuki et al., 2012). The temperature of the dielectric peak varies with the frequency of the applied electric field, but only for x smaller than 0.050; any further Sn concentration induces proper ferroelectricity in $SrTiO_3$. In this regime, a FE phase transition is observed on cooling, from *Pm*-3*m* to *P*4*mm* (T_C~200 K for x=0.100, Suzuki et al., 2012). Scanning-transmission electron microscopy and pair-distribution function (PDF) analysis from neutron diffraction agree on the off-centering of the Sn^{2+} cation at the A-site (Laurita et al., 2015). While substitution of Sn at the B-site does, in fact, happen (Wang et al., 2016), only the A-site off-centering contributes to local and long-range dipolar interactions. More important, local dipolar interactions are active even in the cubic long-range phase. In particular, Laurita et al. (2015) proposed that Sn is displaced along the <110> pseudo-cubic direction (consistent with an *Amm*2 phase) at temperatures as high as 400 K. Approaching the FE phase transition, the short-range interatomic distances become consistent with the long-range *P*4*mm* symmetry.

A = Ca

Doping $SrTiO_3$ by Ca^{2+} stabilizes FE modes already in modest amounts (x=0.002): sharp dielectric permittivity peaks are observed around x=0.016, whereby the system is a 'quantum ferroelectric' (Bednorz & Müller, 1984), then broader features appear in the dielectric spectra at higher Ca concentrations ($0.016 \leqslant x \leqslant 0.120$). It is interesting to note that the low-temperature structure - the same AFD *I*4/*mcm* phase of undoped $SrTiO_3$ - persists down to the lowest accessible temperature; the small polar displacements of Ca^{2+} along <001>, despite not inducing a FE transition, are believed to form short-range ordered polar clusters (Geneste et al., 2008) responsible for the dielectric pemitivity response. Finally, ferroelectricity is suppressed for x>0.12, where successive transitions from cubic *Pm*-3*m* to AFD *I*4/*mcm* and to the *Pbnm* denote an antiferroelectric state governed by the superposition of R4+ and M3+ modes coupled with antiphase A-site displacements (Ranjan et al., 2000), close to the model proposed by Benedek and Fennie (2013) for orthorhombic non-FE perovskites.

1.4.2 Pr-doped $SrTiO_3$

Doping $SrTiO_3$ with praseodymium invokes none of the conditions leading to ferroelectricity in the previous examples: Pr^{3+} possesses no stereochemically active lone electron pair and, contrary to Ba^{2+}, its small ionic radius (1.18 Å, from Shannon, 1976) shifts the tolerance factor to well below 1. In addition, none of the other zone-boundary modes active in Ca-doped $SrTiO_3$ appears to play an important role in Pr-doped $SrTiO_3$ (Ranjan et al., 2008; Garg et al., 2009). Nonetheless, Pr-doped $SrTiO_3$ (SPTO) shows remarkable dielectric permittivity peaks at T~500 K as well as dielectric polarization loops (Duran 2005, 2008) (panel A in Figure 1.10). Early works on SPTO (x=0.050) by Duran et al. (2005, 2008) claimed that the sharp dielectric permittivity peaks and the specific heat anomalies they detected in a narrow range of temperatures could be indicative of a FE phase transition. They also found X-ray powder diffraction (XRPD) patterns compatible with the polar tetragonal *P4mm* space group, in analogy with the FE $BaTiO_3$. Shortly afterwards, another group proposed the centrosymmetric AFD structure (space group *I*4/*mcm*) as the low-temperature structure of SPTO, based on high-quality XRPD and neutron powder diffraction (NPD) data (Ranjan et al., 2008; Garg et al., 2009). Besides ruling out a normal paraelectric-ferroelectric transition on cooling, these authors pointed out that the dependence of the dielectric peaks on the frequency of the applied electric field demonstrated the diffuse character of the FE phenomena (panel B in Figure 1.10). In addition, the observation of electrostrictive strain in a lightly-doped sample (x=0.050) prompted them to describe the dielectric phenomena in terms of dielectric relaxations.

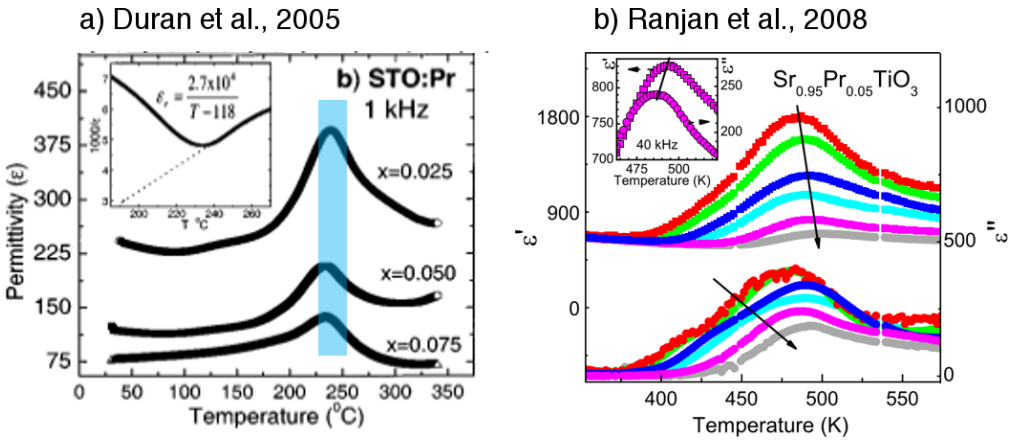

Figure 1.10: The dielectric spectra of SPTO reported in the articles referenced.

But the decrease in tolerance factor is not the only player. Pr enters the SPTO solid solution mainly as the trivalent Pr^{3+} and exclusively replaces Sr^{2+} at the A site (Sluchinskaya et al, 2012a, 2012b) and, therefore, questions arise as to the mechanism of charge compensation. Since perovskites tend not to accommodate interstitial oxygen atoms, possible pathways include charge transfer to the B site (i.e. Ti^{4+}/Ti^{3+} mixed valency), as in self-compensating La-

doped $SrTiO_3$ (Moos & Hardtl, 1997; Balachandran & Eror, 1982) or some form of vacancy formation at the A site.

References

Aschauer, U., & Spaldin, N. A. (2014). Competition and cooperation between antiferrodistortive and ferroelectric instabilities in the model perovskite $SrTiO_3$. Journal of Physics: Condensed Matter, 26(12), 122203.

Balachandran, U., & Eror, N. G. (1982). Electrical conductivity in lanthanum - doped strontium titanate. Journal of The Electrochemical Society, 129(5), 1021-1026.

Barnes, P. W., Lufaso, M. W., & Woodward, P. M. (2006). Structure determination of $A_2M_3+TaO_6$ and $A_2M_3+NbO_6$ ordered perovskites: octahedral tilting and pseudosymmetry. Acta Crystallographica Section B: Structural Science, 62(3), 384-396.

Bednorz, J. G., & Müller, K. A. (1984). $Sr_{1-x}Ca_xTiO_3$: An XY Quantum Ferroelectric with Transition to Randomness. Physical Review Letters, 52(25), 2289.

Benedek, N. A., & Fennie, C. J. (2013). Why are there so few perovskite ferroelectrics?. The Journal of Physical Chemistry C, 117(26), 13339-13349.

Blinc, R., Zalar, B., Laguta, V. V., & Itoh, M. (2005). Order-Disorder Component in the Phase Transition Mechanism of ^{18}O Enriched Strontium Titanate. Physical Review Letters, 94(14), 147601.

Brese, N. E., & O'Keeffe, M. (1991). Bond-valence parameters for solids. Acta Crystallographica Section B: Structural Science, 47(2), 192-197.

Brown, I. D. (1981). The bond-valence method: an empirical approach to chemical structure and bonding. Structure and bonding in crystals, 2, 1-30.

Brown, I. D. (1992). Chemical and steric constraints in inorganic solids. Acta Crystallographica Section B: Structural Science, 48(5), 553-572.

Bruce, A. D., Müller, K. A., & Berlinger, W. (1979). Order-disorder behavior at displacive structural phase transitions. Physical Review Letters, 42(3), 185.

Bussmann-Holder, A., Büttner, H., & Bishop, A. R. (2007). Polar-Soft-Mode-Driven Structural Phase Transition in $SrTiO_3$. Physical Review Letters, 99(16), 167603.

Campbell, B. J., Stokes, H. T., Tanner, D. E. and Hatch, D. M. (2006). ISODISPLACE: An Internet Tool for Exploring Structural Distortions. Journal of Applied Crystallography 39, 607-614.

Clark, S. J., Segall, M. D., Pickard, C. J., Hasnip, P. J., Probert, M. I., Refson, K., & Payne, M. C. (2005). First principles methods using CASTEP. Zeitschrift für Kristallographie-Crystalline Materials, 220(5/6), 567-570.

Clearfield, A. (1963). The synthesis and crystal structures of some alkaline earth titanium and zirconium sulfides. Acta Crystallographica, 16(2), 135-142.

Courtens, E., Coddens, G., Hennion, B., Hehlen, B., Pelous, J., & Vacher, R. (1993). Phonon anomalies in $SrTiO_3$ in the quantum paraelectric regime. Physica Scripta, 1993(T49B), 430.

Durán, A., Martínez, E., Díaz, J. A., & Siqueiros, J. M. (2005). Ferroelectricity at room temperature in Pr-doped $SrTiO_3$. Journal of applied physics, 97(10), 4109.

Durán, A., Morales, F., Fuentes, L., & Siqueiros, J. M. (2008). Specific heat anomalies at 37, 105 and 455 K in $SrTiO_3$: Pr. Journal of Physics: Condensed Matter, 20(8), 085219.

de Jongh, L. J., & Miedema, A. R. (1974). Experiments on simple magnetic model systems. Advances in Physics, 23(1), 1-260.

Fleury, P. A. (1976). The effects of soft modes on the structure and properties of materials. Annual Review of Materials Science, 6(1), 157-180.

Garg, R., Senyshyn, A., Boysen, H., & Ranjan, R. (2009). Structure of the noncubic phase in the ferroelectric state of Pr-substituted $SrTiO_3$. Physical Review B, 79(14), 144122.

Geneste, G., & Kiat, J. M. (2008). Ground state of Ca-doped strontium titanate: Ferroelectricity versus polar nanoregions. Physical Review B, 77(17), 174101.

Glazer, A. M. (1972). The classification of tilted octahedra in perovskites. Acta Crystallographica Section B: Structural Crystallography and Crystal Chemistry, 28(11), 3384-3392.

Glazer, A. M. (1975). Simple ways of determining perovskite structures. Acta Crystallographica Section A: Crystal Physics, Diffraction, Theoretical and General Crystallography, 31(6), 756-762.

Glazer, A. M., & Megaw, H. D. (1972). The structure of sodium niobate (T2) at 600° C, and the cubic-tetragonal transition in relation to soft-phonon modes. Philosophical Magazine, 25(5), 1119-1135.

Goldschmidt, V. M. (1926). Die gesetze der krystallochemie. Naturwissenschaften, 14(21), 477-485.

Grupp, D. E., & Goldman, A. M. (1997). Indications of a T= 0 quantum phase transition in $SrTiO_3$. Physical Review Letters, 78(18), 3511.

Hegenbarth, E. (1964). Die Feldstärkeabhängigkeit der Dielektrizitätskonstanten von $SrTiO_3$ Einkristallen im Temperaturbereich von 15 bis 80 K. Physica Status solidi (b), 6(2), 333-337.

Hemberger, J., Nicklas, M., Viana, R., Lunkenheimer, P., Loidl, A., & Böhmer, R. (1996). Quantum paraelectric and induced ferroelectric states in $SrTiO_3$. Journal of Physics: Condensed Matter, 8(25), 4673.

Hönle, W., Miller, G., & Simon, A. (1988). Preparation, crystal structures, and electronic properties of $LiGaCl_3$ and $LiGaI_3$. Journal of Solid State Chemistry, 75(1), 147-155.

Howard, C. J., & Stokes, H. T. (1998). Group-theoretical analysis of octahedral tilting in perovskites. Acta Crystallographica Section B: Structural Science, 54(6), 782-789.

Laurita, G., Page, K., Suzuki, S., & Seshadri, R. (2015). Average and local structure of the Pb-free ferroelectric perovskites (Sr, Sn)TiO_3 and (Ba, Ca, Sn) TiO_3. Physical Review B, 92(21), 214109.

Lemanov, V. V., Smirnova, E. P., Syrnikov, P. P., & Tarakanov, E. A. (1996). Phase transitions and glasslike behavior in $Sr_{1-x}Ba_xTiO_3$. Physical Review B, 54(5), 3151.

Levin, I., Krayzman, V., & Woicik, J. C. (2014). Local structure in perovskite (Ba, Sr)TiO_3: Reverse Monte Carlo refinements from multiple measurement techniques. Physical Review B, 89(2), 024106.

Lufaso, M. W., & Woodward, P. M. (2001). Prediction of the crystal structures of perovskites using the software program SPuDS. Acta Crystallographica Section B: Structural Science, 57(6), 725-738.

Megaw, H. D. (1968). A simple theory of the off-centre displacement of cations in octahedral environments. Acta Crystallographica Section B: Structural Crystallography and Crystal Chemistry, 24(1), 149-153.

Megaw, H. D. (1973). Crystal structures: a working approach (No. 10). Saunders Limited.

Menoret, C., Kiat, J. M., Dkhil, B., Dunlop, M., Dammak, H., & Hernandez, O. (2002). Structural evolution and polar order in $Sr_{1-x}Ba_xTiO_3$. Physical Review B, 65(22), 224104.

Meyer, G. M., Nelmes, R. J., & Hutton, J. (1978). High-resolution (direct space) studies of anharmonic motion associated with the structural phase transition in $SrTiO_3$. Ferroelectrics, 21, 461-462.

Mitchell, R. H., Chakhmouradian, A. R., & Woodward, P. M. (2000). Crystal chemistry of perovskite-type compounds in the tausonite-loparite series,$(Sr_{1-2x}Na_xLa_x)TiO_3$. Physics and Chemistry of Minerals, 27(8), 583-589.

Miller, S. C., & Love, W. F. (1967). Tables of irreducible representations of space groups and co-representations of magnetic space groups. Pruett Press.

Momma, K., & Izumi, F. (2011). VESTA 3 for three-dimensional visualization of crystal, volumetric and morphology data. Journal of Applied Crystallography, 44(6), 1272-1276.

Moos, R., & Hardtl, K. H. (1997). Defect Chemistry of Donor-Doped and Undoped Strontium Titanate Ceramics between 1000 and 1400 C. Journal of the American Ceramic Society, 80(10), 2549-2562.

Müller, K. A., Berlinger, W., & Waldner, F. (1968). Characteristic structural phase transition in perovskite-type compounds. Physical Review Letters, 21(12), 814.

Müller, K. A., & Burkard, H. (1979). $SrTiO_3$: An intrinsic quantum paraelectric below 4 K. Physical Review B, 19(7), 3593.

Müller, K. A., Berlinger, W., & Tosatti, E. (1991). Indication for a novel phase in the quantum paraelectric regime of $SrTiO_3$. Zeitschrift für Physik B Condensed Matter, 84(2), 277-283.

Okazaki, A., & Suemune, Y. (1961). The Crystal Structures of $KMnF_3$, $KFeF_3$, $KCoF_3$, $KNiF_3$ and $KCuF_3$ Above and Below Their Neel Temperatures. Journal of the Physical Society of Japan, 16(4), 671-675.

O'Keeffe, M. (1989). The prediction and interpretation of bond lengths in crystals. In Stereochemistry and Bonding (pp. 161-190). Springer Berlin Heidelberg.

Peschel, S., Ziegler, B., Schwarten, M., & Babel, D. (2000). Kristallstrukturbestimmungen an Cs_2NaCr (CN) 6 und weiteren Verbindungen $A_2BM(CN)_6$ (A= Rb, Cs; B= Na, K, Rb, NH_4; M= Cr, Mn, Fe, Co): Oktaederkippung und Toleranzfaktor von Cyanokryolithen. Zeitschrift für anorganische und allgemeine Chemie, 626(7), 1561-1566.

Ranjan, R., & Pandey, D. (1999). Novel structural features and phase transition behaviour of $(Sr_{1-x}Ca_x)TiO_3$: II. X-ray diffraction studies. Journal of Physics: Condensed Matter, 11(10), 2247.

Ranjan, R., Garg, R., Hackl, R., Senyshyn, A., Schmidbauer, E., Trots, D., & Boysen, H. (2008). Onset of spontaneous electrostrictive strain below 520 K in Pr-doped $SrTiO_3$. Physical Review B, 78(9), 092102.

Riste, T., Samuelsen, E. J., Otnes, K. T., & Feder, J. (1971). Critical behaviour of $SrTiO_3$ near the 105 K phase transition. Solid state communications, 9(17), 1455-1458.

Samara, G. A. (2003). The relaxational properties of compositionally disordered ABO3 perovskites. Journal of Physics: Condensed Matter, 15(9), R367.

Shannon, R. T. (1976). Revised effective ionic radii and systematic studies of interatomic distances in halides and chalcogenides. Acta Crystallographica Section A: Crystal Physics, Diffraction, Theoretical and General Crystallography, 32(5), 751-767.

Shirane, G., Danner, H., Pavlovic, A., & Pepinsky, R. (1954). Phase Transitions in Ferroelectric $KNbO_3$. Physical Review, 93(4), 672

Shirane, G., Danner, H., & Pepinsky, R. (1957). Neutron Diffraction Study of Orthorhombic $BaTiO_3$. Physical Review, 105(3), 856.

Shirane, G., & Yamada, Y. (1969). Lattice-Dynamical Study of the 110° K Phase Transition in $SrTiO_3$. Physical Review, 177(2), 858.

Sluchinskaya, I. A., Lebedev, A. I., & Erko, A. (2012). a) Crystal structure, local structure, and defect structure of Pr-doped $SrTiO_3$. Journal of Applied Physics, 112(2), 024103; b) XAFS studies of the local structure and charge state of the Pr impurity in $SrTiO_3$. Physics of the Solid State, 54(5), 975-979.

Tsuda, K., & Tanaka, M. (1995). Refinement of crystal structure parameters using convergent-beam electron diffraction: the low-temperature phase of $SrTiO_3$. Acta Crystallographica Section A: Foundations of Crystallography, 51(1), 7-19.

Vanderbilt, D., & Zhong, W. (1998). First-principles theory of structural phase transitions for perovskites: competing instabilities. Ferroelectrics, 206(1), 181-204.

Wang, T., Pitike, K. C., Yuan, Y., Nakhmanson, S. M., Gopalan, V., & Jalan, B. (2016). Chemistry, growth kinetics, and epitaxial stabilization of Sn^{2+} in Sn-doped $SrTiO_3$ using $(CH_3)_6Sn_2$ tin precursor. APL Materials, *accepted*.

Woodward, P. M. (1997). Octahedral tilting in perovskites. II. Structure stabilizing forces. Acta Crystallographica Section B: Structural Science, 53(1), 44-66.

Zalar, B., Lebar, A., Seliger, J., Blinc, R., Laguta, V. V., & Itoh, M. (2005). NMR study of disorder in $BaTiO_3$ and $SrTiO_3$. Physical Review B, 71(6), 064107.

Zhong, W., & Vanderbilt, D. (1995). Competing structural instabilities in cubic perovskites. Physical review letters, 74(13), 2587.

:Chapter 2:

Total scattering analysis of powder diffraction data

2.1 Local structure from total scattering

2.1.1 Why local structure?

Properties in materials are often the result of internal competing forces. Their mechanism usually owes to a precise arrangement of atoms not necessarily captured by the average, long-range order of the material. Examples of disorder in crystalline materials include the incomplete softening of the zone-centre mode in $SrTiO_3$ and the dipolar clusters deemed responsible for low-temperature ferroelectric states (see section 2.4). How exactly does an average model fail? Consider, for instance, a phase in which sites have fractional or mixed occupancy: these are, by definition, not described by an average model, since each individual site is either vacant or occupied - by either atom X or Y. Although in reciprocal-space analysis the mismatch may disappear into a large thermal parameter and still allow a good fit to the data, the structure description is incomplete: vacancies or either type of atom are in this model assumed to be statistically distributed, but also clustered or arranged in an orderly pattern.

Deviations from the long-range structure are the result of structural inhomogeneity on a shorter length scale. This is why the description of the average, long-range structure and that of the environment in the first few Å or nanometres around each atom are perfectly complementary approaches emphasizing different structural features. In practice, local structure can be studied in a few ways. X-ray absorption spectroscopy (XAS) is a technique extremely sensitive to the arrangement of nearest-neighbour species around a single type of atom and, as such, it contains no information on short-range order beyond the first couple of shells. Scanning-tunnelling microscopy and atomic-force microscopy yield information with sub-nanometre spatial resolution but cannot probe the bulk structure. Transmission-electron microscopy is bulk-probing, but the limited amount of matter sampled (tens of nanometres) may not be representative of the whole material. Atomic pair distribution function (PDF) analysis is a diffraction method that probes the bulk structure and give robust information, potentially, up to several tens of nanometres. In its normal implementation, the PDF is not element-sensitive, so it represents the distribution of all interatomic distances in the solid.

Atomic distribution functions are obtained through ‘total’ scattering measurements. This means recording the scattered intensity at all possible changes in energy and momentum of the incident radiation - in other words, measuring elastic and inelastic (coherent) over the widest possible range of scattering vector (Q, see Appendix to this Chapter). Of the total scattered intensity, the elastic part makes up the Bragg component, used for determining the long-range structure, e.g. by Rietveld analysis. Bragg peaks rest on a low, oscillating background that comprises diffuse scattering, both the elastic and the inelastic parts; the former contains information on the static local structure, while the latter part arises from local structural

dynamics. Total scattering is thus named after the unresolved sum of the intensities of the three contributions.

2.1.2 Basic derivation and functions

This paragraph presents the relationship between the scattered intensity measured and the atomic PDF functions defined below and used throughout this work. This simple derivation is loosely based on the equations by Hannon et al. (1990) and the thorough treatment reported in the user's guide of the Gudrun program (Soper, 2012). Excellent accounts can be also found in the books by Thorpe and Billinge (1998) and by Egami and Billinge (2003). The PDF formalisms used below are taken from the paper by Keen (2001) and referenced in the manual of the RMCProfile software (Tucker et al., 2012). The notation presented here is used consistently throughout this work and references are made where needed to the equivalent functions defined by Keen. The scattering vector $\boldsymbol{Q}$ is defined in the next section.

The radiation scattered from an ensemble of atoms situated at positions R_1, R_2, ..., R_N is given by:

$$A(\boldsymbol{Q}) = \sum_{j}^{N} b_j \exp\left(i\boldsymbol{Q} \cdot R_j\right).$$

where b_j is either a dimensionless number corresponding to either the isotope-averaged, coherent neutron scattering length or the Q-dependent X-ray atomic form factor. $A(\mathbf{Q})$ corresponds to the Fourier transform of the atomic positions and its relationship to the quantity actually measured in a scattering experiment, $I(\mathbf{Q})$, is:

$$I(\boldsymbol{Q}) = \frac{1}{N}|A(\boldsymbol{Q})|^2 =$$

$$= \frac{1}{N}\sum_{j,k} b_j\, b_k \exp\left[i\boldsymbol{Q} \cdot \left(\boldsymbol{R}_j - \boldsymbol{R}_k\right)\right].$$

The sum over all atoms can be divided into: i) a 'self' term (j=k), the correlation of every atom with itself; ii) a 'distinct' term, the correlations between distinct atoms (i.e. not necessarily different atom types). If the scattering material is composed of multiple elements (α,β), $I(\mathbf{Q})$ can be expressed in terms of partial correlation functions as:

$$I(Q) = \sum_{\alpha} c_\alpha\, b_\alpha^2 + \sum_{\alpha,\beta>\alpha} \left(2 - \delta_{\alpha\beta}\right) c_\alpha b_\alpha c_\beta b_\beta S_{\alpha\beta}(\boldsymbol{Q}),$$

where the first part contains the 'self' terms (i.e. pairs of same atom types). Each term is weighted by the respective scattering lengths and the use of the Kronecker delta only allows unique atom pairs. For N atom types in the material, there are $N(N+N)/2$ partial structure factors $S_{\alpha\beta}(\mathbf{Q})$, each defined as:

$$S_{\alpha\beta}(\boldsymbol{Q}) = \rho \int g_{\alpha\beta}(\boldsymbol{r}) \exp\left(i\boldsymbol{Q} \cdot \boldsymbol{r}_{\alpha\beta}\right) d\boldsymbol{r}.$$

with ρ the atomic number density (i.e. number of atoms per unit volume). $S_{\alpha\beta}(\mathbf{Q})$ corresponds to the Fourier transform of the partial PDF $g_{\alpha\beta}(\mathbf{r})$. For an ideal powder, i.e. one in which crystallites are oriented in any possible direction (Ω) with equal probability and are numerous enough to cover all relative orientations of $\mathbf{Q}$ and $\mathbf{r}$ (in polar coordinates, $\mathbf{Q} \cdot \mathbf{r}_{\alpha\beta} = Q \cdot r_{\alpha\beta} \cos\theta$), the orientationally averaged scattering function is obtained as:

$$\langle \exp(i\boldsymbol{Q} \cdot \boldsymbol{r}_{\alpha\beta}) \rangle_{\Omega} = \frac{1}{4\pi} \int_0^{2\pi} d\vartheta \int_0^{\pi} \sin\theta \, d\theta \exp\left(iQr_{\alpha\beta} \cos\theta\right) =$$

$$= \frac{1}{2} \int_{-1}^{+1} \exp\left(iQr_{\alpha\beta} \cos\theta\right) d\theta =$$

$$= \frac{\sin(Qr_{\alpha\beta})}{Qr_{\alpha\beta}}.$$

Notice that the orientationally averaged Q and r are now taken as the respective magnitudes. So, for an isotropic system, $I(\mathbf{Q})$ can be finally rewritten as:

$$\langle I(\boldsymbol{Q}) \rangle_{\Omega} = I(Q) =$$

$$= \sum_{\alpha} c_{\alpha} \, b_{\alpha}^2 + \sum_{\alpha,\beta>\alpha} \left(2 - \delta_{\alpha\beta}\right) c_{\alpha} b_{\alpha} c_{\beta} b_{\beta} \, \rho \left[\delta(Q) + \int_0^{\infty} 4\pi r^2 \, g_{\alpha\beta}(r) \, \frac{\sin(Qr_{\alpha\beta})}{Qr_{\alpha\beta}} \, dr \right].$$

In the second term, the delta-function in reciprocal space $\delta(Q)$ represents a constant scattering level in real space, depending only on the scattering lengths (form factors in the case of X-rays) in the sample. Fluctuations about the constant scattering level are given by the integral term, which contains all the 'distinct' interatomic correlations at a distance r.

If all atom types are considered, this quantity represents the fluctuation of the local atomic density with respect to the mean density, averaged over all the atoms in the material. After summation over all the atom types, the integral in the second term is equivalent to $F(Q)$[1].

$$F(Q) = \int_0^\infty 4\pi\rho r^2\, g(r)\, \frac{\sin(Qr_{\alpha\beta})}{Qr_{\alpha\beta}}\, dr$$

Coherently, the sum of all the $g_{\alpha\beta}(r)$ in the previous equation corresponds to the $g(r)$ PDF[2]:

$$g(r) = \sum_{i,j} c_\alpha b_\alpha c_\beta b_\beta (g_{\alpha\beta}(r) - 1),$$

where the partial $g_{\alpha\beta}(r)$, which oscillates between 0 and 1, is subtracted by 1 to yield the limiting values:

$$g(r \to 0) = -\left(\sum_i c_i b_i\right)^2 ;\ g(r \to \infty) = 0$$

This is the function used in the Reverse Monte Carlo refinements presented in the second part of Chapter 4. It is related to the experimental intensity, $I(Q)$, by the Fourier transform of the $F(Q)$ term defined above:

$$g(r) = \frac{1}{(2\pi)^3\rho} \int_0^\infty 4\pi Q^2\, F(Q)\, \frac{\sin(Qr)}{Qr}\, dQ$$

The alternative function $G(r)$ changes from $g(r)$ in that it is scaled by r and, whenever used in this work, it is called $G(r)$[3]. It is the PDF function used as standard by the programs PDFFit (Proffen and Billinge, 1999) and PDFGui (Farrow et al., 2007). Its relationship to $g(r)$ is given by:

$$G(r) = g(r)\frac{4\pi\rho\, r}{(\sum_i c_i b_i)^2}$$

It will be apparent that the limiting values of $G(r)$ are:

$$G(r \to 0) = -4\pi\rho r;\ G(r \to \infty) = 0,$$

giving $G(r)$ its characteristic slope at low-r, whose agreement with the expected slope is usually a loose indication that data were normalised properly. Similarly, the first, flat segment of the

[1] This is the same function referenced as $F(Q)$ in Keen's paper.
[2] This is the function called $G(r)$ in Equations 10 and 15 in Keen's paper.
[3] This is the function called $G^{PDF}(r)$ in Equations 43 and 44 in Keen's paper. It is equivalent to the $D(r)$ defined *ibid*. divided by the squared sum of the molar fraction-weighted scattering lengths, $(\sum_i c_i b_i)^2$. Thus, using $D(r)$ in PDFGUI is perfectly acceptable, but expect an overall scale factor approximately $(\sum_i c_i b_i)^2$.

$g(r)$ should be level with its low-r limit. Finally, Figure 2.1 shows the functions $F(Q)$, $G(r)$, and $g(r)$ obtained from neutron total scattering of $SrTiO_3$.

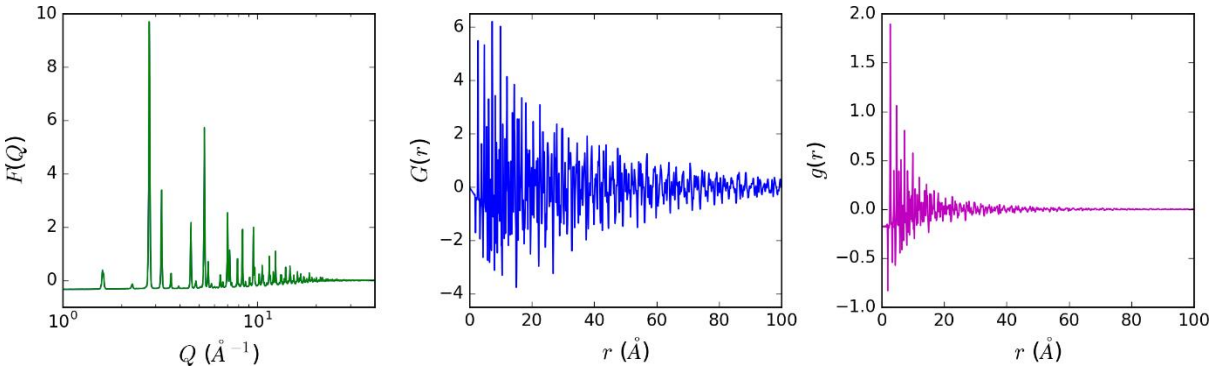

Figure 2.1: F(Q) (left panel), G(r) (middle panel), and g(r) (right panel) obtained from neutron total scattering data of $SrTiO_3$ at 90 K temperature.

2.2 Total scattering experiments

2.2.1 Effect of Q_{max}, instrument resolution, counting statistics, normalisation

Assuming that the reader is familiar with the basics of crystallography (Warren, 1969; Stout & Jensen, 1989; Giacovazzo, 2002), only the concepts specific to total scattering experiments are recalled in this section.

Typical measurement geometry is transmission. An incident beam of photons (neutrons) of wavelength λ and wavevector **k** ($|\mathbf{k}| = k = 2\pi/\lambda$) is scattered by a powder sample at an angle 2θ. The wavevector of the scattered photons (neutrons) is **k'** which, in the case of elastic scattering, has the same magnitude k as the incident wave. The scattering vector is given by $\mathbf{Q} = \boldsymbol{k} - \boldsymbol{k}'$ and its modulus, following from Bragg's law, is given by $|\mathbf{Q}| = Q = 2k\sin\theta = 4\pi\sin\theta/\lambda$. Since the scattering from a powder is isotropic - ideally - we are only concerned with its magnitude Q.

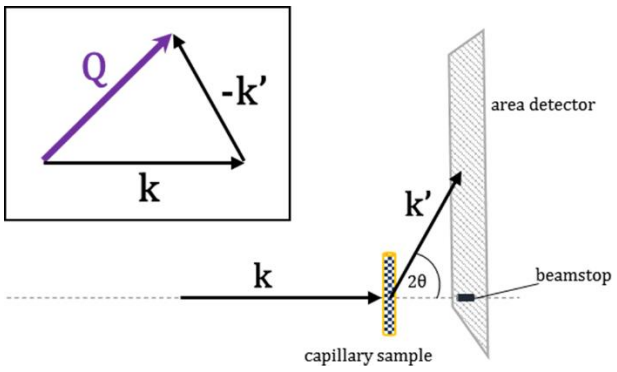

Figure 2.2: Basic scattering geometry and definition of the scattering vector, Q.

The definition of $g(r)$ given in paragraph 2.1.2 assumes that $F(Q)$ is integrated over an infinite range of Q. The largest value of Q accessible in a diffraction experiment, $Q_{max}=4\pi\sin\theta/\lambda$, is limited by the X-ray or neutron wavelength λ and by the maximum 2θ angle attainable. The termination error of the Fourier transform - the Gibbs phenomenon - results in oscillations of definite wavelength throughout the $g(r)$ that can be seen most clearly in the inter-peak regions at low-r. As demonstrated by Toby and Egami (1992), integrating over a finite range of Q is also equivalent to multiplying the integrand, $F(Q)$, by a step function [$Z(Q)=1$ for $Q\leq Q_{max}$; $Z(Q)=0$ for $Q>Q_{max}$]. After taking the Fourier-transform, this product translates into the convolution of $g(r)$ with a broadening function with the form $\sin(Q_{max}\,\Delta r)/\Delta r$. This broadening adds to that caused by thermal motion, but it can be reduced to a negligible fraction of thermal broadening using a large enough value of Q_{max}. The threshold value, demonstrated Toby and Egami (1992) for a handful of reference materials, can be found when Q_{max} is larger than the average Debye-Waller factor by the ratio shown in panel A of Figure 2.2.

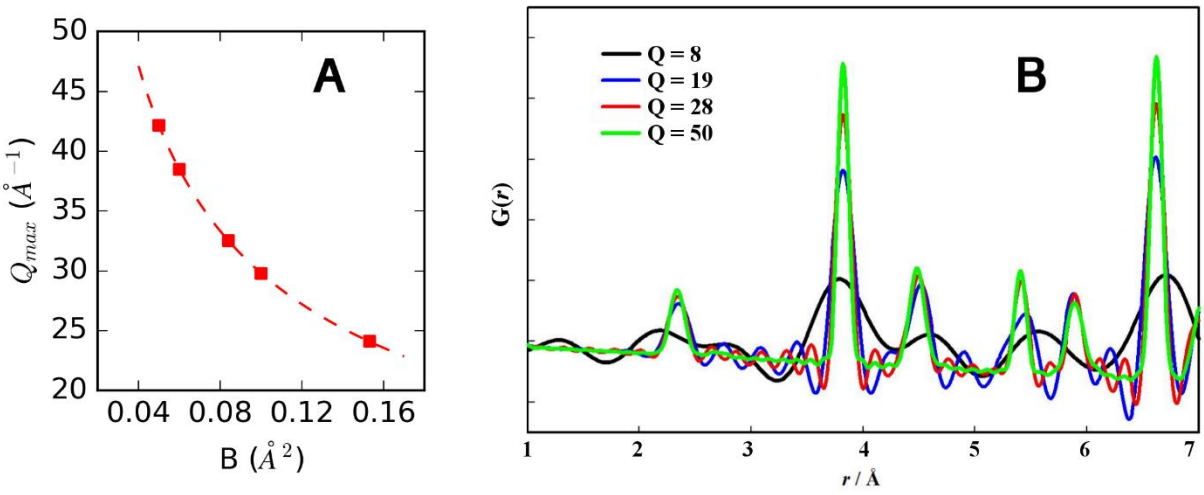

Figure 2.3: Panel A: values of Q_{max} minimizing termination error for different Debye-Waller factors. Squares represent the lowest Q_{max} value at which thermal broadening outsizes termination broadening in the data from Toby and Egami (1992). The dashed line merely gives a cue for the trend. Panel B: from Coduri (2012), G(r) of CeO_2 calculated at varying values of Q_{max}.

Another way to think of the effect of Q_{max} on $g(r)$ broadening is through the spatial resolution $\Delta r/r \approx 2\pi/Q_{max}$. It becomes apparent why a Cu-Kα X-ray wavelength or cold neutrons are not suited to measure data for PDF analysis and why this usually requires high-energy radiation like that available at synchrotron and neutron sources. This is further evidenced by panel B of Figure 2.3 (picture from Coduri, 2012). The black curve is the X-ray $G(r)$ of a CeO_2 reference calculated using $Q_{max}=8$ Å^{-1}, the value one can obtain with a Cu-anode lab diffractometer; also shown are the $G(r)$ curves attainable with a Mo or Ag anode (19 Å^{-1}), with a typical synchrotron measurement (28 Å^{-1}), and a very high Q_{max} as a reference (50 Å^{-1}).

In the light of broadening and termination error, one might decide to use the highest Q_{max} available. However, the choice of Q_{max} must also consider the decreasing signal-over-noise ratio as the 2θ range is extended. Especially in the case of X-rays, because of the decay of the coherent intensity with 2θ, including high-Q data introduces noise in the experimental functions. The Q value at which Bragg peaks are no longer visible may be a loose indication of the ideal Q_{max} for a given material: truncating too early complicates data normalisation as the true scattering level is hidden under overlapping peaks; going too far introduces a large incoherent contribution to the high-Q data. Assuming a sensible choice of Q_{max} is made, another way to rid the data of noise is to increase counting statistics. The weight of random uncertainties of data points - their estimated standard deviation - is reduced by $\sqrt{N}$ times by taking N independent observations. This is shown in practice in Figure 2.4. Each row represents the scattering functions and $G(r)$ calculated on X-ray data obtained after half the counting time of the row above. Contrary to the low-Q region of $F(Q)$, where signal-to-noise ratio is higher, the high-Q region is dramatically affected by reducing counting statistics. The $G(r)$ curves shown in the right column demonstrate that noise at high-Q has the largest influence on spurious oscillation at low-r in real space.

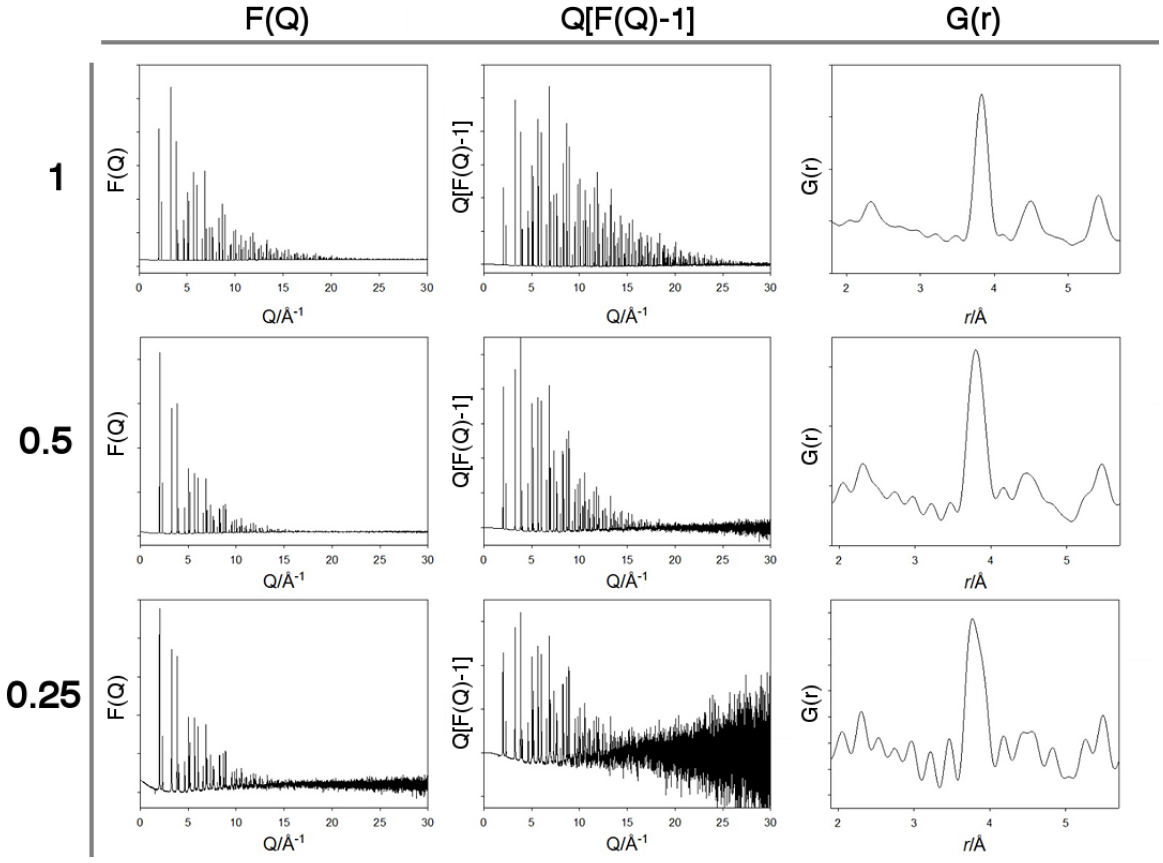

Figure 2.4: Scattering functions F(Q) and Q[F(Q)-1] and the Fourier-transform of the latter, G(r) of a reference CeO_2 sample calculated from data at different counting times. Rows represent the relative counting times (1, 0.5, and 0.25) in descending order.

The last effect presented in this paragraph is the damping of PDF peak intensities. This has different meanings for $g(r)$ and $G(r)$. Since $g(r)$ tends to the average scattering level of the material at high-r, the amplitude of its oscillations falls off like $1/r$; the amplitude of oscillations is constant, instead, in $G(r)$, which therefore represents directly the structural coherence of a sample. The effect of a higher coherence length appears evident, for instance, by comparing the X-ray $G(r)$ of crystalline CeO_2 (panel A in Figure 2.4) to those of nanoparticle samples shown in panel D of Figure 2.5. While CeO_2 has relatively intense peaks at 600-1000 Å, the $G(r)$ curves of iron nanoparticles (Orlando et al., 2015) become featureless at a characteristic coherence length despite the positive effect, as it will be now explained, of a high Q-resolution.

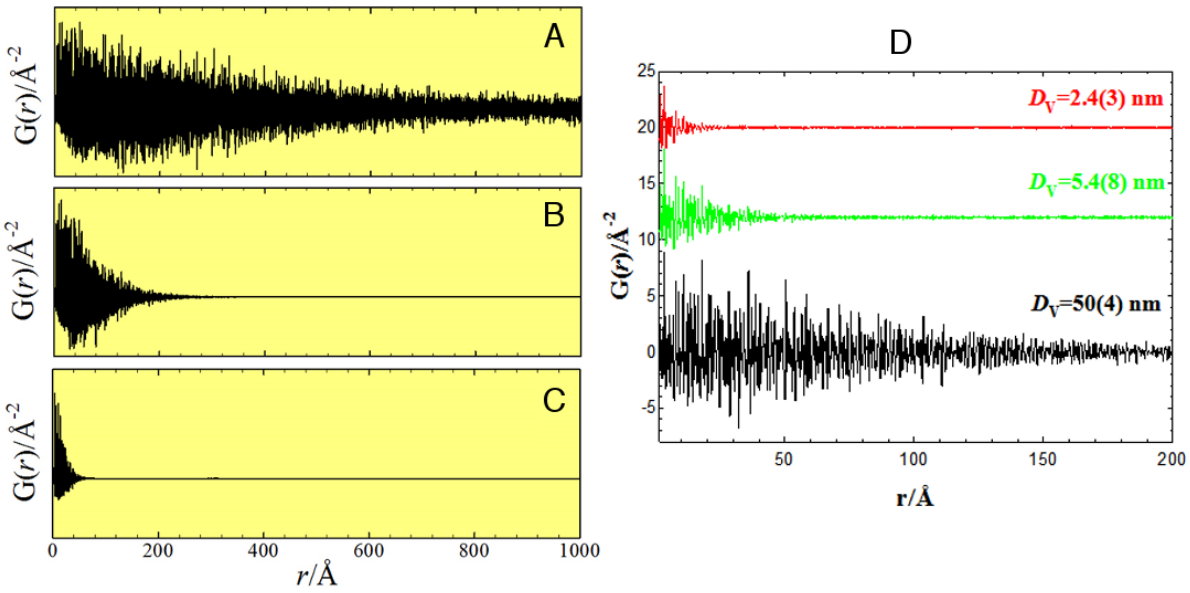

Figure 2.5: Panel A: G(r) curve of crystalline CeO_2 obtained at high Q-resolution ($\Delta Q/Q=10^{-4}$) at the ID22 beamline of ESRF. Panels B and C: G(r) curves of the same sample obtained in a standard measurement using the area detector at ID22 (between 10^1-10^2 times less resolved) and using the FReLoN camera at ID11 of ESRF (between 10^2-10^3 times less resolved). Panel D: intensity falloff of the G(r) of iron nanoparticles of varying coherence lengths, collected using the same high-resolution setup as in panel A.

There is another important contribution to intensity falloff not related to the sample. The limited Q-resolution of the measurement, which depends largely on the sample-detector distance and the type of detector used, results in greatly different intensity damping. Figure 2.4, for instance, shows (panels A-C) the $G(r)$ of crystalline CeO_2 measured with a high-resolution setup (A); an intermediate resolution setup, with an area detector positioned at a large distance from the sample (B); a low-resolution, high-throughput setup, with an area detector positioned close to the sample (C). While the intensity falloff can be reproduced quite easily in the case of constant $\Delta Q/Q$ (Egami and Billinge, 2003), the same correction is trickier for multiple detector banks as in the case of time-of-flight instruments (Tucker et al., 2001).

Finally, an outline of the corrections needed to obtain a reliable $I(Q)$ for the calculation of the PDF from the raw intensity. A successful correction should put the measured intensity on an absolute scale (barns or electrons per atom per unit of solid angle): not only this helps relating measurements from different sources, but correct coordination numbers can be calculated from PDF peak areas, too. Measured intensity is divided by the incident flux (measured by a beam monitor) and by the solid angle covered by the detector. In the case of neutron scattering, measuring a rod of vanadium, a purely incoherent scatterer, yields the accurate spectrum of the neutron source. The sample is normally contained in some vessel: for X-rays this is often a capillary made of polyimide, borosilicate glass, or fused silica (quartz glass); for neutrons, this usually means a cylindrical vanadium can. In more complicated cases, there might be a device for heating/cooling, a pressure cell, a cell for electric or magnetic fields, etc. The contribution of anything but the sample should be measured and subtracted from the total measured intensity. This can also involve the background from the empty instrument (more often with neutrons), whose signal should contribute equally to the intensity of the sample and of the empty container.

Correction for absorption is usually painless for both X-ray and neutron scattering. It is calculated from the geometry of the specimen and the absorption coefficients of the atoms involved (plus the possible contribution of any object intercepting the beam). However, artefacts can be introduced in the case of fluorescence emission by atoms close to their X-ray absorption edge or when nuclear resonance causes very high neutron capture at a certain wavelength. Besides minimising the absorption coefficient, the choice of wavelength (or of wavelength range, in the case of TOF) must account for all these effects. Multiple scattering is related to absorption, since it contributes to total attenuation of the scattered beam (Soper, 2012). Multiple scattering occurs when the beam is scattered twice or more before it leaves the sample. Double scattering is, however, the most intense component and is usually what corrections cater for. For X-rays a correction was proposed by Dwiggins and Park (1971); for neutrons by Soper and Egelstaff (1980).

The effect of inelastic, incoherent (Compton) scattering from recoiling electrons can be large when using high energy X-rays, particularly at high-Q, where its cross-section increases over the vanishing coherent cross-section. Correction for Compton scattering can be avoided using analyser crystals between sample and detector, excluding the wavelengths of inelastically scattered photons. In the case of neutrons, the effect of inelasticity does not affect the ‘distinct’ part of $I(Q)$ [i.e. the part containing $F(Q)$ and, thus, the Fourier transform of the PDF] so much as it affects self-scattering (Soper, 2009). The correction used today borrows much from the treatment by Placzek (1952).

2.2.2 Synchrotron X-ray experiment

Total scattering experiments have become common relatively recently thanks to the higher availability of high-energy, high-flux radiation at large facilities. As evidenced in paragraph 2.2.1, total scattering measurements need to maximise both counting statistics and 2θ range compared with a conventional scattering experiment. For X-rays, synchrotrons meet these demands brilliantly. Diffraction beamlines situated on undulators provide a high-flux, collimated beam of highly monochromatic, coherent photons of any arbitrary energy[4] in the range 10-100 keV. Thus, PDF-quality data [i.e. a pattern with $Q_{max}(=4\pi\sin\theta/\lambda)$ more than 30 $Å^{-1}$ and high signal-over-noise ratio] of a crystalline powder can be collected in just few minutes.

The experimental setup needed for total scattering measurement is better illustrated referring to a well-endowed beamline such as ID22 at ESRF (Fitch, 2004). Though not primarily a PDF beamline, its high-resolution setup makes it possible to extend PDF analysis to the nanometre range (1-50 nm), as demonstrated in Chapter 6. White X-ray beam from the undulators is initially collimated by a curved mirror, which reduces its vertical divergence. The collimated white beam is monochromated by a silicon double-crystal, cooled to liquid-nitrogen temperature to withstand the intense photon flux; thus, selecting a wavelength means collecting the beam scattered at a certain angle to the 111 Bragg reflection of Si. Beam size is then adjusted between 0.5×0.1 and 1.5×1.5 mm^2 using water-cooled slits. The beam is scattered from the sample, generally a spinning capillary, towards nine scintillator detectors mounted offset on the 2θ circle of the diffractometer and each preceded by a Ge-111 analyser crystal. The use of analyser crystals (combined with high vertical collimation) results in high reproducibility of peak positions and an extremely narrow instrumental resolution function, whose effect on the intensity of PDF peaks is explained in paragraph 2.2.1. Finally, total scattering data can be collected in a wide range of temperature as the capillary can be heated/cooled from room temperature using a cryostat (5 K≤T≤290 K), a cold nitrogen stream (80 K≤T≤370 K), a hot air blower (300 K ≤T≤1100 K), or a mirror furnace (T ≤1700 K).

2.2.3 Time of flight neutron experiment

Unlike constant-wavelength X-ray and neutron diffraction, the time-of-flight (TOF) technique uses a white beam of neutrons impinging on the sample at a fixed angle. The TOF technique is used at spallation neutron sources to maximise counting statistics, since the time-averaged flux is lower than that of a reactor source (10^{13} neutrons cm^{-2} s^{-1} compared with 10^{15} neutrons cm^{-2}

[4] In practice there are preferred energy points corresponding to maxima of undulator emission. Excellent accounts of synchrotron physics can be found in the books by Baruchel (1993) and by Als-Nielsen & McMorrow (2011)

s^{-1}). On the other hand, spallation neutrons are emitted in very intense pulses (~10^{19} neutrons cm^{-2} s^{-1}), so high counting statistics is recovered by collecting the polychromatic beam for many of such high-flux pulses (Kisi & Howard, 2012).

Spallation neutrons are produced by bombarding a tungsten or uranium target with high-energy (GeV) protons. Every collision liberates ~30 high-energy neutrons, which need to be slowed down by a moderator medium, usually hydrogen, water or methane so as to exploit the large incoherent, inelastic scattering cross-section of hydrogen. Neutrons leave the moderator with energies peaking at the temperature of the moderator ($E=T\times k_1$, with k_1=0.0861734 eV/K) while their energy spectrum consists of a Maxwellian thermal distribution and a continuous tail of energies corresponding to undermoderated[5], hot (epithermal) neutrons. This tail comprises short wavelengths (down to 0.05 Å), allowing measurements in Q-ranges considerably wider (up to 100 $Å^{-1}$) than attainable with a constant-wavelength diffractometer. Every wavelength in the spectrum is identified by the time taken by the neutron to travel from source to detector. This happens because high-energy, short-wavelength neutrons move faster than longer-wavelength neutrons, resulting in a time spread of the neutron bunch. It becomes apparent that wavelengths can be better resolved by making the flight path longer.

Scattered neutrons are detected by arrays of scintillator detectors covering all possible 2θ and arranged in banks to cover the largest possible solid angle. At the GEM diffractometer at the ISIS spallation source (Hannon, 2005), for instance, detectors are positioned in the range $1.2°\leq 2\theta \leq 171.4°$ and cover an area in excess of 7 m^2, considerably larger than the area of a conventional 2-D X-ray detector. Since the wavelength and, thus, the scattering vector (Q) of every neutron detected is known from the scattering angle of the detector and the time of arrival, the whole range of Q is measured by multiple detectors. Detectors situated at different 2θ have different count rates as a function of Q depending on the portion of solid angle they cover, so they contribute differently to the crucial high-Q part of the data. Finally, an implicit advantage of having detectors in a wide 2θ range is a high tolerance to complex sample environments. This allows using a wide array of cooling and heating devices, pressure cells or gas-flow systems.

[5] Undermoderation, i.e. release of neutrons that have not reached thermal equilibrium with the moderator, is deliberate and is the method used to avoid overlap of pulses, which would reduce peak flux and destroy the time-resolution of TOF acquisition.

2.3 Data analysis

2.3.1 Fitting a structural model to the PDF

Extracting structural information from PDF data can follow a method analogous to Rietveld analysis. This is the approach implemented in the programs PDFFit and PDFGui (Proffen & Billinge, 1999; Farrow et al., 2007). A calculated PDF is computed from a structural model and compared to the experimental PDF. The refinable parameters of the structural model are varied to optimize the agreement between the calculated and experimental functions by means of a least-squares minimization. In general, this method assesses the validity of the model proposed by the user. This is estimated by the profile fit residual

$$R_p = \left[\frac{\sum w_i(G_i^{exp} - G_i^{calc})^2}{\sum w_i(G_i^{exp})^2}\right]^{\frac{1}{2}}$$

where G_i^{exp} and G_i^{calc} are the i-th point of the experimental $G(r)$ and of the calculated $G(r)$, respectively, and w_i is the weight of each point G_i^{exp} (normally the uncertainty on its value). The routine for calculating PDF from a structural model is described in detail by Egami and Billinge (2003). Suffice to say here that, for a model with N atoms, interatomic distances are calculated recursively between each of the N atom and all the neighbours within a cutoff distance of choice; intensity builds up by adding a count for every neighbour; the final function must then be normalized by the scattering lengths of the atom types involved and by the total number of atoms. This can be written as:

$$R(r) = \frac{1}{N}\sum_{\alpha\beta}\frac{b_\alpha b_\beta}{\langle b\rangle^2}\delta\left(r - \left(r_\alpha - r_\beta\right)\right).$$

The core step of this method is choosing a model with sensible parameters to be refined. In the simplest case, this can be a single phase with refinable lattice parameters and few atomic positions; in some cases, such as short-range order, a multiphase model with refinable phase fraction (see Chapter 6) or a supercell of the crystallographic unit cell. For crystalline solids, a more systematic approach can be refining directly soft-mode amplitudes as obtained from a symmetry decomposition of the parent structure of the compound studied. The latter approach is presented in Chapter 5.

The agreement between experimental and calculated PDF is aided by parametrisation of the instrumental effects influencing as-collected data (thus, in reciprocal space). The programs mentioned use explicit corrections for Q_{max} and for Q-resolution (Qiu et al., 2004). In practice, these are catered for by a dampening function applied to the $G(r)$ and by an r-dependent broadening of the $G(r)$. Instrumental parameters are not usually refined together with the free parameters of the structural model; instead, they should be refined prior to the analysis using a

reference compound, so that sample-related broadenings are absent and the refined quantities only reflect systematic effects.

2.3.2 Generating a structural model with the Reverse Monte Carlo method

One of the most popular implementations of the RMC method is called RMCProfile (Tucker et al., 2007); another one, focused on diffuse scattering, is called DISCUS (Proffen & Neder, 1997). Contrary to the model-fitting method just presented, the Reverse Monte-Carlo (RMC) method continuously shapes a structural model by applying random shifts to the atoms. The model, usually referred to as atomic configuration, is a box of arbitrary size and with periodic boundaries. Independent of what the initial model is based on (the actual crystallographic phase, a supergroup structure, or random arrangement), no symmetry constraint is applied in the configuration. Consequently, atoms in (initially) equivalent sites need not be found in symmetry-related positions after the first move, i.e. the configuration is practically a *P*1 unit cell. The only, straightforward requirements are the correct atomic number density and interatomic distances complying with both the hard-sphere repulsion potential and the fundamental atom connectivity. A sound choice for disordered crystalline materials is usually a multiple of the long-range unit cell, since this both maintains the basic polyhedral connectivity and can accommodate any possible local distortion.

During the RMC refinement, atoms are moved at random by shifts in any direction (usually up to 0.05 Å). Every *N* moves the PDF is calculated for the trial configuration and compared to the experimental PDF. The agreement between calculated and experimental functions is used to assess the quality of the model and drive the atomic configuration towards the minimum fit residual. For an arbitrary function F fitted by RMC, the agreement, X^2, is calculated as (Tucker et al., 2002):

$$X_F^2 = \frac{\sum_j \left[F_j^{calc} - F_j^{exp}\right]^2}{\sigma_F^2}.$$

Random atom moves are accepted if they improve the goodness of fit (i.e. lower the value of X^2), but also if they reduce it, within a tolerance reflecting the weight attributed to the dataset being fitted. An advantage over least-squares minimization, this allows avoiding local minima in analogy with simulated annealing, with the purely formal difference that the 'energy' function to minimize is fit residual.

Since the RMC refinement is set to search the absolute minimum and it does so with no explicit symmetry bias, it will be apparent that i) a distortion with respect to the starting model is always relatable to the data; ii) the RMC model should fit the experimental function better than a model conjured up by the user. Also, since the *P*1 configuration is defined by independent atoms

rather than by sites related by symmetry, vacant sites and mixed-occupancy sites are treated naturally, i.e. different species sit in different individual positions. The last advantage with respect to either reciprocal-space analysis or model fitting to PDF is that the model generated by RMC can optimize the fit to either PDF, $F(Q)$, or Bragg peaks, or any combination. This case, however, requires accurate weighting of the different datasets, which can prove tricky. On the one hand, weighting should reflect data quality, i.e. the uncertainty in each dataset; on the other hand, bad weighting can bias the final configuration towards only one aspect of the data. The main downside is that the experimental data may not be unambiguously consistent with a single model - there can be, in fact, a host of well-fitting solutions, particularly, in highly disordered materials. Anyway, the capability of generating unbiased, unconstrained models makes the RMC method extremely general, as shown, for instance, by the solution of bond-valence (Norberg et al., 2009) and spin ordering (Timm et al., 2016) problems.

References

Als-Nielsen, J., & McMorrow, D. (2011). Elements of modern X-ray physics. John Wiley & Sons.

Higher European Research Course for Users of Large Experimental Systems. (1993). Neutron and synchrotron radiation for condensed matter studies. J. Baruchel (Ed.). Springer-Verlag.

Coduri, M., (2012). Local disorder in doped ceria: a crystallographic study.

Dwiggins, C. W., & Park, D. A. (1971). Calculation of the intensity of secondary scattering of x-rays by non-crystalline materials. Acta Crystallographica Section A: Crystal Physics, Diffraction, Theoretical and General Crystallography, 27(3), 264-272.

Egami, T., & Billinge, S. J. L. (2003). Underneath the Bragg peaks: structural analysis of complex materials (Vol. 16). Elsevier.

Farrow, C.L., Juhas, P., Liu, J.W., Bryndin, D., Božin, E.S., Bloch, J., Proffen, T. and Billinge, S.J.L., (2007). PDFfit2 and PDFgui: computer programs for studying nanostructure in crystals. Journal of Physics: Condensed Matter, 19(33), 335219.

Fitch, A. N. (2004). The high resolution powder diffraction beam line at ESRF. Journal of Research of the National Institute of Standards and Technology, 109(1), 133.

Giacovazzo, C. (2002). Fundamentals of crystallography (Vol. 7). Oxford University Press, USA.

Hannon, A. C., Howells, W. S., & Soper, A. K. (1990). ATLAS: A suite of programs for the analysis of time-of-flight neutron diffraction data from liquid and amorphous samples. In Institute of Physics Conference Series (Vol. 107, pp. 193-211).

Hannon, A. C. (2005). Results on disordered materials from the GEneral Materials diffractometer, GEM, at ISIS. Nuclear Instruments and Methods in Physics Research Section A: Accelerators, Spectrometers, Detectors and Associated Equipment, 551(1), 88-107.

Keen, D. A. (2001). A comparison of various commonly used correlation functions for describing total scattering. Journal of Applied Crystallography, 34(2), 172-177.

Kisi, E. H., & Howard, C. J. (2012). Applications of neutron powder diffraction (Vol. 15). Oxford University Press.

Orlando, T., Capozzi, A., Umut, E., Bordonali, L., Mariani, M., Galinetto, P., Pineider, F., Innocenti, C., Masala, P., Tabak, F. and Scavini, M. (2015). Spin Dynamics in Hybrid Iron Oxide–Gold Nanostructures. The Journal of Physical Chemistry C, 119(2), 1224-1233.

Norberg, S. T., Tucker, M. G., & Hull, S. (2009). Bond valence sum: a new soft chemical constraint for RMCProfile. Journal of Applied Crystallography, 42(2), 179-184.

Placzek, G.. (1952). The scattering of neutrons by systems of heavy nuclei. Physical Review, 86: 377 –388.

Proffen, T., & Neder, R. B. (1997). DISCUS: A program for diffuse scattering and defect-structure simulation. Journal of applied crystallography, 30(2), 171-175.

Proffen, T., & Billinge, S. J. L. (1999). PDFFIT, a program for full profile structural refinement of the atomic pair distribution function. Journal of Applied Crystallography, 32(3), 572-575.

Qiu, X., Božin, E. S., Juhas, P., Proffen, T., & Billinge, S. J. (2004). Reciprocal-space instrumental effects on the real-space neutron atomic pair distribution function. Journal of Applied Crystallography, 37(1), 110-116.

Soper, A. K., & Egelstaff, P. A. (1980). Multiple scattering and attenuation of neutrons in concentric cylinders: I. Isotropic first scattering. Nuclear Instruments and Methods, 178(2-3), 415-425.

Soper, A. K. (2009). Inelasticity corrections for time-of-flight and fixed wavelength neutron diffraction experiments. Molecular Physics, 107(16), 1667-1684.

Soper, A.K. (2012). GudrunN and GudrunX: Programs for correcting raw neutron and x-ray total scattering data to differential cross section.

Stout, G. H., & Jensen, L. H. (1989). X-Ray Structue Determination: a Practical Guide. (Retroactive Coverage). John Wiley and Sons, Inc.(United States), 1989,, 453.

Thorpe, M. F. (1998). Local structure from diffraction. Springer Science & Business Media.

Timm, L., Tucker, M. G., Keen, D. A., Thygesen, P. M., Saines, P. J., & Goodwin, A. L. (2016). Exploration of antiferromagnetic CoO and NiO using reverse Monte Carlo total neutron scattering refinements. Physica Scripta, 91(11), 114004.

Tucker, M. G., Dove, M. T., & Keen, D. A., Total scattering and Reverse Monte Carlo modelling of disordered crystalline materials. Published in Thorpe, M. F. (Ed.). (2002). From semiconductors to proteins: Beyond the average structure. Springer Science & Business Media.

Tucker, M. G., Dove, M. T., & Keen, D. A. (2001). MCGRtof: Monte Carlo G (r) with resolution corrections for time-of-flight neutron diffractometers. Journal of applied crystallography, 34(6), 780-782.

Tucker, M. G., Keen, D. A., Dove, M. T., Goodwin, A. L., & Hui, Q. (2007). RMCProfile: reverse Monte Carlo for polycrystalline materials. Journal of Physics: Condensed Matter, 19(33), 335218.

Tucker, M. G., Dove, M. T., Goodwin, A. L., & Keen, D. A. (2012). RMCProfile user manual, code version 6.5.0.

Warren, B. E. (1969). X-ray Diffraction. Courier Corporation.

:Chapter 3:

Phase diagram of Pr-doped strontium titanate

The results presented here were published in Physical Review B: Checchia, S., Allieta, M., Coduri, M., Brunelli, M., & Scavini, M. (2016). Relaxor ferroeletric behavior in $Sr_{1-x}Pr_xTiO_3$: Cooperation between polar and antiferrodistortive instabilities. Physical Review B, 94(10), 104201)

3.1 Introduction

This chapter is about the determination of long-range symmetry in $Sr_{1-x}Pr_xTiO_3$ (SPTO), in the temperature range 90-650 K and in the Pr concentration range 0-15%. It should be self-explanatory why knowing the crystallographic phase at any point of the temperature/composition phase diagram is important. But a high accuracy in doing so is particularly important in the case of SPTO, as it sets the reference structure against which all the findings from the local probes will be discussed in the following chapter.

The structural information on SPTO available in the literature is limited and sometimes contradictory. For the $0.020 \leq x \leq 0.075$ range, Durán and co-workers (Durán et al, 2005; Durán et al, 2008) reported a cubic structure at room temperature; for x=0.150, their laboratory XRPD data suggested a polar *P*4*mm* symmetry, the same exhibited by the ferroelectric $BaTiO_3$. A polar space group was consistent with their observation of peaks in both dielectric permittivity and specific heat between 450 K and 500 K, which they attributed to a normal ferroelectric-paraelectric phase transition. But this interpretation was rejected by Ranjan and co-workers (Ranjan et al, 2008; Garg et al, 2009), who determined for $x \geq 0.05$ a centrosymmetric tetragonal phase (space group *I*4/*mcm*) at room temperature analogous to that of undoped $SrTiO_3$. While their finding was substantiated by using both high-resolution synchrotron X-ray diffraction and neutron diffraction, the lack of temperature-resolved XRPD data did not allow a thorough comparison with the antiferrodistortive (AFD) phase of $SrTiO_3$ in terms of the order parameters and, in turn, of the active instabilities.

In the following, it is showed that the room-temperature structure of SPTO is tetragonal (space group *I*4/*mcm*) for $x \geq 0.100$, whereas the samples with $x < 0.100$ are cubic at room temperature and undergo a phase transition to *I*4/*mcm* in the range $175 \leq T \leq 270$ K. The hitherto undetected structural phase transitions from *I*4/*mcm* to *Pm*-3*m* for the $0.020 \leq x \leq 0.150$ compositions are found to occur at higher temperature as x is increased. Only for x=0.150, thus, the phase transition temperature (T_C) agrees with the temperature of the dielectric permittivity peak observed by Durán et al.. At any composition, the temperature dependence of the tilt angle of the TiO_6 octahedra is consistent with a second order phase transition, in analogy with the phase transition in the undoped $SrTiO_3$. Neutron powder diffraction data are in good agreement with the magnitude of the AFD at 90 K, proving the high sensitivity of our XRPD data to the tilt of TiO_6 octahedra. In addition, refinements on

neutron diffraction data reveal an interesting trend in the oxygen anisotropic displacement parameters (ADPs).

3.2 Experimental

$Sr_{1-x}Pr_xTiO_3$ samples with x = 0, 0.020, 0.035, 0.050, 0.063, 0.075, 0,100, 0.125, 0.150 were prepared by a solid-state reaction using TiO_2 (Sigma-Aldrich 99.8%), $SrCO_3$ (Sigma-Aldrich 99.9%), Pr_6O_{11} (Sigma-Aldrich 99.9%). Stoichiometric mixtures of as-received reagents were uniaxially pressed into discs and fired in Pt crucibles for 4h at T = 1400 K, 4h at T = 1550 K, and finally 4 h at T = 1650 K until single-phase samples were obtained. Every stage of the reaction was carried out in static air atmosphere. Between each sintering stage, the disks were finely ground together and pressed into discs again.

Synchrotron X-ray powder diffraction (XRPD) measurements were carried out at the ID22 beamline of the ESRF (described in 3.1.1). High resolution diffraction patterns of all the samples were collected between 90 K and 650 K using incident photon beam with wavelength λ=0.31994 Å. 1 mm-diameter quartz capillaries were packed with finely ground SPTO powders and spun during measurement. XRPD patterns were collected following two routines: a) fixed temperature at 90 K and 295 K, and 10 temperatures in the range $300 \leq T \leq 650$ K for the samples with x = 0.020, 0.035, 0.050, 0.075 (6 temperature points were acquired for $SrTiO_3$). In this case, two scans $0° \leq 2\theta \leq 60°$ (Q_{max}=19 $Å^{-1}$) at a scan rate of 2°/min were summed; b) a single $0° \leq 2\theta \leq 40°$ scan (Q_{max}=13 $Å^{-1}$) at a 4°/min scan rate while heating the sample at 1 K/min.

Neutron powder diffraction measurements were carried out at the GEM diffractometer at ISIS (described in 3.1.2) on 8 g of the samples with x=0, 0.035, 0.075, 0.150. Each sample was contained in a cylindrical vanadium can (0.8 mm diameter, 50 mm height) and measured for 6 h at 90, 295, 450, and 600 K temperature. The scattering of instrument background, sample container, and V/Nb rod was also measured and used for data correction.

Rietveld analysis was performed through the GSAS program and its graphical interface EXPGUI (Larson and von Dreele, 2000; Toby, 2001). The background was subtracted using shifted Chebyshev polynomials. For X-ray data, the diffraction peak profiles were fitted with a Thompson-Cox-Hastings pseudo-Voigt function (Thompson et al., 1997) corrected for peak asymmetry (Finger et al., 1994); the absorption correction for the Debye-Scherrer geometry was applied through the empirical Lobanov formula (Lobanov and Alte da Veiga, 1998); the anomalous scattering parameters, f' and f'', used are those reported by Brennan and Cowan (1992). In the case of neutrons, the patterns were corrected for absorption during reduction of the raw data using the Mantid software available at GEM; peak shape was reproduced by the

TOF profile function 2 (see 3.1.2); the structural model was refined against four TOF patterns, namely, those from detector banks 2, 3, 4, 5 (Q_{max}=13 Å^{-1}). In the last refinement cycles all the parameters were refined: cell parameters, one atomic position, thermal displacement parameters (anisotropic thermal parameters were used with neutron data), four to eight background parameters, diffractometer zero, overall scale factor, and four profile parameters.

3.3 Results

3.3.1 Tetragonal-cubic phase transition

The XRPD patterns at 90 K of all the SPTO samples are best fitted by a tetragonal phase with I4/mcm symmetry. The unit cell adopted in the tetragonal phase is a $\sqrt{2}\ a_p \times \sqrt{2}\ a_p \times 2\ a_p$ supercell of the parent cubic cell (Figure 3.1), where a_p is the cubic cell parameter (a_p ~ 3.90 Å).

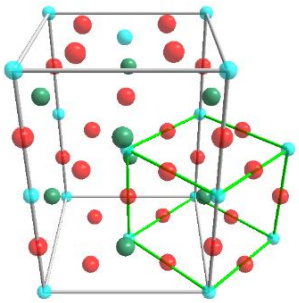

Figure 3.1: the cubic (green edges) and the tetragonal (grey) unit

On heating, every SPTO sample undergoes a structural transition from the tetragonal I4/mcm phase to the Pm-3m cubic perovskite phase, depending on Pr concentration, at a temperature $175 \leq T_C \leq 470$ K.

Figures 3.2 and 3.3 show sections of selected XRPD patterns that detail the structural evolution on cooling under T_C. At temperatures below T_C, the (200) peak of the cubic perovskite is split into two components of relative intensity 1:2 (Figure 3.2); the low-*d* and high-d components are indexed, respectively, as (220) and (004) in the tetragonal phase. As the temperature is lowered, the cell volume is reduced largely as a result of striction along the direction of a, while the c-axis has a near-zero dependence on temperature (panels A and C in Figure 3.4). The result is a continuous increase in tetragonality on cooling for each sample (Figure 3.4, panel D). But as the pseudo-cubic cell parameters, c_p and a_p, drift increasingly apart with Pr concentration, there is also a remarkable increase in tetragonality caused by

Sr/Pr substitution (note the shift to the curves in Figure 3.4 panel D). It must be noted that for x<0.050 tetragonality is tiny and not resolved even with the formidable Q-resolution of ID22. Shown in Figure 3.3, a set of superstructure reflections is visible under T_C in the patterns of every SPTO sample. Because these peaks arise by condensation of the out-of-phase tilt of TiO_6 octahedra along the <001> direction, they make the difference between the centrosymmetric *I*4/*mcm* and the non-centrosymmetric *P*4*mm* phase. The continuous increase in the intensity of superstructure peaks, as the temperature is lowered, reflects the increasing tilt angle of the octahedra.

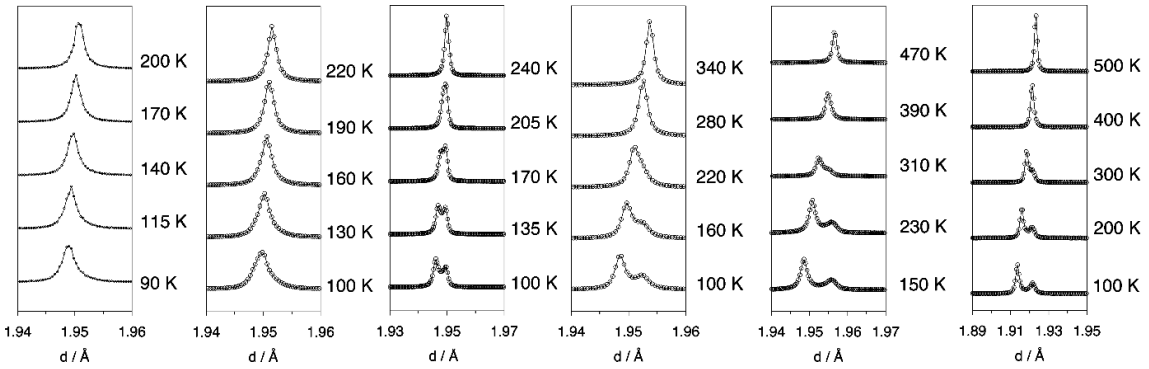

Figure 3.2: Temperature evolution of the cubic 200 reflection of the cubic cell splitting into the low-d 220 and high-d 004 tetragonal reflections on cooling below T_C. From left to right, the panels show x=0.020, 0.035, 0.050, 0.075, 0.100, 0.150.

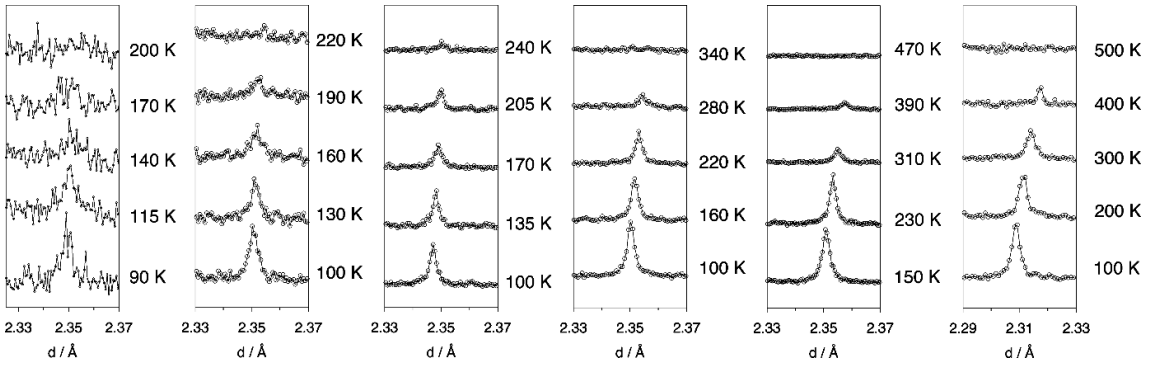

Figure 3.3: Temperature evolution of the 211 reflection of the tetragonal cell, indicating the decrease in octahedral tilt angle on heating at T_C. From left to right, the panels show x=0.020, 0.035, 0.050, 0.075, 0.100, 0.150.

As confirmed by symmetry analysis by the ISODISTORT program (Campbell et al., 2006), tilt angle and tetragonality are, respectively, the primary and secondary order parameters of the structural phase transition in SPTO, in analogy with the AFD transition in undoped $SrTiO_3$. The amplitude of tetragonal strain is readily calculated from the phase parameters as $\eta=c_p/a_p-1$, where a_p and c_p are the pseudo-cubic cell parameters showed in Figure 3.4. The octahedral tilt angle is calculated as

$$\phi = \text{atan}(1 - 4x_{O(8h)})$$

with $x_{O(8h)}$ the x coordinate of the oxygen atom in the *8h* Wyckoff site (x, x+1/2, 0), the only positional degree of freedom in the *I*4/*mcm* structure.

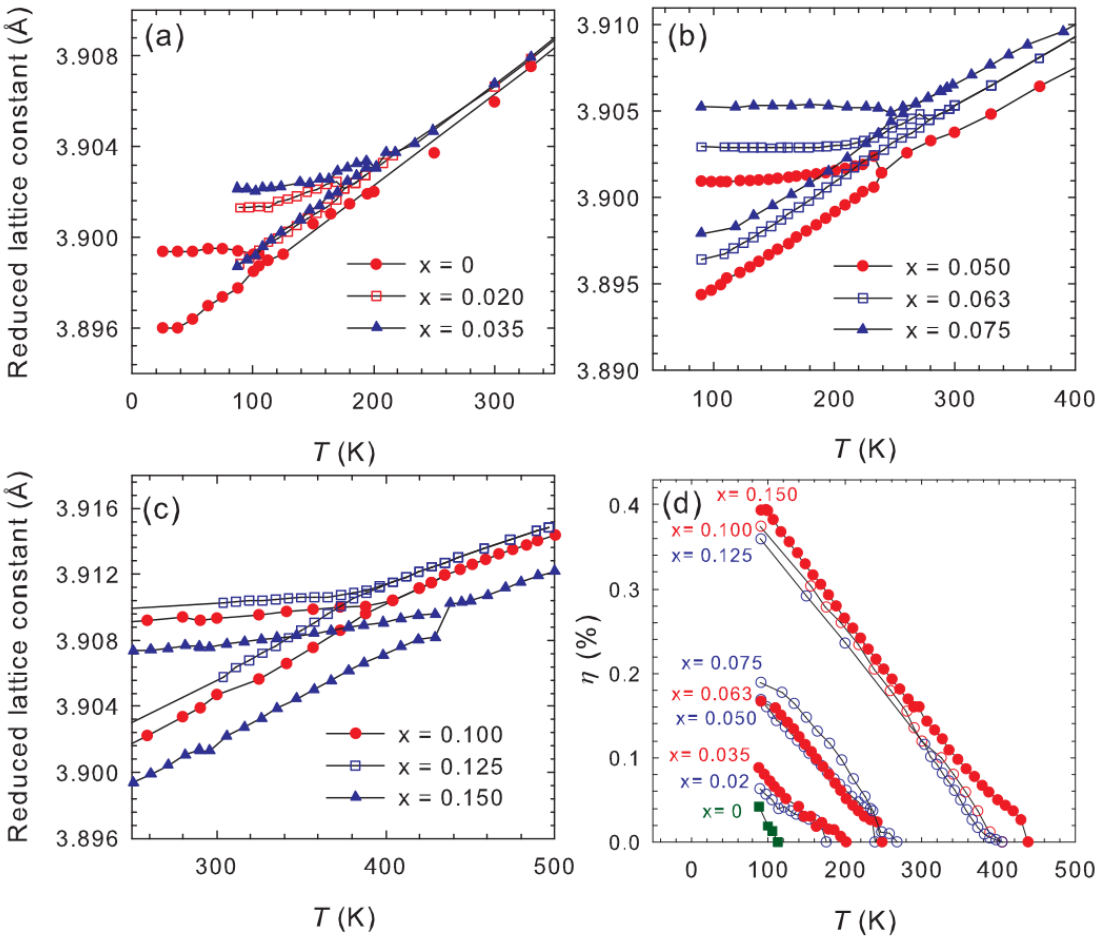

Figure 3.4: (a–c) Temperature evolution of the cell parameters reduced to the cubic parent cell. The panels show subsequent groups of three compositions. Below the transition temperature at TC the c axis is greater than the a axis. (d) Cell tetragonality expressed as $\eta = c_p/a_p - 1$ as a function of temperature for all the samples. Data for $SrTiO_3$ for T < 90 K are taken from Okazaki and Kawaminami (1973).

The Sr/Pr substitution at the perovskite A-site has a huge effect on the magnitude of both tetragonality and tilt angle (panel D in Figure 3.4 and Figure 3.5, respectively): because of the increase in T_C obtained by doping, at 100 K the tilt angle varies between 2.1° and 5.2° depending on x while undoped $SrTiO_3$ is very close to the tetragonal-cubic phase transition. Not only, however, the octahedral rotations are frozen at a higher temperature, but the tilt angles of the doped samples are considerably larger than the maximum tilt angle allowed in undoped SrTiO3 (~2°). The same trend holds for tetragonal strain, as the maximum value of η for x=0.15 is four times as large as the value of η at 5 K for undoped $SrTiO_3$.

The temperature dependence of the primary order parameter of the AFD phase transition, ϕ, is compared with a pure displacive second-order behaviour and fitted by the mean-field equation

$$\phi(T) = \phi(0) \times \left(1 - \frac{T}{T_C}\right)^{\beta}$$

where $\phi(0)$ is the extrapolated tilt angle at zero temperature and β the critical exponent. A critical exponent set to β=0.50 returns the best fits to all the ϕ vs T curves (Figure 3.5), evidencing no deviations from a pure second-order transition.

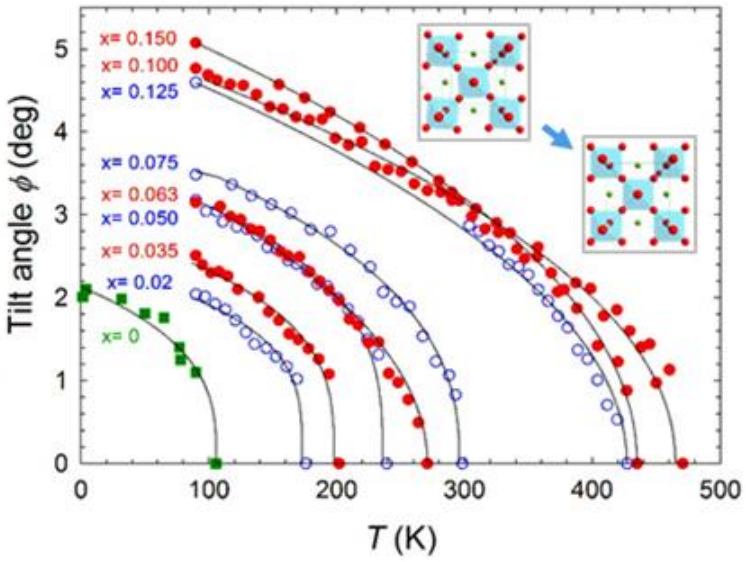

Figure 3.5: Temperature evolution of the tilt angle for $SrTiO_3$ and all the SPTO samples. The insets show the tetragonal cell viewed along the [001] direction, depicting the out-of-phase tilt of the TiO6 octahedra and the zero-tilt arrangement. The solid lines are the best fits to the mean field equation using a critical exponent β=0.5.

3.3.2 Comparison with neutron diffraction

Because the primary distortion involved in the AFD phase transition is purely oxygen-related, the reciprocal-space analysis of neutron powder diffraction data of a small but representative part of the samples and the temperatures (see 3.2) measured by XRPD is reported, in order to confirm the results just presented. As one can infer from the coherent neutron scattering lengths and molar fractions in SPTO, oxygen is the stronger neutron scatterer in all these samples (tables of the neutron scattering lengths relevant to this work are reported in the

Appendix to chapter 4). In Figure 3.6 the accuracy of the order parameters returned by the Rietveld analysis of XRPD data is assessed by comparing them to the respective values obtained by Rietveld analysis of NPD data. While for x=0.150 the agreement is excellent throughout the 90-600 K temperature range (Figure 3.6, panels B and D), both ϕ and η are slightly underestimated by XRPD for x=0.075, 0.035, and pure $SrTiO_3$ (Figure 3.6, panels a and c). The tilt angle discrepancy for x=0.075 is about 0.5° (12.5%), but it becomes almost 1° (100%) for $SrTiO_3$. Nonetheless, the sheer increase in both tilt and tetragonality obtained by Pr-doping is confirmed by the NPD data, especially since the XRPD and NPD values for x=0.150 are remarkably close.

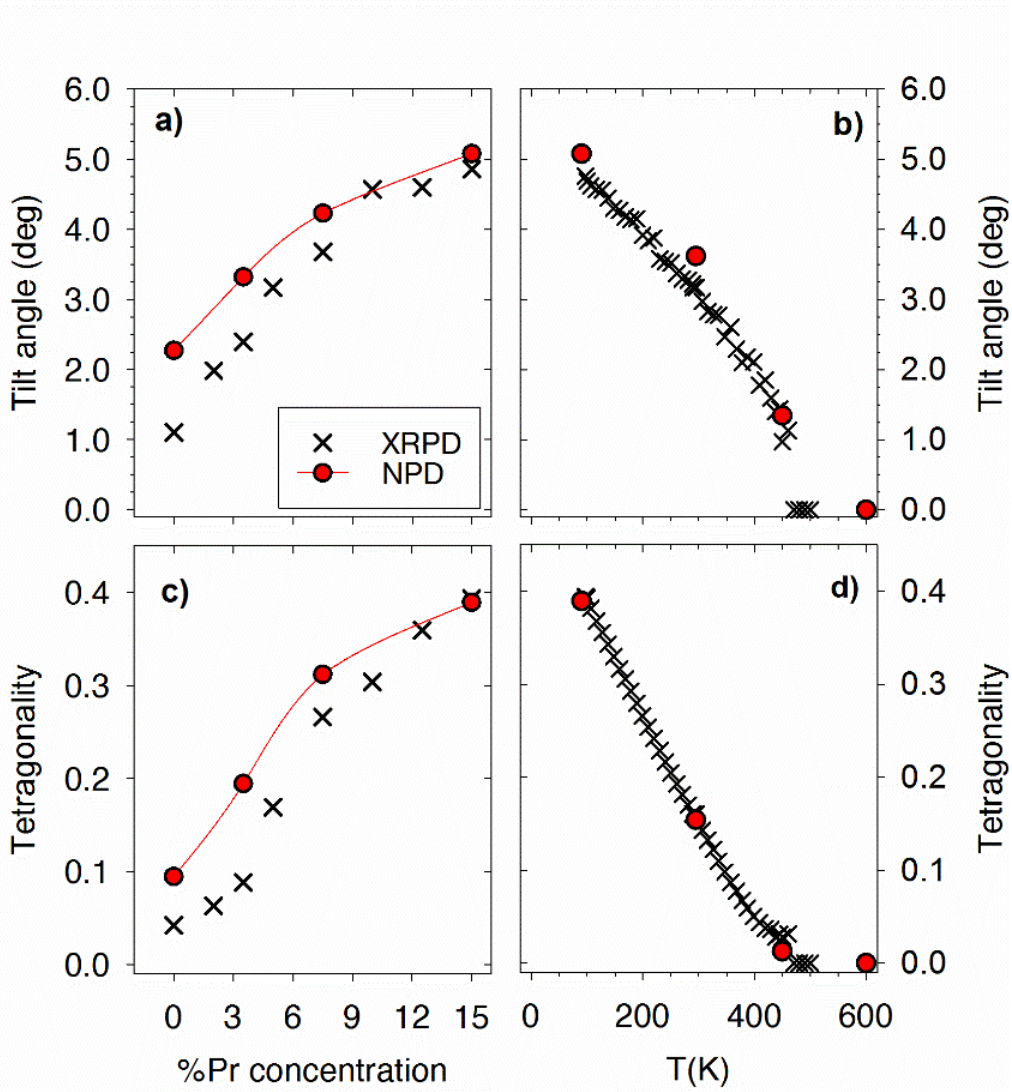

Figure 3.6: (a) Tilt angle at 90 K versus Pr concentration; (b) Tilt angle versus temperature for x=0.150; (c) Tetragonality at 90 K versus Pr concentration; (d) Tetragonality versus temperature for x=0.150. In all panels full red circles are neutron data, black crosses are X-ray data.

The refined phases at 90 K of the four samples analysed are reported in Table 3.1. Note that

not only the values of the isotropic thermal parameters (U) of the cations increase linearly with x, but the U_{33} component of the anisotropic ADP of the oxygens in the *8h* site increases much faster than the other two, U_{11} and U_{12}. At the same time, the thermal ellipsoids of the oxygens in the *4a* site (0,0,1/4) have a much larger component in the *xy* plane than they have along *z*. This behaviour, though, does not seem to depend on Pr concentration. Figure 3.7 shows the tetragonal unit cell corresponding to the refined phase of x=0.150 at 90 K.

Table 3.1: Results of the Rietveld refinements on NPD data at 90 K. All phases belong to the I4/mcm space group, by which $U_{11}=U_{22}$ and $U_{13}=U_{23}=0$. The residual R(F^2) is given relative to the NPD pattern recorded by the detector bank 5 of the GEM diffractometer.

Atom	Wyckoff	x	y	z	$U_{iso}\times10^2$ (Å^2)	$U_{11}\times10^2$ (Å^2)	$U_{33}\times10^2$ (Å^2)	$U_{12}\times10^2$ (Å^2)
$SrTiO_3$		**a=5.5140(1) Å, c=7.8069(3) Å**				**wRp=3.85%, R(F^2)=4.80%**		
Sr	*4b*	0	0.5	0.25	0.297(9)	--	--	--
Ti	*4c*	0	0	0	0.254(9)	--	--	--
O1	*4a*	0	0	0.25	--	0.82(1)	0.21(1)	
O2	*8h*	0.2437(1)	0.7437(1)	0	--	0.34(5)	0.50(7)	0.15(6)
x=0.035		**a=5.5121(1) Å, c=7.8105(2) Å**				**wRp = 3.51%, R(F^2) = 3.72%**		
Sr/Pr	*4b*	0	0.5	0.25	0.351(9)	--	--	--
Ti	*4c*	0	0	0	0.29(1)	--	--	--
O1	*4a*	0	0	0.25	--	0.70(5)	0.18(8)	
O2	*8h*	0.2358(1)	0.7358(1)	0.25	--	0.46(2)	0.80(6)	0.04(4)
x=0.075		**a=5.5061(1) Å, c=7.8111(1) Å**				**wRp = 3.08%, R(F^2) = 4.63%**		
Sr/Pr	*4b*	0	0.5	0.25	0.41(1)	--	--	--
Ti	*4c*	0	0	0	0.336(8)	--	--	--
O1	*4a*	0	0	0.25	--	0.68(3)	0.04(5)	
O2	*8h*	0.2316(1)	0.7316(1)	0.25	--	0.48(1)	0.79(4)	0.09(3)
x=0.150		**a= 5.5031(1) Å, c = 7.8131(1) Å**				**wRp = 3.40%, R(F^2) = 6.11%**		
Sr/Pr	*4b*	0	0.5	0.25	0.47(1)	--	--	--
Ti	*4c*	0	0	0	0.40(1)	--	--	--
O1	*4a*	0	0	0.25	--	0.86(3)	0.05(5)	
O2	*8h*	0.2280(3)	0.7280(3)	0.25	--	0.51(1)	1.08(4)	0.19(3)

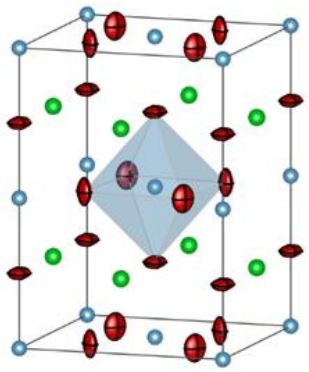

Figure 3.7: Tetragonal unit cell for x=0.150 at 90 K obtained from NPD data. For the two oxygen sites the 98% probability ellipsoids are shown.

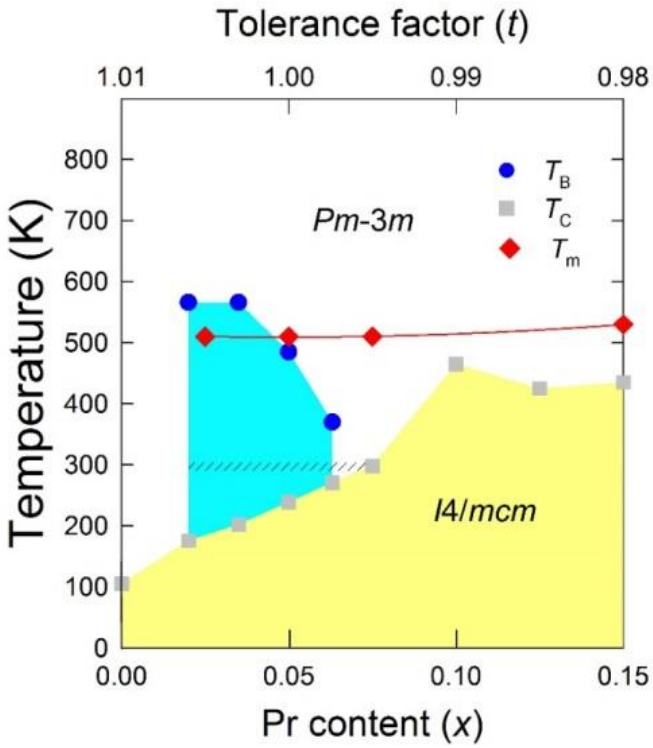

Figure 3.8: Phase diagram proposed for SPTO. Squares indicate T_C, the temperature of the long-range structural phase transition; diamonds indicate T_M, the onset of the dielectric peak observed in ref. (Duran et al., 2005). The secondary abscissa reports the perovskite tolerance factor relative to x in the primary abscissa. The region delimited by the Burns temperature (T_B) is shaded in blue.

3.3.3 Electrostrictive strain

Having characterised the long-range structure of SPTO as purely AFD and centrosymmetric, the focus here is on the structural response in the temperature range around T_M=500 K, where T_M is the temperature of the dielectric peak observed for SPTO (Duran et al., 2005). In order to stay clear of the condensed AFD mode and highlight only the structural distortion related to the relaxor FE character, only the cubic phase of $x \leq 0.075$ samples is considered (see phase diagram in Figure 3.8). The data considered here are the fixed-temperature, high-Q_{max}, high-counting time XRPD patterns collected between 300 K and 650 K, as described in 3.2.

Figure 3.9 shows the variation of the lattice parameter for the x=0.035 sample in the temperature range well into the cubic regime. By cooling down from T=650 K, the temperature evolution of the a cell parameter follows a Debye-like linear contraction until it reaches a critical temperature; by further cooling, an anomalous dilatation results in a different a vs T slope. All the samples in the $0.020 \leq x \leq 0.063$ range exhibit a similar departure from the expected linear thermal contraction, which, in absence of applied electric field, can be attributed to spontaneous electrostrictive strain (Burns and Dacol, 1983; Cross, 1987). Thus, T_B denotes the critical Burns temperatures observed for these samples.

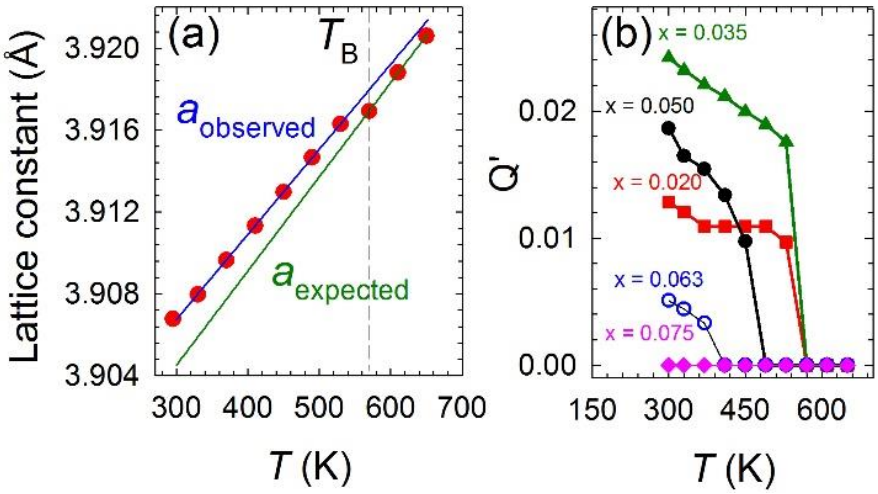

Figure 3.9: (a) Temperature evolution of the cubic cell parameter a for x=0.035: full circles are observed values; solid lines are aobserved (blue) and aexpected (green) defined in the text. (b) The order parameter of electrostrictive strain (Q'= √(QP2))

For the x=0.020, 0.035 samples, the critical Burns temperatures are higher than the temperature of dielectric relaxation (T_M). Plotting all the T_B critical temperatures obtained in the T-x phase diagram of SPTO (Figure 3.8) evidences a distinct phase regime within the cubic region. Electrostrictive strain is evaluated as $a_{observed}$–$a_{expected}$ = QP^2: $a_{observed}$ is the

observed lattice parameter; $a_{expected}$ is the lattice parameter obtained by linear fitting the data points above T_B; P is the local polarization; Q is a constant factor. Thus, the anomalous temperature evolution of the cubic lattice parameter below T_B translates in all the samples into a steep rise of $Q' = \sqrt{(QP^2)}$, a quantity linearly dependent on polarization (panel B in Figure 3.9).

In the samples with x= 0.020 and x=0.035, electrostrictive strain sets in at a higher T_B than in x= 0.050 and x=0.063. Only for Pr concentrations up to x=0.035, thus, T_B is consistent with the temperature of the dielectric anomaly, T_M, (see Fig.3.8); as previously proposed by Ranjan et al. (Ranjan et al., 2008), electrostrictive strain is a likely indication of the emergence of dipole moment through the formation of local FE ordering. Differently, the decrease in T_B for x=0.050 and x=0.063, and so the absence of any electrostrictive effect at x=0.075, strongly suggests a drop in spontaneous polarization. One can tentatively ascribe this polarization drop to the stronger long-range AFD instability setting in above x=0.075, which counters the FE zone-centre instability, in this case, in terms of inhibited local order and, in turn, absence of electrostrictive strain. With no electrostrictive strain detectable for $x \geq 0.075$, there is no unifying, composition-independent evidence of a FE state in SPTO.

3.4 Discussion

The low-temperature structure of SPTO determined here for every x agrees with the one proposed by Garg et al. (Garg et al., 2009) on highly doped SPTO at room temperature. Thus, their finding was extended to all Pr concentrations, noting that only the samples with $x \geq 0.100$ are tetragonal at room temperature, and that the phase transition occurs at temperatures 175 K $\leq T \leq$ 270 K for Pr concentrations in the range $0.020 \leq x \leq 0.075$. Therefore, a long-range FE transition in the range 90 K $\leq T \leq$ 650 K, as proposed by Duran et al., can be excluded.

Although the centrosymmetric *I*4/*mcm* phase and the corresponding polar phase obtained by mixing with a Γ mode (space group *I*4*cm*) cannot be ultimately told apart using XRPD, there are several reasons why the phase transition reported here is decoupled from the dielectric permittivity anomalies in SPTO. First, the dielectric permittivity anomalies are observed at $T_M \approx 500$ K almost independent of composition, but T_M never matches our measured T_C other than for x=0.150. Second, the order parameters (ϕ, η) and the critical temperature (T_C) of the AFD phase transition are amplified by increasing Pr concentration, but a stronger AFD instability is expected to suppress a long-range structural FE transition (Zhong and Vanderbilt, 1995). Third, all the samples with $x \leq 0.075$ are cubic at T_M, and in some of them ($0.020 \leq x \leq 0.0625$) electrostrictive strain seems to be the structural response actually related to

the freezing of local electric dipoles.

The tetragonal phase of SPTO also matches the AFD structure exhibited by $SrTiO_3$ under 105 K, and by $EuTiO_3$ under 215 K (Allieta et al., 2012; Goian et al., 2012). The *I*4/*mcm* space group is simply obtained by condensing the tilt of the TiO_6 octahedra along the c-axis, a tilt pattern expressed with $a^0a^0c^-$ in the Glazer notation (Glazer, 1972). As the tolerance factor in SPTO decreases with *x* (*t*~0.98 at 15% doping), in the light of the smaller ionic radius of Pr^{3+} with respect to Sr^{2+} (1.19 Å and 1.44 Å), one might have expected Pr to induce one effect between a more complex, lower-symmetry tilt pattern, a ferroelectric distortion, or, more simply, a larger distortion of the existing $SrTiO_3$ structure. In fact, an A cation smaller than Sr in $SrTiO_3$ is underbonded (tolerance factor smaller than 1), so its anion coordination could be optimized primarily through octahedral rotations, but also through FE distortions (Woodward, 1997; Benedek and Fennie, 2013). Having ruled out a long-range FE structure in SPTO, a change from the $a^0a^0c^-$ tilt pattern can also be proved incompatible with these XRPD data.

The distortion associated to the R4+ irrep of the cubic *Pm*-3*m* space group present in all these perovskites defines the subgroups *I*4/*mcm*, *Imma*, and *R*-3*c*, if a single tilt amplitude is considered and allowing tilt components to be directed along one, two, or all three axes, respectively (Howard and Stokes, 1998). From the peak intensities in the powder diffraction patterns it was possible to select *I*4/*mcm* between the three types of distortion, thus, also to rule out further symmetry reductions associated with the R4+ irreducible representation (*C*2/*m*, *C*2/*c*, and *P*-1). High-quality XRPD data also helped ruling out other possible long-range distortions involving the opposite-sign tilt pattern ($a^0a^0c^+$) invoked by the M3+ irrep (Howard and Stokes, 1998). A distortion generated by its superposition to R4+, for instance, is observed in $Sr_{1-x}Ca_xTiO_3$, another relaxor FE at small dopant concentrations (<5%) (Ranjan et al., 2000).

Therefore, the effect of Pr doping on the long-range structure is to increase the temperature at which the R4+ mode condenses into the tetragonal structure, and to increase the amplitude of the distortion well over that observed in undoped $SrTiO_3$, as demonstrated by the increase in the order parameters ϕ and η as a function of *x*. Ultimately, in view of the increase in the cation ADPs with doping, and of the trend in the oxygen ADPs revealed by neutron diffraction, further insights on the SPTO structure can only be obtained through local structural probes like Raman spectroscopy and Pair Distribution Function.

References

Allieta, M., Scavini, M., Spalek, L.J., Scagnoli, V., Walker, H.C., Panagopoulos, C., Saxena, S.S., Katsufuji, T. & Mazzoli, C. (2012). Role of intrinsic disorder in the structural phase transition of magnetoelectric EuTiO 3. Physical Review B, 85(18), 184107.

Benedek, N. A., & Fennie, C. J. (2013). Why are there so few perovskite ferroelectrics?. The Journal of Physical Chemistry C, 117(26), 13339-13349.

Burns, G., and Dacol, F. H. (1983). Crystalline ferroelectrics with glassy polarization behavior. Physical Review B, 28(5), 2527.

Campbell, B. J., Stokes, H. T., Tanner, D. E. and Hatch, D. M. (2006). ISODISPLACE: An Internet Tool for Exploring Structural Distortions. Journal of Applied Crystallography 39, 607-614.

Cross, L. E. (1987). Relaxor ferroelectrics. Ferroelectrics, 76(1), 241-267.

Durán, A., Martínez, E., Díaz, J. A., & Siqueiros, J. M. (2005). Ferroelectricity at room temperature in Pr-doped SrTiO3. Journal of applied physics, 97(10), 4109.

Durán, A., Morales, F., Fuentes, L., & Siqueiros, J. M. (2008). Specific heat anomalies at 37, 105 and 455 K in SrTiO3: Pr. Journal of Physics: Condensed Matter, 20(8), 085219.

Finger, L. W., Cox, D. E., & Jephcoat, A. P. (1994). A correction for powder diffraction peak asymmetry due to axial divergence. Journal of Applied Crystallography, 27(6), 892-900.

Garg, R., Senyshyn, A., Boysen, H., & Ranjan, R. (2009). Structure of the noncubic phase in the ferroelectric state of Pr-substituted SrTiO 3. Physical Review B, 79(14), 144122.

Glazer, A. M. (1972). The classification of tilted octahedra in perovskites. Acta Crystallographica Section B: Structural Crystallography and Crystal Chemistry, 28(11), 3384-3392.

Goian, V., Kamba, S., Pacherová, O., Drahokoupil, J., Palatinus, L., Dušek, M., Rohlíček, J., Savinov, M., Laufek, F., Schranz, W. and Fuith, A. (2012). Antiferrodistortive phase transition in EuTiO 3. Physical Review B, 86(5), 054112.

Howard, C. J., & Stokes, H. T. (1998). Group-theoretical analysis of octahedral tilting in perovskites. Acta Crystallographica Section B: Structural Science, 54(6), 782-789.

Larson, A. C. and Von Dreele, R. B. (2000). General Structure Analysis System (GSAS) (Report LAUR 86-748), Los Alamos, National Laboratory.

Lobanov, N. N. and Alte da Veiga, L. (1998). 6th European Powder Diffraction Conference,

Abstract P12-16.

Okazaki, A. and Kawaminami, M. (1973). Material Research Bulletin 8, 545.

Ranjan, R., Pandey, D., & Lalla, N. P. (2000). Novel features of $Sr_{1-x}Ca_xTiO_3$ phase diagram: evidence for competing antiferroelectric and ferroelectric interactions. Physical Review Letters, 84(16), 3726.

Ranjan, R., Garg, R., Hackl, R., Senyshyn, A., Schmidbauer, E., Trots, D., & Boysen, H. (2008). Onset of spontaneous electrostrictive strain below 520 K in Pr-doped $SrTiO_3$. Physical Review B, 78(9), 092102.

Thompson, P., Cox, D. E., & Hastings, J. B. (1987). Rietveld refinement of Debye–Scherrer synchrotron X-ray data from Al2O3. Journal of Applied Crystallography, 20(2), 79-83.

Toby, B. H. (2001). EXPGUI, a graphical user interface for GSAS, Journal of Applied Crystallography 34, 210–213.

Woodward, P. M. (1997). Octahedral tilting in perovskites. II. Structure stabilizing forces. Acta Crystallographica Section B: Structural Science, 53(1), 44-66.

Zhong, W., & Vanderbilt, D. (1995). Competing structural instabilities in cubic perovskites. Physical Review Letters, 74(13), 2587.

Appendix

Neutron powder diffraction patterns

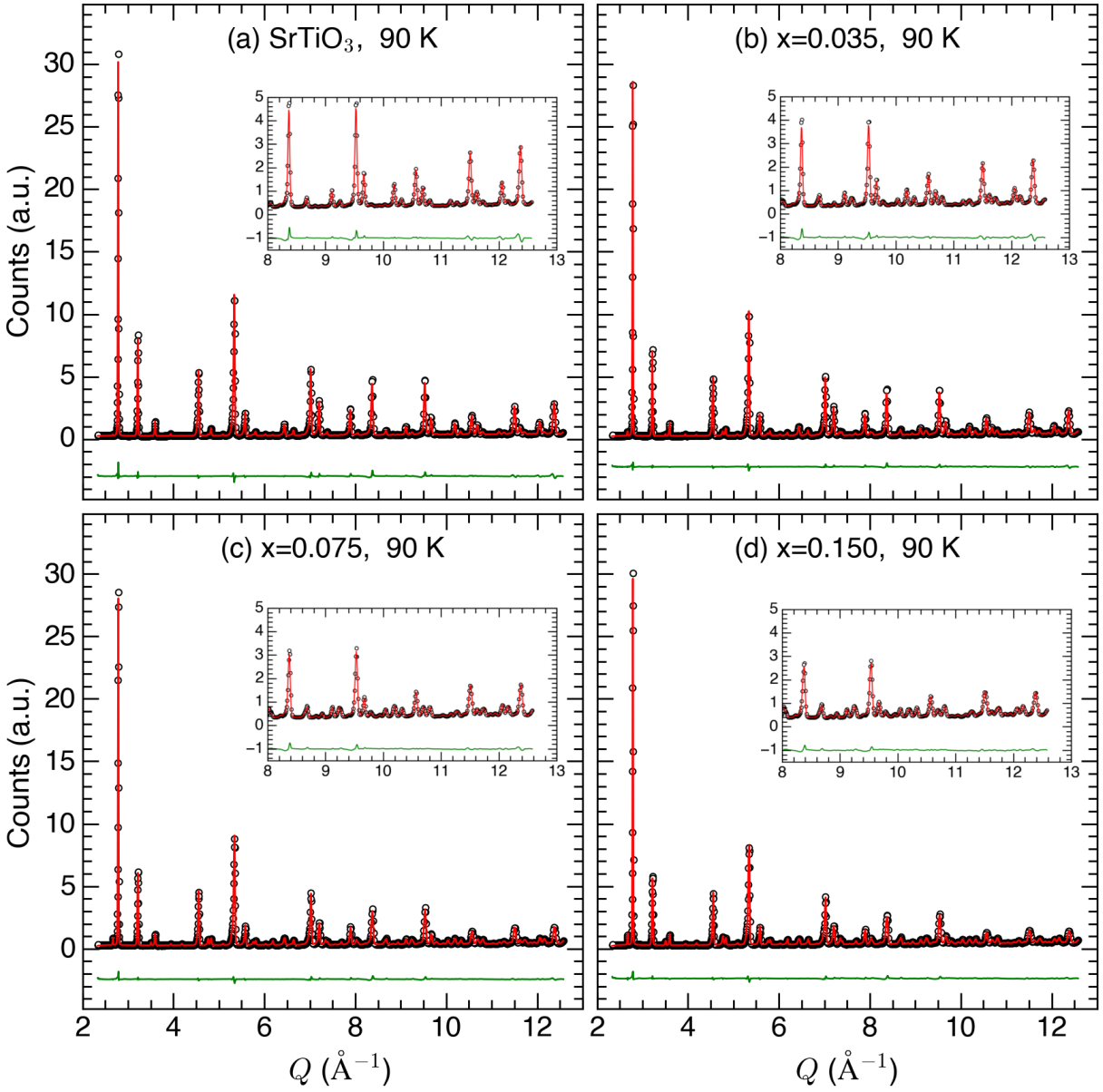

:Chapter 4:

Local structure of Pr-doped strontium titanate

4.1 Introduction

In this chapter, we look at local structural features by means of the Pair Distribution Function approach (PDF), whose basics have been covered in Chapter 2. In view of the long-range centrosymmetric structure determined in Chapter 3, the present PDF analysis is used to disclose atomic displacements with no long-range coherence, which do not show up in reciprocal-space patterns except being hinted at by the trend of atomic displacement parameters. Cation displacements with respect to the centre of the respective oxygen coordination cages would explain the emergence of electric dipoles, which would, in turn, shed light on the microscopic mechanism by which $Sr_{1-x}Pr_xTiO_3$ (SPTO) develops relaxor ferroelectricity.

Although ABO_3 perovskites are probably the most studied class of materials, many structural aspects of their phase transitions and their local disorder have been cleared up only very recently thanks to PDF. In $BaTiO_3$, for instance, the local off-center displacements of Ti atoms along <111> directions were reconciled with the structural phase transitions by a recent neutron PDF approach based on symmetry decomposition (Senn et al., 2016). PDF was key to determining the split chemical environment of Sr and Ba in the local structure of Sr-doped $BaTiO_3$ (Levin et al., 2014). Cation ordering and local atomic displacements in the $BiScO_3$-$PbTiO_3$ solid solution were mapped out of neutron PDF by a reverse Monte Carlo study (Datta et al., 2016). By an analogous approach, short-range order showed up in $Ca(Zr,Ti)O_3$ (Krayzman and Levin, 2007). Cation ordering and correlated displacements were studied by reverse Monte Carlo in $Bi(Ti, Fe, Mg)O_3$ (Chong et al., 2012), another Pb-free ferroelectric. PDF also help elucidating the effect on ferroelectricity of the stereochemically-active Pb^{2+} located in the A-site of $SrTiO_3$ (Laurita et al., 2015).

In analogy to these cases (and countless more) local structure is used to explain the emergence of the relaxor behaviour in SPTO upon Pr/Sr substitution. In particular, the aim of the analysis presented in this chapter is to pin down as accurately as possible the structural mechanism breaking centrosymmetry in doped $SrTiO_3$. The highly symmetric structure of SPTO is an advantage in some respects, for instance, because many of the first PDF peaks are well apart, but challenging in some others, since certain atom pairs systematically overlap (see Figure 4.1). What follows presents the results of two different approaches to PDF analysis. The basic reason for using the two methods is that two sets of data at our disposal, X-ray PDF (XPDF) and neutron PDF (NPDF), highlight different features of the local structure of SPTO. Since XPDF is more sensitive to the chemical environment of metal atoms (see form factors in Figure 4.2), we first look for macroscopic cation displacements or, in general, local breakings of the long-range symmetry. This is done by testing the agreement of structural models generated by applying either the zone-centre, ferroelectric (FE) instability (i.e. cation off-centering) or by the zone-boundary, antiferrodistortive (AFD) instability (i.e. octahedral tilt) to the cubic

perovskite structure; consequently, the structural parameters of the target phase are refined against the experimental PDF by least-squares cycles until reaching optimum agreement. The Reverse Monte-Carlo (RMC) method, here applied to neutron PDF, takes the opposite approach: experimental PDF is used to generate a model – by moving atoms randomly and accepting changes based on the agreement between calculated and experimental PDF. The RMC method is a natural choice to fit neutron PDF in the case of SPTO: because of the large scattering cross-section of oxygen (Figure 4.1) and the systematically overlapping interatomic distances in the perovskite structure (see Figure 4.2), only an unconstrained refinement is able to evidence complex distortions originating from multiple atoms, such as those involving the superposition of FE and AFD modes.

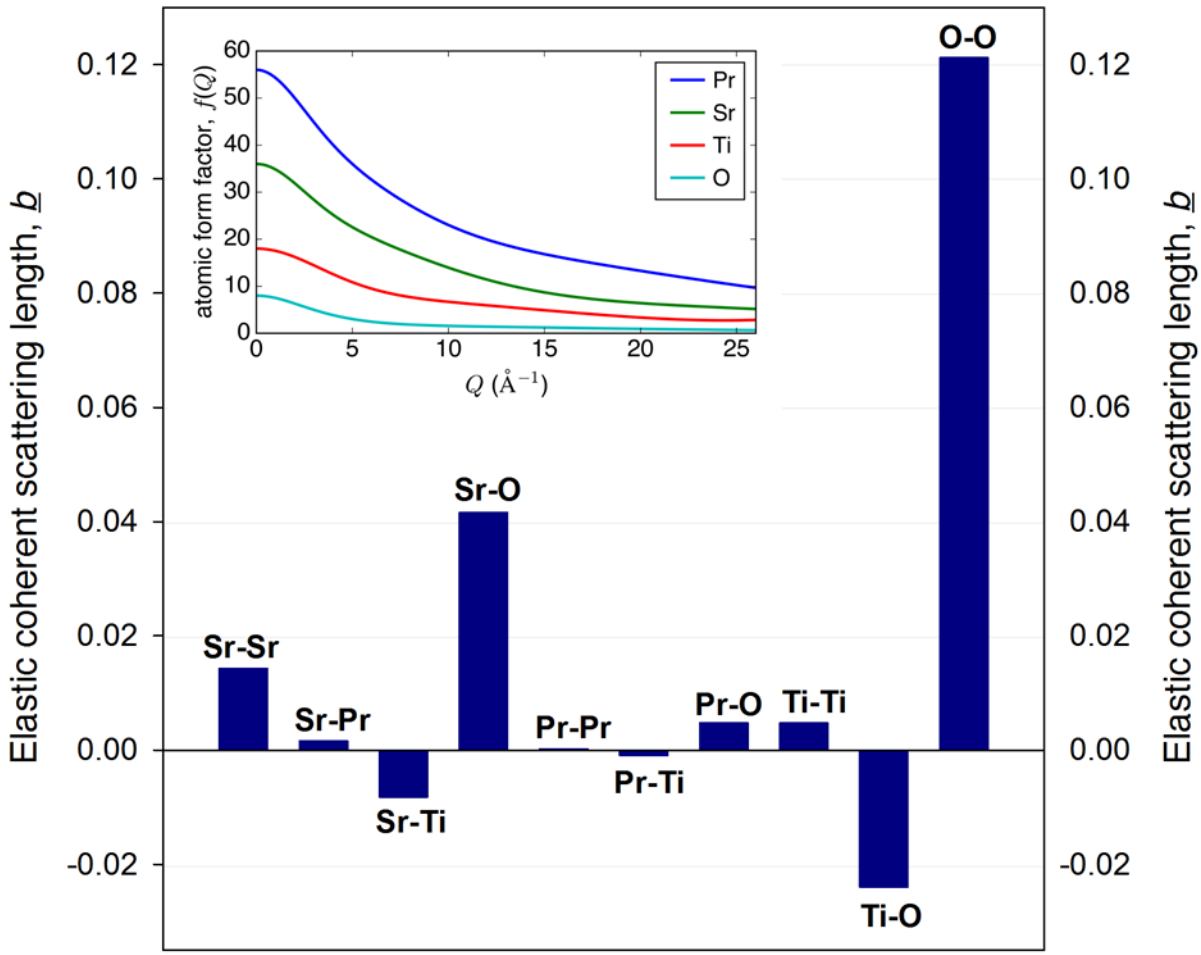

Figure 4.1: Histogram of isotope-averaged, coherent neutron scattering lengths for atom pairs in SPTO (x =0.150). Inset: X-ray scattering atomic form factors for SPTO. Neutron scattering lengths are taken from Ref. (Sears, 1991).

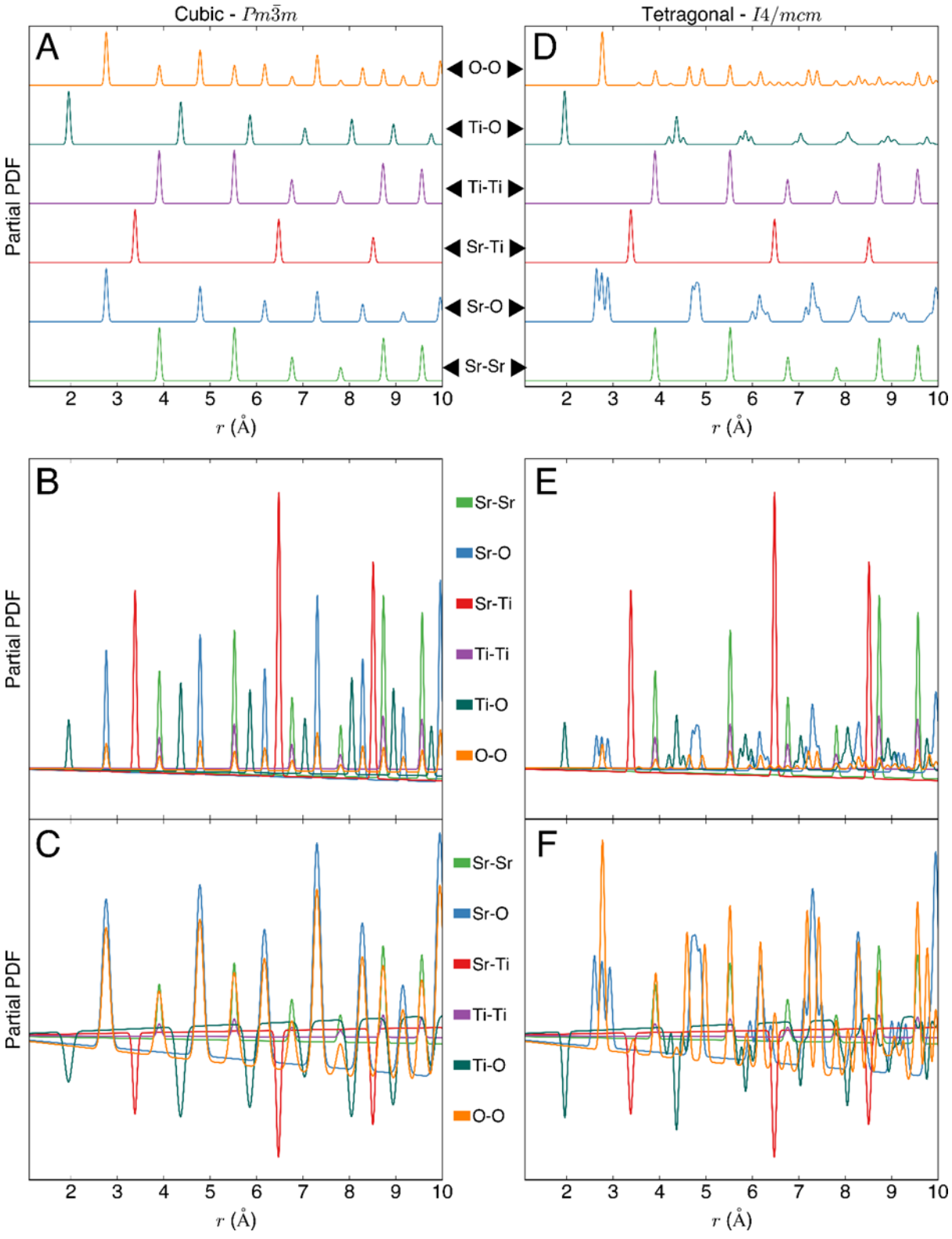

Figure 4.2: (A) Partial PDF curves for SrTiO3 calculated for the cubic phase; for the sake of visualization, each partial PDF is offset, normalized to the same amplitude, and divided by r. (B-C) Superposed partial PDFs with their real amplitudes in the case of X-rays (panel B) and neutrons (panel C); the actual G(r) baselines ($-4\pi\rho_0 r$) were kept. (D-F) The equivalent plots in the case of the tetragonal I4/mcm phase, with an applied tilt angle of 5°.

In addition, it can be helpful to compare structural observations with insights from Raman spectroscopy; since relaxor ferroelectrics such as $SrTiO_3$ and $KTaO_3$, both in the undoped and in the doped state, have been the subject of myriad studies, their dynamics are well understood and serve as reference for the current analysis. Raman scattering in perovskite ferroelectrics originates from the modulation of the oxygen electronic polarizability by optical vibrational modes (Vugmeister et al., 1995): the observation of some of these Raman modes of Pr-doped samples can be related to fluctuations of the space- and time-dependent polarization in the crystal lattice; the dependence of mode intensity and linewidth on composition gives a qualitative, yet useful, picture of how off-centered impurities in the $SrTiO_3$ lattice induce the dipolar state inferred from dielectric permittivity measurements.

Though it remains hard to reconstruct a definitive distorted unit cell even after the most likely distortions active in SPTO have been identified, it is showed that the combination of different datasets and methods is a powerful approach to model disorder in a perovskite with mixed site occupation, even more so when disorder involves small atomic displacements of both cations and oxygen atoms.

4.2 X-ray PDF and Raman spectroscopy

4.2.1 Experimental

X-ray PDF (XPDF) data were collected on selected powder samples of SPTO prepared by solid-state synthesis as described in Section 3.2. The Pr concentrations of the samples probed by XPDF were x=0, 0.020, 0.050, 0.075, 0.100, 0.125, 0.150. Synchrotron X-ray powder diffraction measurements were carried out at the ID22 beamline of the ESRF (described in 3.1.1). The data used in this PDF analysis were collected at T=90 K and T=295 K using incident X-ray wavelength λ=0.16102 Å (Q_{max}=28 Å^{-1}) on a 2D detector (Perkin Elmer XRD 1611CP3) with 100×100 μm^2 pixel size. Wavelength, sample-detector distance (379.3 mm), and azimuthal integration parameters were all calibrated with a CeO_2 reference sample that was sintered for 4 hours at 1400 °C. The detector mask was created with the program FIT2D (Hammersley, 1998); calibration and azimuthal integration were all done using the program pyFAI (Ashiotis et al., 2015). The integrated Q-space data were corrected for background, absorption, and Compton scattering and then Fourier-transformed to $G(r)$ using the program PDFgetX2 (Qiu et al., 2004). $G(r)$ is invoked according to the formalism explained in Chapter 2 and based on the definition by Keen (Keen, 2001). Local structural models were created and refined against the experimental $G(r)$ using the program PDFGui (Farrow et al., 2007). The degrees of freedom of the models (cell parameters, atomic positions, thermal displacement parameters, correlated displacement factor, and overall scale) and instrumental parameters (damping and broadening of the PDF) are optimized in least-squares refinement against the

$G(r)$ and the agreement is assessed by the fit residual (R_p), defined as:

$$R_p = \left[\frac{\sum w_i (G_i^{exp} - G_i^{calc})^2}{\sum w_i (G_i^{exp})^2}\right]^{\frac{1}{2}}$$

where G_i^{exp} and G_i^{calc} are the i-th point of the experimental $G(r)$ and of the calculated $G(r)$, respectively, and w_i is the weight of each point G_i^{exp} (normally the uncertainty on its value).

Raman measurements were performed on a Renishaw RA 100 Raman analyser at the Swiss–Norwegian Beam Lines (SNBL) at ESRF. Spectra were collected at T = 295 K on the samples with x = 0, 0.020, 0.050, 0.075, 0.100, 0.125, 0.150, using a 532 nm (green) excitation wavelength at 2 mW in backscattering mode. Exposure time was 40 s for all the samples.

4.2.2 Comparing polar and centrosymmetric models

The experimental $G(r)$ curves at 90 K and 295 K of the $SrTiO_3$ and SPTO samples are reported in Figure 4.3.

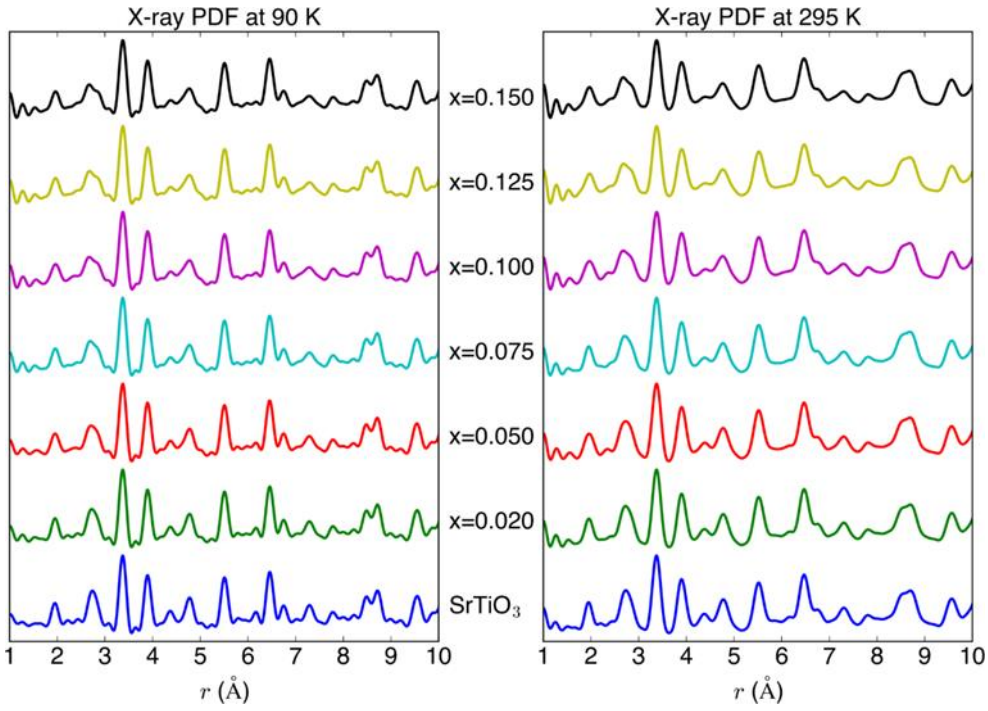

Figure 4.3: Experimental X-ray PDF curves of $SrTiO_3$ and six SPTO samples at T=90 K (left panel) and at T=295 K (right panel). All the curves are G(r) divided by r. The inset on the right shows the Ti-O peak calculated for different space groups.

The feature most sensitive to the Sr/Pr substitution is the second peak, centered at r=2.75 Å and corresponding to nearest-neighbour (NN) Pr/Sr-O distances and O-O distances; at both 90 K and 295 K, peak width increases considerably for x=0.020 and x=0.050, and for x≥0.075 two

components are clearly visible. This peak has two types of contributors: six O-O NNs belonging to the same octahedron and twelve (Pr,Sr)-O NN within the same cuboctahedron (see Figure 4.2). Because in X-ray PDF the contribution of O-O pairs is small compared with that of (Pr,Sr)-O distances (called A-O hereafter), the *x*-dependent broadening of this peak must be ascribed to changes in geometry of the AO_{12} cuboctahedra. When the local symmetry is undistorted cubic, there are 12 identical A-O distances, which give a sharp, single $G(r)$ peak (Figure 4.2, panel A blue curve); differently, a tetragonal arrangement as in the long-range structure of SPTO makes the A-O distances split into three subshells, each one comprising 4 atoms (Figure 4.2, panel B blue curve): the low-*r* and high-*r* components, involving the equatorial O atoms in TiO_6 octahedra, stray from their initial position to an extent proportional to tilt angle; the mid-*r* component, which corresponds to the in-plane A-O distances, should be affected only by displacements of the A atom, or by disordered positions of the axial octahedral oxygens. While in the $G(r)$ of undoped $SrTiO_3$ at 90 K the A-O peak is symmetric and fully consistent with a 4+4+4 splitting, the asymmetric peak visible in every doped sample – most clearly for x=0.150 at 90 K – should contain information about a different distortion.

To test the possibility that the peak asymmetry is related to polar displacements of A-site cations, simple polar distortions were applied to the cubic structure, i.e. those directly obtained from *Pm*-3*m* by switching on a single Γ4- displacement mode, to fit the $G(r)$ in the short-range. The space groups tested are *P*4*mm*, *Amm*2, and *R*-3*m*, respectively, generated by atomic displacements along the directions <100>, <110>, and <111> of the cubic phase. In addition, because off-centering at the A-site must also affect the A-Ti peak at r=3.20 Å and the A-A peak at r=3.80 Å (assuming no correlation between displacements), these fits straddle the range 2.3 Å < r < 4.2 Å. All *P*4*mm*, *Amm*2, and *R*-3*m* models fit these three peaks accurately, as shown in Figure 4.4 (panels A-C) for the fit for x=0.150 at 90 K. In each case, the broad distribution of A-O distances could be reproduced properly – and kept consistent with the relatively narrow A-Ti and A-A peaks – only by appyling equivalent displacements of both A and Ti. By contrast, all three polar models fail to reproduce the $G(r)$ if the fit is extended to the range 1 Å < r < 7 Å (Figure 4.4, panels D-F): in particular, none of *P*4*mm* and *R*-3*m* is able to fit the sharp Ti-O peak at r=1.95 Å, while *Amm*2 gives a poor fit mostly in the range 5<r<7 Å.

It must be noted that the first $G(r)$ peak, corresponding to NN Ti-O distances, shows a modest broadening with increasing x, and overall remains a single, symmetric peak. This suggests two things: first, TiO_6 octahedra remain relatively rigid and, second, the displacement of Ti inside the octahedron does not play a major role, if at all, in the *x*-dependent increase in the Ti ADP observed in Rietveld refinements (see the refined phases in Chapter 3). The inset in Figure 4.3 depicts the expected shape of the Ti-O $G(r)$ peak under the centrosymmetric and non-centrosymmetric models considered here. It is immediately clear how the Ti displacement triggered in the polar models *P*4*mm*, *Amm*2, and *R*-3*m* spreads the distribution of Ti-O

distances, while the rigid octahedral tilt in *I*4/*mcm* has no effect on it.

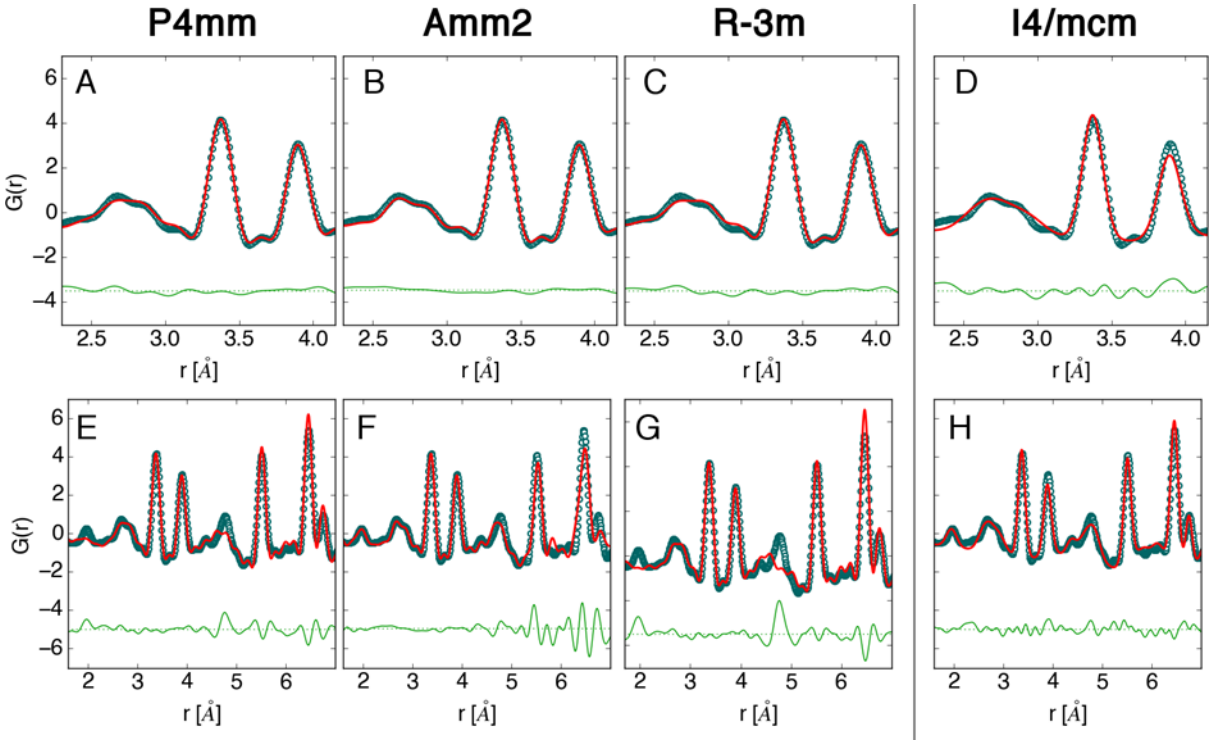

Figure 4.4: For x=0.150 at T=90 K, (panels A-D) G(r) fits in the range 2.3<r<4.2 Å for three polar models and for the AFD tetragonal model. (panels E-H) The correspondiing G(r) fits in the range 1<r<7 Å.

On the other hand, $G(r)$ fits in the range $1 \leq r \leq 7$ Å indicate that a tetragonal *I*4/*mcm* symmetry, obtained by condensing one R4+ tilt mode, is the single-distortion model most consistent with the experimental $G(r)$ of every sample at both T=90 K and T=295 K (panels D and H in Figure 4.4). Not only *I*4/*mcm* accounts for a symmetric Ti-O peak and gives a low, r-independent fit residual, but it also has the lowest number of parameters among the models tested (8 parameters; namely, two cell parameters, three thermal displacement parameters, one atomic position, overall scale, and a quadratic correlation coefficient). To this point, it must be noted that other sensible models might be those generated by the superposition of Γ- and R-point instabilities in *Pm*-3*m*, i.e. *I*4*cm*, *Ima*2, or *Cm*. These models, however, increase considerably the number of refinable parameters (they have 5, 5, and 9 atomic degrees of freedom, respectively) but fail to improve fit quality with respect to *I*4/*mcm*. Similarly, overparametrisation of the least-squares fit prevents one from testing models generated by superposition of different tilt patterns, with the added difficulty that the distortion is only related to oxygen atoms, so it contributes very weakly to the overall XPDF.

4.2.3 Local order parameters from PDF

Having shown that the tetragonal *I*4/*mcm* phase is the most sensible model among those tested for the XPDF, we apply it to all compositions at both 90 K and 295 K and discuss the evolution of the tetragonal phase with both temperature and composition in terms of the local order parameters: local tilt angle, ϕ_{loc}, and local tetragonality, η_{loc}. Figure 4.5 shows all the $G(r)$ fits up to 10 Å, also reporting the respective residual curves under each fitted curve.

The fits of the $SrTiO_3$ and SPTO $G(r)$ at 90 K return values of ϕ_{loc} systematically larger than the respective values obtained by Rietveld refinement using the same *I*4/*mcm* structure (panels A and B in Figure 4.6). The gap between the long-range and the local tilt angles widens with Pr concentration, with ϕ_{loc} exceeding 8° in the case of x=0.150. While local octahedral tilt can be expected in both $SrTiO_3$ and SPTO at T=90 K since every sample has a tetragonal long-range structure, less expectedly, the fits at 295 K return non-zero values of ϕ_{loc} for every doped sample, regardless of the cubic long-range structure in the samples with $0.020 \leq x \leq 0.075$. In analogy with the fits of the 90 K $G(r)$, samples with a long-range tetragonal structure at 295 K ($x \geq 0.100$) also show enhanced octahedral tilt on the local scale. Most important, the amplitude of local octahedral tilt does not change between 90 K and 295 K except for undoped $SrTiO_3$, whose local structure can be unambiguously interpreted as cubic; this suggests that locally the R4+ instability is active regardless of whether the mode is condensed on the long-range.

Local tetragonality follows a similar trend (panels C and D in Figure 4.6). The order parameter of local tetragonality is calculated from the tetragonal cell parameters as $\eta_{loc}=c/a-1$, where both c and a are reduced to the parent *Pm*-3*m* unit cell. Although the values of η_{loc} show a marked step after x=0.075, the overall increase in long-range tetragonality with x mirrors the trend of long-range tilt angle. Similarly to what already observed for ϕ_{loc}, the values of η_{loc} at T=90 K and T=295 K are very close, suggesting that also the strain mode coupled to the R4+ tilt mode, on the local scale, is independent of the long-range phase transition.

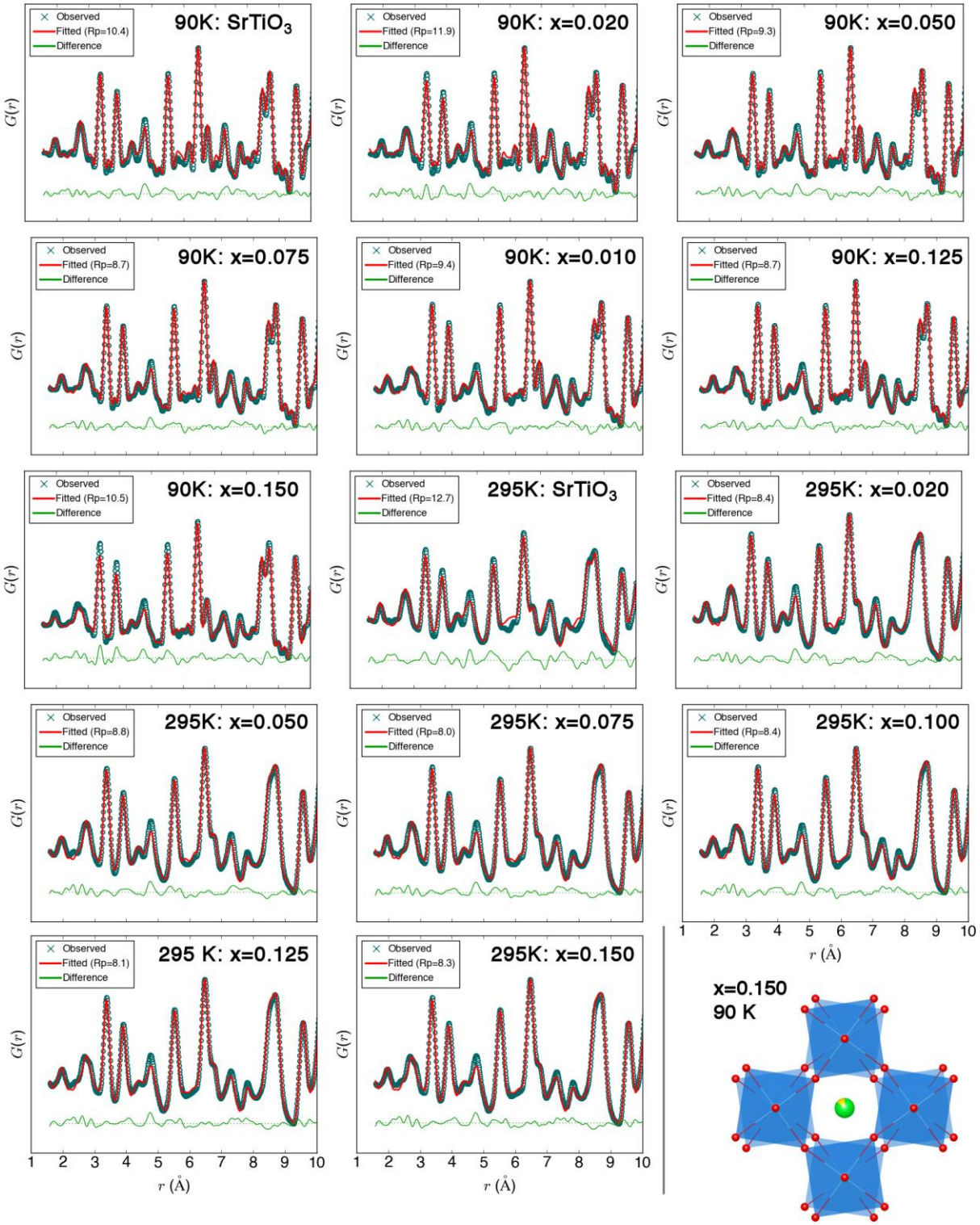

Figure 4.5: Fits to the X-ray $G(r)$ of all composition probed at both 90 K and 295K. All fits tested the symmetry I4/mcm (note that the fit for undoped $SrTiO_3$ at 295 K is far from ideal). The bottom right inset shows the view along the c-axis of the portion of the tetragonal unit cell corresponding to the parent cubic perovskite cell.

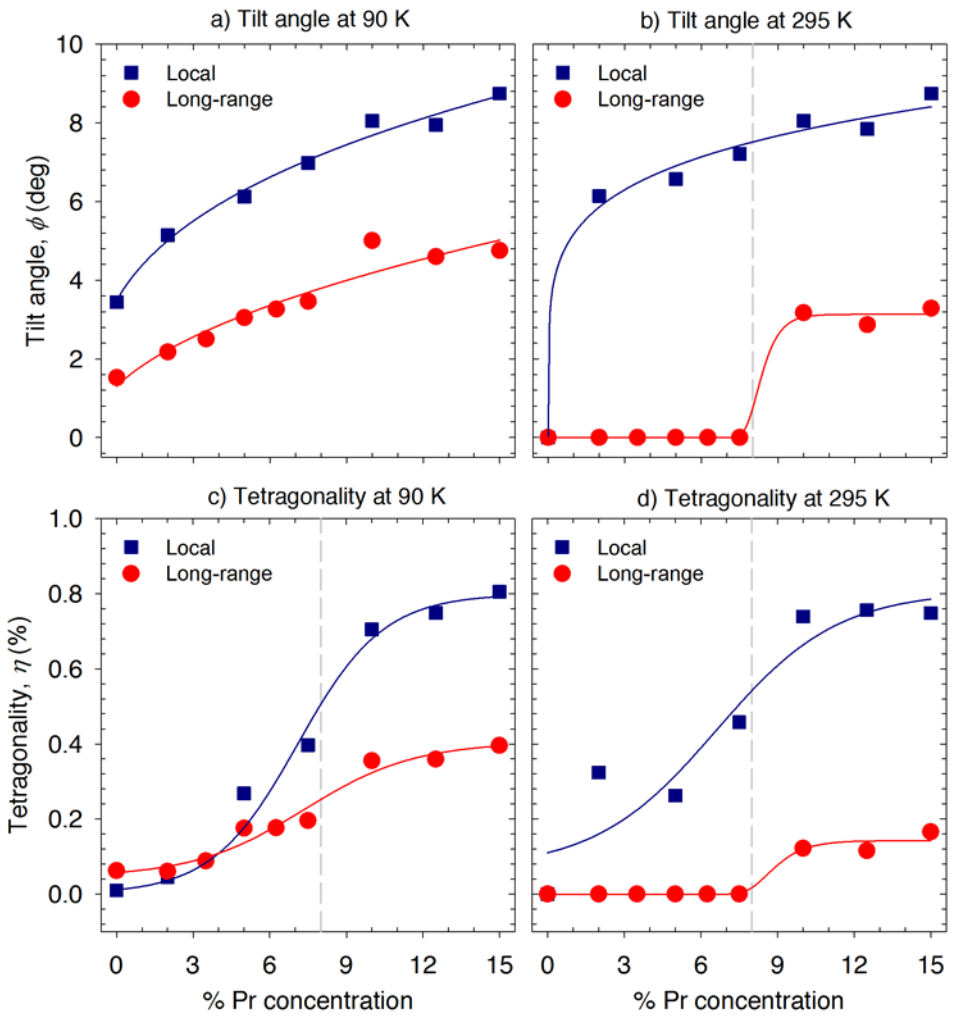

Figure 4.6: Panels A and B: values of local octahedral tilt angle (φ_{loc}) at T=90 K and T=295 K. Panels C and D: values of local tetragonality (η_{loc}) at the same temperatures. In all panels red circles are the long-range values, obtained from Rietveld refinements; blue squares are local values, obtained from phase fitting the G(r). The dashed grey line in panels B and D is the boundary of the tetragonal region in the long-range structure. The same line in panel C indicates the step in the value of (η_{loc}).

4.2.4 Local order parameters from Raman spectroscopy

To gain a better understanding of the instabilities at play in the local structure, Raman spectra of selected samples were measured at T=295 K. The spectrum of $SrTiO_3$ (Figure 4.7) consists mainly of two second-order broad bands centered at about 300 cm^{-1} and 700 cm^{-1}.

Both bands originate from the overlap of different combination modes allowed by the cubic symmetry (Bianchi et al., 1994). As Pr enters the solid solution, the breakdown of the cubic symmetry selection rules gives rise to distinct first-order modes that gradually appear in the spectra of doped samples.

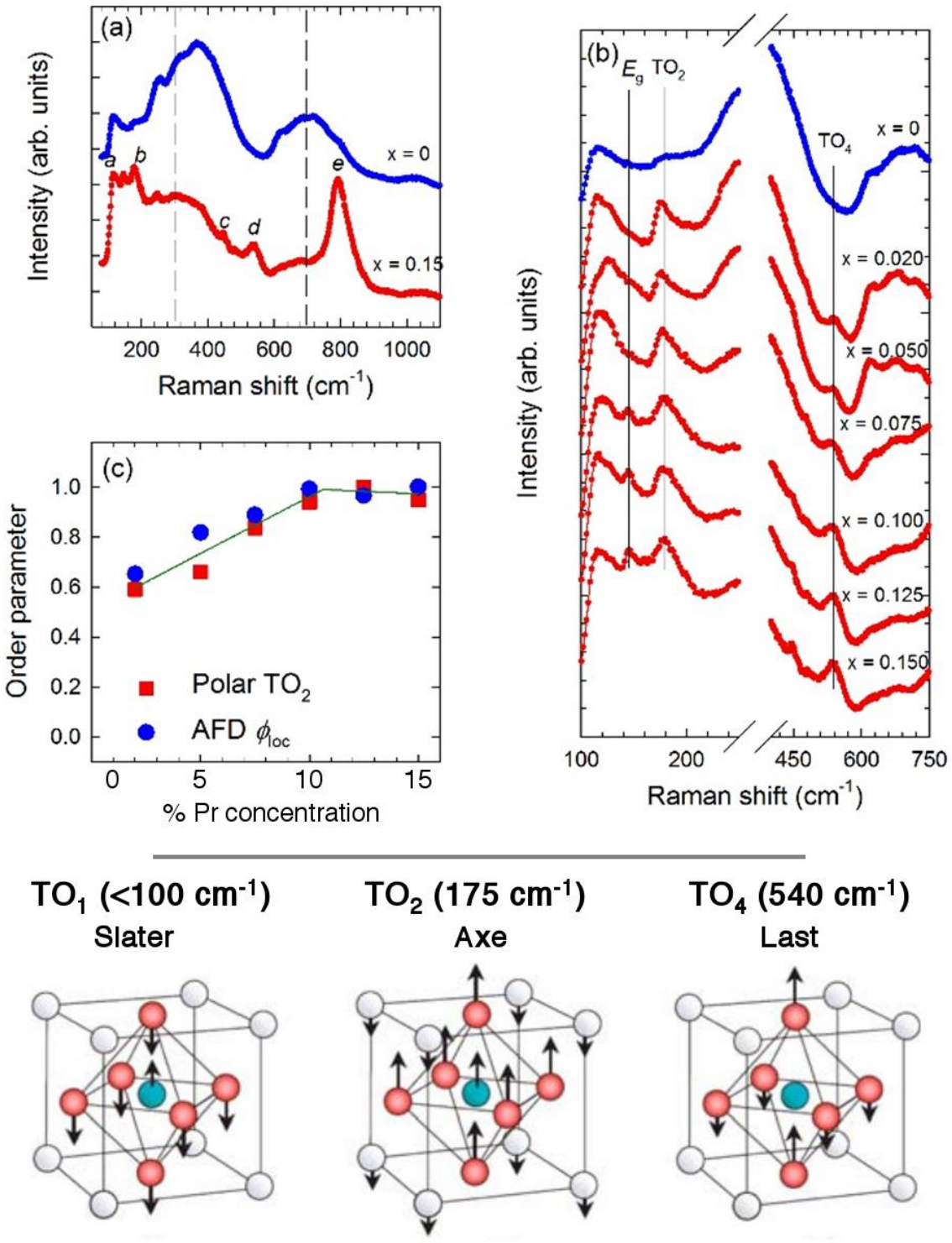

Figure 4.7: (A) 295 K Raman spectra of undoped $SrTiO_3$ and of the x=0.150 sample. The modes identified and considered in the discussion are labelled in alphabetical order in the x=0.150 spectrum. (B) Selected regions of the Raman spectra at room temperature for x=0, 0.020, 0.050, 0.075, 0.100, 0.125, 0.150. Vertical dashed lines mark the principal identified Eg, TO_2, TO_4 modes. (C) Doping dependence of the normalized ϕ_{loc} obtained from XPDF (red squares) compared with the normalized intensity of the TO_2 Raman mode (blue circles). The bottom panel shows schematically the motions related to the transverse optical modes allowed in $SrTiO_3$ (from Goian et al., 2009).

The main first-order modes are labelled in accordance with previous works (Ranjan et al., 2007; Bianchi et al., 1994), as shown in Figure 4.7 (panel A) for x=0.150: (a) 145 cm^{-1}, (b) 175 cm^{-1}, (c) 445 cm^{-1}, (d) 540 cm^{-1}, and (e) 795 cm^{-1}. The two peaks at 145 cm^{-1} and at 445 cm^{-1} arise from the structural modes E_g and B_{1g}, whereas the bands at 175 cm^{-1}, at 540 cm^{-1}, and at 795 cm^{-1} were attributed to the optical TO_2, TO_4 and LO_4 modes, respectively. As a further confirmation of the antiferrodistortive phase determined in Chapter 3, note that the absence of the TO_3 mode excludes a structural ferroelectric state in any of these samples (Toulouse et al., 1992). In the following, the focus is on the compositional dependence of the first-order Raman modes, namely, the structural E_g, B_{1g} and the polar TO_2 and TO_4 based on the spectra reported in Figure 4.7 (panel B).

Both the E_g and B_{1g} structural modes are clearly visible for $x \geq 0.100$, and also appear in x=0.075 as weak modulations at 145 cm^{-1} and 445 cm^{-1}. These two modes (labelled with *a* and *c* in Figure 4.7, panel A) correspond to the freezing of the triply degenerate soft phonon at the R point of the Brillouin zone, so they are expected to mirror the cubic-tetragonal phase transition of $SrTiO_3$ and SPTO. Coherently, they are found only in the samples that at 295 K are tetragonal or, like x=0.075, close to the phase transition. Turning our attention to the TO_2, TO_4 polar modes, it must be remembered that three types of zone-centre modes are allowed in the *Pm*-3*m* cubic structure: the Last mode, the Slater mode, and the Axe mode (sketched in the inset of Figure 4.7). While the frequency of the Slater mode (TO_1) is out of the reach of the spectrometer used, the mode labelled as TO_2 is the Last mode, which represents the counter-oscillation of A cations and BO_6 octahedra; the higher-frequency TO_4 is the Axe mode, corresponding to the stretching of the BO_6 octahedra toward one of the axial oxygen atoms (Bianchi et al., 1994, Goian et al., 2009).

As can be seen from the spectra in Figure 4.7 (panel B), every sample except undoped $SrTiO_3$ features the bands relative to the TO_2 and TO_4 polar modes; this indicates that the zone-center polar instabilities are switched on already at the lowest Pr concentration. The intensity and the asymmetry of the TO_2 line, both increasing with Pr concentration, can be interpreted, respectively, as the measure of the mean-square polarization in the lattice and its inhomogeneous, fluctuating distribution (Toulouse et al., 1992; DiAntonio et al., 1993). In addition, the shape of the TO_2 line is qualitatively consistent with a polar mode coherence length substantially shorter than the theoretical critical coherence length related to a structural FE transition. All these results suggest that Pr could be involved in the emergence of local polar phenomena.

When randomly-substituted ions are off-centered in their sites in a highly polarizable lattice, they form dynamic, randomly-relaxing dipoles that produce a domain state with space- and time-varying polarizability; in absence of a long-range FE transitions. this behaviour, together

with the emergence of the TO_2 and TO_4 polar modes, was observed in known relaxor ferroelectrics like Li- and Nb-doped $KTaO_3$ and Ca-doped $SrTiO_3$ and linked to the relaxational frequencies of polar nanoregions (Toulouse et al., 1992; DiAntonio et al., 1993; Bianchi et al., 1995; Toulouse et al., 1994; Vugmeister et al., 1995). In our case, the mode frequencies vary only weakly with composition, but the intensity trends are quite revealing. In particular, the TO_2 intensity increases smoothly with x and then levels off when $x \geq 0.100$ (Figure 4.7 panel C). Most important, if the polar TO_2 intensity and the AFD ϕ_{loc} extracted from XPDF fits are normalized to unity and plotted together, it is immediately clear that the two parameters have the same dependence on composition (Figure 4.7 panel C).

How to interpret this? The TO_2 intensity can be seen as a gauge of the polar distortion associated with polar nanoregions, and the local tilt angle (ϕ_{loc}) as its structural equivalent. In the model proposed by Toulouse and co-workers for doped $KTaO_3$ (DiAntonio et al., 1993; Toulouse et al., 1994; Vugmeister et al., 1995), assuming a slow relaxation of the impurity-induced dipoles, the intensity of TO_2 is a measure of the autocorrelation ($<P^2>$) of the spatially- and temporally fluctuating polarization (Bianchi et al., 1995; Toulouse et al., 1994). Similarly, the PDF represents the autocorrelation function of the real space, depending on the fluctuations from the average electron density given by local structural disorder, which is largely enhanced by doping. Thus, the correlation between a purely FE order parameter and a purely AFD order parameter implies that local structural deviations quantified by the local AFD increase can actually originate from fluctuations in local polarization, signalled by the emergence of the TO_2, TO_4 Raman modes.

4.2.5 Discussion

As shown in Chapter 3, SPTO retains inversion symmetry through the cubic/tetragonal transition, accompanied by an increasing AFD character in the long-range phase. This agrees very well with the first-principles calculations by Zhong and Vanderbilt, predicting that a strong AFD distortion practically suppresses FE distortions (Zhong and Vanderbilt, 1995). Moreover, within the accuracy of the XPDF study, a centrosymmetric, AFD phase is the model most consistent with the local structure of every Pr-doped sample both at T=90 K and T=300 K. In few cases, this holds true even when samples are cubic on the long-range.

The absence of a polar structural order seems to conflict with the observation of dielectric permittivity peaks by Duran et al. (Duran et al., 2005) and of the polar Raman modes discussed in section 4.2.3. But the coexistence of these conflicting phenomena can be reconciled with theory by considering the combined effect of tetragonality and tilting angle, which largely characterizes the structure of SPTO both locally and long-range, and which Aschauer and Spaldin recently studied by DFT (Aschauer and Spaldin, 2014). In particular, they found a theoretical equilibrium tilt angle (ϕ_{eq}=5.7°) below which the suppression of the FE

displacement of Ti by octahedral rotations is energetically favourable: because of charge transfer between Ti-O σ^* and Sr-O σ^* bonds, which decreases the anti-bonding orbital overlap, the Ti-O bonds are stronger and, consequently, less polarizable. This is an unfavourable condition for ferroelectricity. But if octahedra are tilted by an angle larger than ϕ_{eq}, the increased tetragonality coupled to octahedral tilt in the AFD model makes the FE displacement energetically favourable again: in order to offset the loss of Ti-O π-bonding along the *c*-axis caused by large tilting, the FE displacement of Ti is allowed to rise at a favourable energy cost, as shown by the blue curve in Figure 4.8 (taken from Aschauer and Spaldin, 2014).

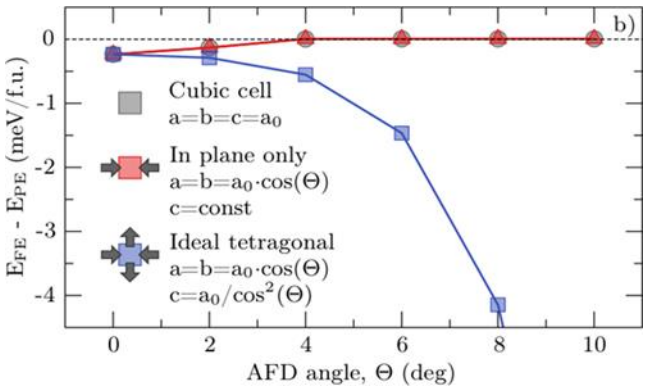

Figure 4.8: Taken from Aschauer and Spaldin, 2014. Plot of the energy difference between the AFD and the FE instabilities considered by Aschauer and Spaldin (octahedral rotation and one-dimensional displacement of Ti) as a function of octahedral tilt angle. It is immediately clear that octahedral rotations must be large and coupled with tetragonal strain of the same kind shown by $SrTiO_3$ and SPTO in order for the FE displacement mode to become energetically favourable (blue curve). Conversely, no-strain or in-plane-only strain prevent stabilization of the FE mode.

Our experimental results match this scenario. First, the two local order parameters ϕ_{loc} and η_{loc} are coupled, as they show very similar trends with composition at both temperatures. All values of ϕ_{loc} are greater than the critical ϕ_{eq} in the whole range of composition (panels A and B in Figure 4.6) and local tetragonality always increases with respect to long-range (panels C and D in Figure 4.6). Second, the presence of zone-centre modes is demonstrated locally by the appearance of the TO_2 and TO_4 Raman peaks already at the minimum Pr concentration; the correlation between the TO_2 intensity and the local octahedral tilt angle at T=295 K supports the coexistence of FE and AFD instabilities in SPTO. The short correlation length of the polar nanoregions evidenced by Raman - and implied by the local scale of the PDF - means that they are also compatible with a centrosymmetric long-range structure.

Despite the good agreement between the results of independent probes, this picture needs confirmation. In the following section direct evidence is sought of the coexistence of tilting

and polar distortions by taking advantage of the higher sensitivity of neutron PDF to the scattering by oxygen atoms. In fact, the main contributor to the refined value of tilt angle is the broad A-O peak centered at r=2.75 Å; the weight of successive A-O and O-O peaks in the total $G(r)$ is low and their intensities are considerably more smeared by applying octahedral rotations (Figure 4.2). As anticipated by the asymmetry of the first A-O peak, it is not unreasonable that the local tilt angle actually encompasses different local phenomena, affecting the same A-O and O-O distances, to which these $G(r)$ curves are not very sensitive. Although a large octahedral tilt reproduces decently the broad distribution around r=2.75 Å, this simple tetragonal model may not be the ultimate description of the SPTO local structure.

Ultimately, XPDF shows that macroscopic cation displacements do not play a large part in reducing the local symmetry of SPTO at any T or x, as a centrosymmetric model is still reasonably consistent with the $G(r)$. On the other hand, XPDF tells relatively little about the disorder affecting the oxygen sublattice. In the following, neutron diffraction is used in order to break down the large, all-encompassing octahedral tilt into different contributions, seeking direct evidence of the cooperation between zone-center and zone-boundary distortions.

4.3 Neutron PDF

4.3.1 Experimental

Neutron powder diffraction measurements were carried out at the GEM diffractometer at the ISIS spallation source (Hannon, 2005) on 8 g aliquots of the SPTO samples with x=0.035, 0.075, 0.150, and $SrTiO_3$ (x=0). Each sample was contained in a cylindrical vanadium can (7.6 mm inner diameter, 0.2 mm wall thickness, 50 mm height) and measured for 6 h at 90 K temperature. The scattering of instrument background, empty vanadium can, and V/Nb (95%/5%) rod was also measured and used for data correction. Size of the incident beam was 15×40 mm (width×height); the range of neutron wavelength used was $0.15\ \text{Å} \leq \lambda \leq 3.0\ \text{Å}$. Data from seven detector banks were corrected, merged and Fourier-transformed to obtain the pair distribution function (PDF) using the GudrunN program (Soper, 2012). The neutron PDF (NPDF), here expressed by the $g(r)$ function as defined by Keen (Keen, 2001), was obtained using a range of Q between 0.7 and 40.0 Å^{-1}. PDF analysis is first carried out by the model-fitting method implemented by the program PDFGui (Farrow et al., 2007); a briefing on the method is found in section 4.2.1. Reverse Monte-Carlo refinements are carried out using the RMCProfile code (Tucker et al., 2007) following the method described in section 4.3.2; analysis of the solutions makes use of the Python program outlined in section 4.3.3. Peak fitting was done using the program Fityk (Wojdyr, 2010).

4.3.2 Reverse Monte Carlo refinements

The Reverse Monte-Carlo method to fit total scattering data, here incarnated by the RMCProfile code (Tucker et al., 2007), was used to generate symmetry-unbiased, atomistic configurations based on the fit to the total scattering functions. Differently from the previous section, here the aim is to keep the PDF analysis as independent as possible of models related to the symmetry reduction from cubic and, thus, to show how RMC refinements can supply a plausible picture of the distortions in SPTO using only composition and bond-distance windows as constraints.

The type of PDF function used in the fits is $g(r)$ (defined in Chapter 2). $g(r)$ is not scaled by r, unlike the $G(r)$ function used for XPDF analysis, so that the low-r part has the highest weight. In the following section, this choice is justified by carrying out PDF fits over different ranges in real space and tracking the departure from the simple $I4/mcm$ model determined in the previous section. The fit range of the $g(r)$ is up to 16 Å, as defined by the longest vector in the supercell of choice, which is a 6×6×4 supercell of the tetragonal $I4/mcm$ unit cell (a=b=33 Å, c=31 Å). As usual, Ti is placed in the lattice origin and all initial atomic positions are set to the undistorted cubic symmetry (i.e. no initial tilt angle was assumed).

Because of the relatively low Pr concentration in the SPTO samples, the neutron scattering cross-sections of the atom pairs involving Pr are lower than any other atom-pair cross-section. Still, Pr gives a reasonable contribution to NPDF for x=0.150 (the case of x=0.150 is shown in Figure 4.2) and in this case, therefore, it was possible to account explicitly for Pr as a separate atom; this permits to readily distinguish the refined positions of Pr atoms from those of Sr atoms, and to simulate the distribution of Pr atoms in the supercell by using the atom swap function in RMCProfile (Hui et al., 2007). When distinct Sr and Pr sites are not applicable, instead, the RMC simulations use a 'grey' atom obtained as the sum of the scattering lengths of Sr and Pr weighted by the respective molar fractions. All the neutron scattering lengths relevant to this work are listed in the tables in the Appendix to this chapter.

Distance windows (DW) define the lower and upper limits for all nearest-neighbour (NN) interatomic distances in the supercell and are specified in the RMC input file. Narrow DWs are used in the early stages of the refinement in order to preserve the expected polyhedral connections; the window limits are then relaxed, for instance, set to slightly exceed the visible limits of the PDF peak, so that minimization of the $g(r)$ fit outweighs the initial guess for the rest of the refinement. Table 4.1 lists all the DW constraints used in this analysis.

Table 4.1: Minimum and maximum distance value allowed for the nearest-neighbour pairs in $SrTiO_3$ and SPTO. One single, average atom at the A site is assumed.

	A-A		A-Ti		A-O		Ti-Ti		Ti-O		O-O	
$SrTiO_3$	3.73	4.13	3.18	3.60	2.53	3.07	3.73	4.13	1.80	2.16	2.53	3.07
x=0.035	3.73	4.12	3.18	3.60	2.51	3.10	3.73	4.12	1.79	2.16	2.51	3.10
x=0.075	3.72	4.12	3.18	3.60	2.42	3.18	3.72	4.12	1.78	2.16	2.42	3.18
x=0.150	3.71	4.12	3.18	3.60	2.40	3.18	3.72	4.12	1.78	2.16	2.40	3.18

The choice of not setting hard constraints to the atom moves also led us to exclude the fit of reciprocal-space data after a few initial attempts. The agreement of the final configuration with reciprocal-space data is evaluated a posteriori by running zero refinement cycles while reading all the $g(r)$, $F(Q)$, and Bragg datasets. The maximum move applied to an atom is set to 0.05 Å for every element. Though the average move is smaller than this, setting a lower limit can be useful in the case of atoms forming pairs that contribute weakly to the overall scattering cross-section and that, consequently, are prone to very large shifts and to incorporating experimental noise.

For each of the four PDFs at 90 K analysed here 36 independent RMC simulations were run, each starting from an undistorted 6×6×4 supercell; the final configurations for each sample are then merged to obtain an 'effective' supercell consisting of 18×18×16 tetragonal unit cells. The merged supercell for each sample thus contains 576×36=20736 Sr/Pr atoms, 20736 Ti atoms,

and 1728×36=62208 O atoms.

Increasing statistics by using a large number of atoms in the analysis is critical to extracting tidy information on disorder. It must be reminded that RMCProfile has no explicit treatment of the effect of termination error, defined by Q_{max} (i.e. convolution of the PDF with a broadening function, which gives the minimum peak width at any distance) and of thermal motion (i.e. broadening dependent on which atom contributes to the peak) on the PDF. This implies that the linewidth of every peak calculated by RMCProfile is solely due to the underlying distribution of interatomic distances in the supercell. This has two main consequences on the final configurations: i) the effect of termination error due to finite Q_{max} is accommodated to by having slightly more disorder in the supercell than is expected, acting like a broadening function[1], and ii) the distribution of the atomic positions for each atom type partly contains a normal distribution of atomic positions that reproduces the PDF broadening due to thermal motion. Consequently, each of the 36 snapshots contains a different arrangement of thermally displaced atoms (it can be safely assumed that normally distributed displacements are random and not repeated identically in every independent refinement), whose contribution to the final structural model can be reduced by running multiple independent refinements (36 in this case). Whereas thermal fluctuations tend to average out to a uniform background in the merged configuration, physically meaningful atomic displacements are expected to show up consistently in all snapshots, concentrating the atoms in their best-fit positions.

4.3.3 Analysis of the RMC configurations

This paragraph explains the method used to analyse the result of the RMC refinements to NPDF. The routines described were all written in Python 2.7 using the standard libraries NumPy, SciPy, Matplotlib, and Seaborn.

The first step in the analysis of RMC configurations is reading through the list of atoms that constitutes the output of RMCProfile; at the same time, the program reads the list of atoms of an undistorted supercell with same size, so that two parallel arrays of atomic positions stored in memory containing the final and the initial atomic coordinates. Next, periodic boundary conditions are applied by appending to the existing lists of coordinates the atoms contained in the outermost subcells, with coordinates and subcell indexes shifted by one supercell unit[2]. A third array of atoms is produced for supercell visualization with VESTA or analogous

[1] Toby and Egami (1992) showed that PDF broadening due to termination error is almost negligible compared with the broadening due to thermal motion if Q_{max} is high enough. For Q_{max}=40 Å^{-1}, as in this case, this holds true for any Debye-Waller factor larger than, for instance, the zero-temperature limit of aluminium (B=0.28 Å^2). In view of the thermal parameters found previously (see Chapter 3), the effect of limited Q_{max} on our refinement solutions is expected to be extremely small.

[2] The original numbering of the subcells given by RMCProfile is maintained. If the original supercell had subcell indexes (0, 1, 2) in a given direction, the expanded supercell will have subcells (-1, 0, 1, 2, 3).

programs, whereby all atomic positions are converted from fractional coordinates to cartesian.

Loading the supercell is done in turn for every RMC configuration found for a given sample. The program runs an outer loop over all these configurations (in this case that should be 36 times) and for each of them runs the main polyhedra reconstruction routine. The latter is a loop running over all the cations of the specified type (Ti or Sr or Pr) and, for each individual atom, it runs a nested loop over all oxygen atoms, including those created by expanding the supercell boundaries. A flowchart is shown in the Appendix to this Chapter.

In the loop over the oxygen atoms, the script accepts as O atoms coordinated to the current cation only those located at a suitable bond distance from the metal atom position (*M*) and whose projections (Δx, Δy, and Δz) on the cartesian axes fall within certain limits dictated by polyhedral geometry and specified in the script. The accepted O atoms are then stored in a list and labelled according to their position relative to the atom *M*: in octahedra, for example, O1-O4 are the equatorial O atoms numbered counter-clockwise (as seen down the <001> direction) starting from the atom situated in $-\Delta x$,$-\Delta y$, Δz with respect to *M* (the sign is given by $\Delta x = x_{oxygen} - x_{cation}$ and Δz must be close to zero); O5 and O6 are the axial O atoms situated above and below the cation, respectively. Analogous numbering is used for O atoms in cuboctahedra. Once the coordinates of the metal atom ($M=(x_M,y_M,z_M)$) and of the O atoms that make up the polyhedron are known, the cation displacement (ΔP) from the centroid of the coordinated oxygens[3] [$\langle O \rangle = (\langle x \rangle, \langle y \rangle, \langle z \rangle)$, brackets denoting the average over all O atoms in the polyhedron] is simply calculated as $\Delta P = M - \langle O \rangle$. Likewise, the displacement of the sole oxygen centroid can be calculated as $\Delta O = \langle O \rangle - C$, where *C* denotes the centroid of the initial positions of the O atoms read from the array of initial positions. Since *C* is also the initial position of the cation, the absolute cation displacement can be calculated as $\Delta M = M - C$.

As mentioned in the previous section, the atomic positions in a RMC configuration have to account for the thermal broadening of the PDF by accepting 'extra' random displacements around their mean position. The exact atomic positions change between different snapshots and thus coalesce into a broad distribution. But since the aim of moving atoms in a RMC supercell is primarily to fit the features of the experimental PDF related to structural disorder, the refined atomic positions must reflect a given distortion, e.g. atom off-centering or octahedral tilt. In view of the large number of atoms used and of the broad distribution of their positions, it is not practical to visualize all the individual atoms from multiple merged configurations. Instead, if atoms are displaced consistently between different snapshots in response to a distortion signalled by the PDF, the sensible information can be found in the density of these positions. This is visualized by plotting the occurrence of atoms in two dimensions on a fixed range of

[3] The position $\langle O \rangle$ *after* the refinement is not the same as the initial cation position; the latter is, instead, the same thing as the centroid of the O atoms *before* the refinement, so they are given the same symbol (*C*).

distances from an origin of choice (e.g. the centroid of O atoms or the initial position of the atom) and grouping the occurrences in gaussian bins ('kernels') to obtain their probability density function. This work is focused on finding the position of the cations with respect to the centre of the coordination polyhedron (ΔP); thus, each density plot represents the three-dimensional density of cation positions (20736 values of ΔP) projected on the slice of a given polyhedron centered on the position of the centroid $\langle O \rangle$ of the O atoms. Plots represent real-space slices spanning from $-0.15 < r < +0.15$ Å from the centre of the plot ($\langle O \rangle$, marked with crosshairs). As sketched in Figure 4.9, the values of ΔP are projected on the plane and plotted so that the x and y directions in real-space match the x and y axes of the plot; the centroid of the anions lies in the plane and at the centre of the crosshair. To obtain the probability density function, the distribution of ΔP is binned using gaussian kernels with a bandwidth generally corresponding to the bin size of the PDF dataset[4] (0.02 Å) using the kernel density estimator function of the Seaborn Python package. The values of probability density (from 0 to 1) are colour-coded so that one end of the colour scale indicates where the displaced atoms (ΔP) are most concentrated, and the other end of the scale indicates where displaced atoms are found the least frequently.

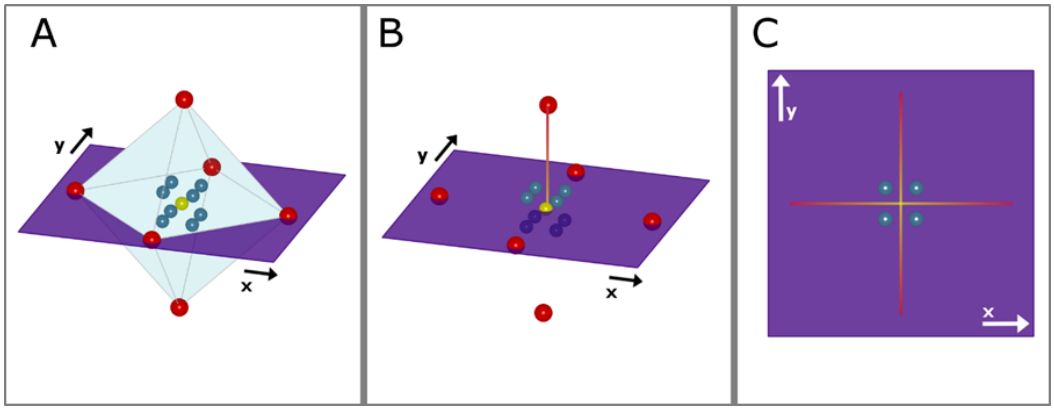

Figure 4.9: How the density plots are constructed. Panel A: the viewing plane (purple) passes through the centroid of the oxygen octahedron (the dummy atom in yellow). Blue atoms represent the 8 symmetry-equivalent positions of the maxima of probability density of the cation positions. Panel B shows the same view without the octahedron; it must be noted that the oxygen centroid is not the same as the initial cation position, since the O atoms were moved as well during the RMC refinement. Panel C: projection along the <001> direction showing the peaks of the probability density (blue points) and the centroid of the octahedron as the centre of the crosshair.

From the position and the orientation relative to the cation of each oxygen atom constituting

[4] Kernel width can also be optimized by the Python function used for kernel density estimation, but this tends to oversmooth distributions, making close peaks undistinguishable. Because all distributions of positions returned by RMCProfile are spread differently, optimum smoothing of KDE was actually obtained using a factor proportional to the standard deviation of each distribution. Anyway, to facilitate comparisons, the same bandwidth was used for all the distributions shown in section 5.3.5.

the polyhedron, the program also calculates a few geometric parameters: volume (by dividing the overall volume in tetrahedrons), tilt angle, the bond distribution index defined by Baur (Baur, 1974), and the displacement of the Axe-type octahedral distortion (see Figure 4.7). Tilt angle is calculated as the angle between the *a* or *b* axis of the supercell and the line perpendicular to the plane fitted through four points: the two axial O atoms of the octahedron and the two midpoints of the equatorial O-O bonds along the axis considered. The Baur distortion index (*D*) is simply obtained as:

$$D = \frac{1}{N}\sum_{N}\frac{|d_{obs} - \langle d\rangle|}{\langle d\rangle}$$

where d_{obs} is the experimental interatomic distance, <*d*> the average bond distance, and *N* the number of bonds considered.

4.3.4 Compatibility with local tetragonal structure

The *g*(*r*) of the four samples measured at 90 K are compared in Figure 4.10. It must be reminded that at 90 K all four samples have a tetragonal long-range structure, and that analysis of XPDF suggests a large local octahedral tilt angle, albeit varying slowly with *x*.

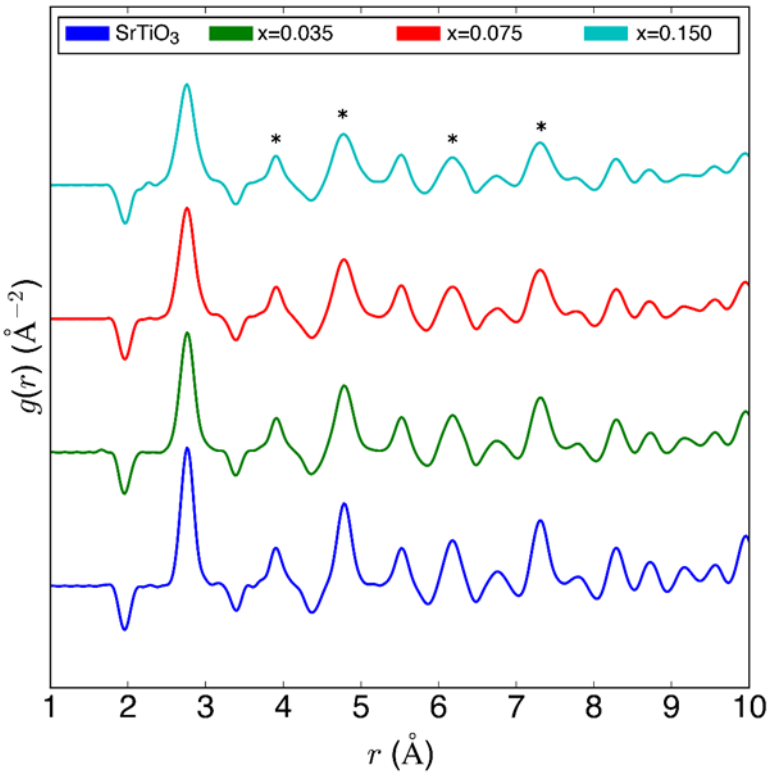

Figure 4.10: Experimental neutron g(r) curves of $SrTiO_3$ and three SPTO samples at T=90 K. Asterisks mark the oxygen-related peaks more affected by composition changes (see 4.3.3).

The effect of increasing Pr concentration of NPDF is immediately evident on the peaks at r=3.8, 4.9, 6.1, and 7.2 Å, all arising from overlapping O-O and A-O distances. With respect to XPDF, where disorder in the A-O correlations shows up mostly in the peak at r=2.75 Å, and where O-O correlations only give weak signals, in NPDF the information related to oxygen atoms is dominant (Figure 4.2). This allows reliable comparisons between the peaks related to the different chemical environments over a wide range of r. It must be noted, for instance, that the negative A-Ti peak at r=3.2 Å is practically unaffected by changes in composition; we also confirm the observation in XPDF of narrow distributions of Ti-O distances up to x=0.150; by contrast, all the peaks involving A-O and O-O pairs are broadened as x is increased (compare Figure 4.10 to Figure 4.2). While this can be partly ascribed to a larger amplitude of the $a^0a^0c^-$-type octahedral tilt generated by the AFD structure of SPTO (see Chapter 3 and paragraph 4.2 above), many of the broad $g(r)$ features arise from distances between octahedra that lie in different planes along the c-axis and are thus uncorrelated by tilt (Vanderbilt and Zhong, 1998); this might carry useful information about other kinds of distortion. Unfortunately, the systematic overlapping of A-O/O-O and of A-A/O-O distances in the perovskite structure discourages directly fitting peaks and analysing their widths. Thus, preliminary insights on the disorder in the A and O sublattices are sought, once again, by model-fitting.

$G(r)$ fits are carried out over successive ranges of r ('box-car' refinement (Coduri et al., 2013)) using the *I*4/*mcm* model with the same refinable parameters specified in the previous paragraph. The plots and the selected values shown in Figure 4.11 evidence that the good $G(r)$ fit obtained for x=0.150 in the shortest range (1-6 Å) is conditional on the use of a large correlation factor of atomic displacements (the δ_2 parameter in PDFGui); by contrast, not accounting for correlated displacements in the case of $SrTiO_3$ affects only slightly the fit quality (panels A-D). Shown in panel I, the weight of correlated motion increases gradually with the Pr concentration, as evidenced by both the x-dependence of δ_2 and the spread between the residuals (R_p) of the fits in which δ_2 is switched on and off. This result reminds of the discrepancy observed in the XPDF curves between the relatively sharp Ti-O, A-Ti peaks and the broad, bivariate A-O distribution at r=2.75 Å (see discussion in 4.2.2); particularly, a larger δ_2 parameter imposes narrower Ti-O and A-Ti peaks in order for them to be consistent with the broad features generated by disordered AO_{12} cuboctahedra. It must be also noted that the worse agreement between the *I*4/*mcm* and the experimental $G(r)$ as x is increased (the relevant fit residuals R_p are plotted in panel I of Figure 4.11). The departure from the *I*4/*mcm* model, however, seems to be dependent on r: beyond r=6 Å, the $G(r)$ fit residuals of the four samples first get closer and then converge in the 12-18 Å range (R_p values are shown in panel J and plots for x=0.150 and $SrTiO_3$ in panels E-H of Figure 4.11).

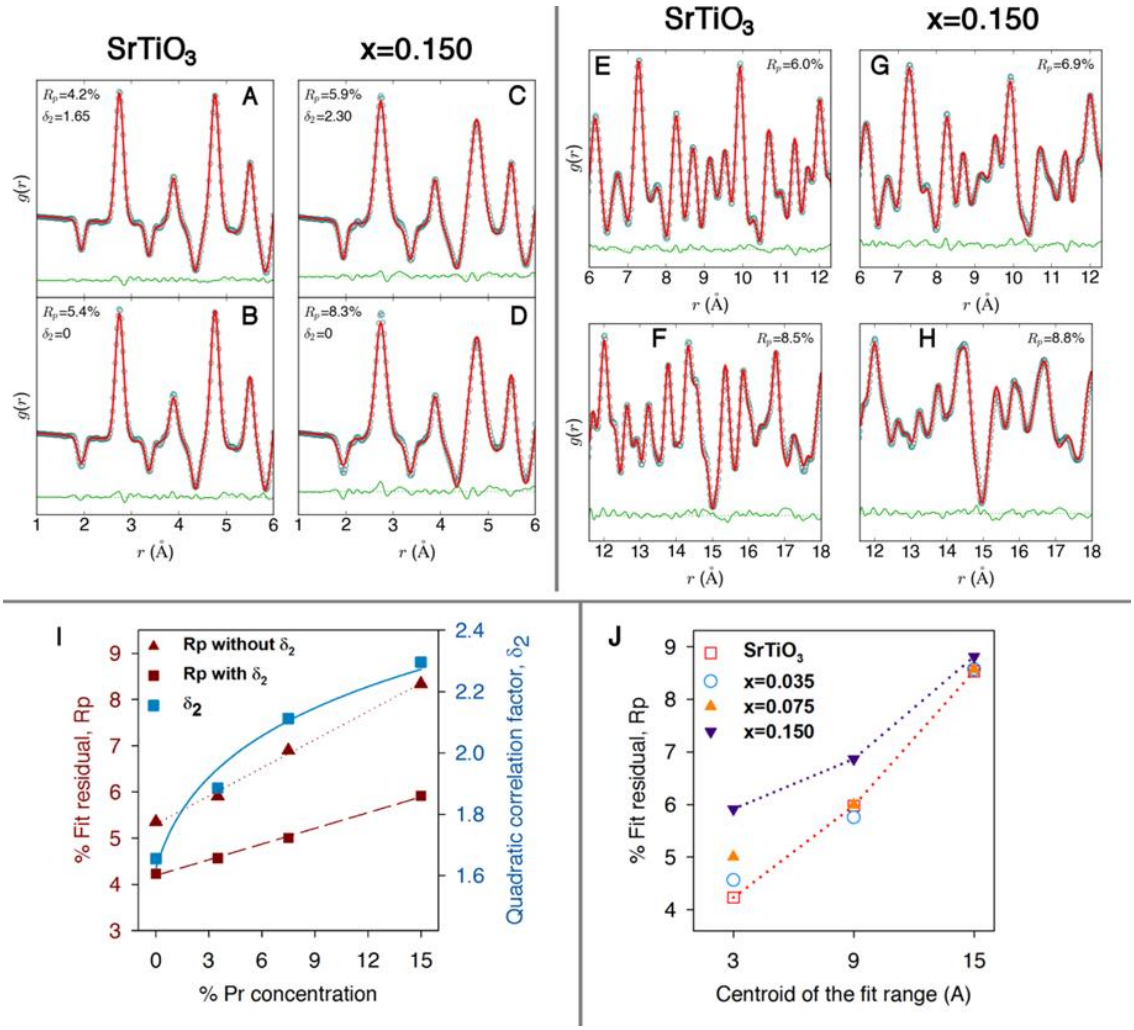

Figure 4.11: Box-car fits to the G(r) of $SrTiO_3$ and SPTO (x=0.150) using the I4/mcm model. Panels A and C show the best fits obtained by allowing the quadratic correlation factor to the atomic displacements (δ_2); the model fits the G(r) of the doped sample not as accurately as that of undoped $SrTiO_3$. Panels B and D show the corresponding fits when the correlation parameter δ_2 is set to zero; notice the increase in the residual (R_p) for x=0.150. Panels E and F show the fits for $SrTiO_3$ in the boxes 6-12 Å and 12-18 Å, respectively; panels G and H show the same fits for x=0.150. Panel I shows the increase in fit residual in the 1-6 Å range with increasing x, both when correlated atomic displacements are accounted for (red filled squares, dashed line) and when δ_2 is set to zero (filled triangles, dotted line); filled blue squares with solid line are the values of δ_2 relative to the former case. Panel J shows the convergence of the fit residuals of the four samples as the fit range is moved further in r.

All indications from PDF analysis so far point to the following picture:

i) disorder increases with Pr concentration in the doped samples, evidenced by worse fits to *G*(*r*) by the long-range *I*4/*mcm* structure in the range up to 6 Å;

ii) local distortions are substantial in the first 10 Å, then average out to the long-range structure,

as suggested by similar agreement with *I*4/*mcm* of all four samples in the range 12<*r*<18 Å;

iii) disorder affects mostly the coordination environment of the mixed-occupancy A-site; this appears as a large octahedral tilt in the local *I*4/*mcm* model best fitting the XPDF or, more generally, as the larger width of the peaks containing A-O and O-O distances.

RMC modelling of neutron PDF is meant to expand on this picture by providing a detailed atomistic configuration for each of the four samples. The distribution of the positions of each atom type are evaluated with respect to the unperturbed initial position and with respect to the centroid of the coordination polyhedron. Polyhedral geometry is also evaluated as described in the previous section. In view of the larger influence of disorder on the short-range (*r*<10 Å) inferred from box-car refinements of the *G*(*r*), all the RMC refinements of the NPDF are carried out on the *g*(*r*), in which the interatomic distances within the first few Ångstroms have the largest weight.

4.3.5 Results of RMC refinements

Once all the RMC refinements are run, and provide the respective configurations, the next step is extracting structural information. The program used to analyse the RMC configurations is outlined in section 4.3.3. First, we look at octahedral tilt angle, which showed the largest effect on the XPDF curves. Contrary to what observed in the previous section, the average octahedral tilt angles obtained by fitting the 90 K neutron data fall in the range 1.5° < ϕ < 5.5°. As shown by Figure 4.12, this is in very good agreement with the tilt angle obtained by reciprocal-space analysis of the same neutron diffraction data. It must be reminded that the tilt angle in the case of RMC refinements is calculated for each of the 20736 octahedra available, yielding a distribution of values rather than a single refined value as in model-fitting; the values plotted in Figure 4.12 are therefore the mean values of each distribution.

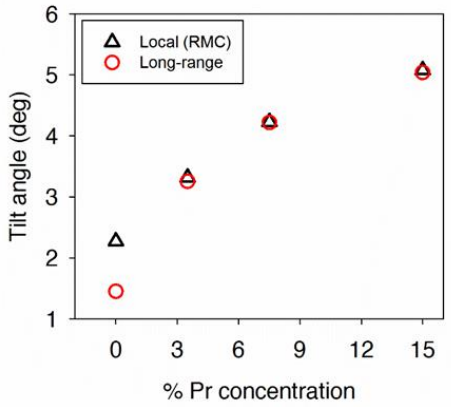

Figure 4.12: Octahedral tilt angle obtained by reciprocal-space analysis (red circles) compared to the mean of the distribution of tilt angles obtained by RMC refinements of neutron PDF (black triangles). The bars on the RMC points are the limits of the tilt-angle distributions.

It must be pointed out that octahedral tilt angle is calculated here as the rotation, with respect to the *a* and *b* axes, of the plane passing through i) the axial oxygen atoms and ii) the midpoints of the two pairs of equatorial atoms; the tilt angle thus calculated is independent of most possible distortions of the octahedron, so it should be reasonably close to the value obtained if the $a^0a^0c^-$-type tilt were isolated as the only active distortion[5]. While octahedral tilt can be investigated in depth by the RMC method, the other order parameter of the AFD structure, tetragonality, is practically suppressed by the fact that the lattice parameters in the RMC simulations are fixed. Another contraindication to searching for elongated subcells is that the atom moves are generated with equal probability along any of the three orthogonal directions.

Anyway, having reconstructed the octahedra, the displacement of Ti with respect to the centre of the octahedron can be examined. As explained in section 4.3.3, knowing the positions of the O atoms and of Ti allows one to calculate the displacement of every single Ti atom ($\Delta Ti_{<O>}$) in the merged configuration from the centroid of the O atoms (<O>). Figure 4.13 shows the density plots of $\Delta Ti_{<O>}$ between -0.15 Å and +0.15 Å from the centre of the octahedron.

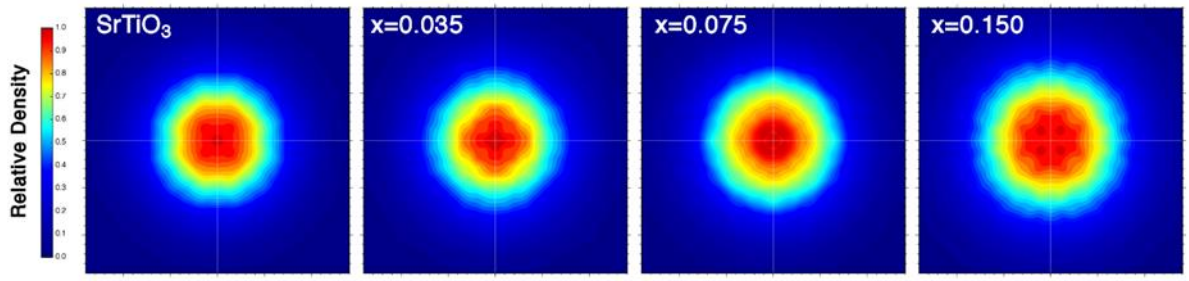

Figure 4.13: Density plots of the refined positions of the Ti atoms with respect to the centre of the oxygen atoms of the octahedron. The probability density function was obtained for all the $\Delta Ti_{<O>}$ points from 36 merged configurations. The boundaries of each plot are ±0.15 Å from the centre of the octahedron. Dark red pixels indicate where Ti atoms are most concentrated; at the other end of the scale, dark blue pixels indicate the lowest probability to find Ti atoms.

In undoped $SrTiO_3$, the highest density of Ti atoms is found at the centre of the coordinated O atoms. As Pr concentration is increased between x=0.035 and x=0.150, two effects become clear: i) a gradual increase in the mean displacement of the uniform distribution, in agreement with the increase in the isotropic thermal displacement found by Rietveld analysis; ii) a gradual split of the maximum probability density toward the <111> symmetry-equivalent directions. In particular, the maximum probability to find Ti atoms is still in the centre of the octahedron

[5] The method used to calculate tilt is actually a tradeoff between accuracy and practicality. A sounder, optimization-based approach to polyhedral geometry is implemented in the GASP program available with RMCProfile (Wells et al., 2004). The way GASP works, though, is incompatible with the aim of the program used in this work, that is, carrying out simultaneously reconstruction of polyhedra and calculation of their geometric parameters so that they can be used for any arbitrary multiple (or portion) of RMC configurations. The tilt angles reported in this section are compared to the values returned by GASP in the Appendix to this Chapter.

for x=0.035, albeit spread over a wider range; for x=0.075, maximum probability is split between the centre of the octahedron and sites displaced along the <111> directions; finally, for x=0.150, the density is highest in the off-centre sites. The density peaks in Figure 4.13 evidence that the maximum off-centering of Ti attainable for x=0.150 does not exceed $\Delta Ti_{<O>}$=0.025 Å.

When the refined structure includes the average A cation at the A-site, an off-centering of similar amplitude ($\Delta A_{<O>}$=0.025 Å) develops gradually between $SrTiO_3$ and x=0.150; Figure 4.14 shows the peak of the probability density drifting away from the centre of the cuboctahedron for x=0.075 and x=0.150.

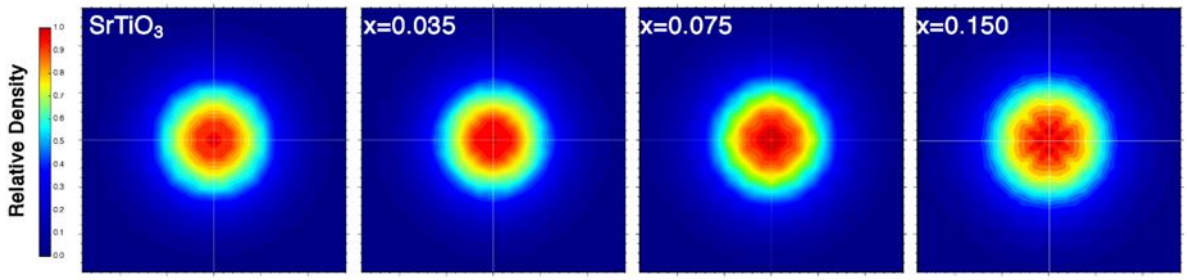

Figure 4.14: Density plots of the refined positions of the A (Sr+Pr) atoms with respect to the centre of the oxygen atoms of the octahedron. The probability density function was obtained for all the $\Delta A_{<O>}$ points from 36 merged configurations. The boundaries of each plot are ±0.15 Å from the centre of the octahedron. Dark red pixels indicate where Ti atoms are most likely to be found; at the other end of the scale, dark blue pixels indicate the lowest probability to find Ti atoms.

In spite of the off-centering of both cations for x=0.150, which should make A-Ti distances more scattered, the most evident change in the partial $g(r)$ of the A-Ti pair between $SrTiO_3$ and x=0.150 is a shift by 0.04 Å toward low-r of the nearest-neighbour peak (panel B in Figure 4.14), which was expected in the light of the smaller ionic radius of Pr^{3+} (1.19 Å) compared with Sr^{2+} (1.44 Å). As shown in panel A of Figure 4.14, the first peak of the partial $g^{Ti}(r)$ is well fitted by a single Gaussian peak in every case except x=0.150. The worse fit in the latter is only partly explained by the truncation on the low-r limit; in fact, it should be ascribed to the low-r subpeak related to Pr-Ti correlations, whose intensity becomes considerable only at x=0.150. Peak width of the first A-Ti peak is insensitive to Pr concentration after the initial increase between $SrTiO_3$ and x=0.035 (width increases by 0.005 Å), suggesting that the peak comprises two unresolved contributions from Sr-Ti and Pr-Ti pairs, and that a change in Pr concentration results in a change in their relative intensity.

Though not completely resolved, a double A-Ti peak points to the coexistence of two different coordination environments for Pr and Sr. In order to understand whether and how this is related to the gradual increase in cation off-centering with a higher Pr concentration, to the correlated

displacement observed in box-car NPDF refinements, and to the increase in tilt angle observed in XPDF, we try to separate the contribution of Pr to the total $g(r)$ from that of Sr and re-examine the local structure of SPTO in the light of the different distortions in the chemical environments of Sr and Pr. This is done by running a set of RMC refinements on the NPDF of x=0.150 including explicitly different Sr and Pr atoms at the A-site. Eventually, the plausibility of the solution returned by RMC will be checked against the structural arguments exposed previously.

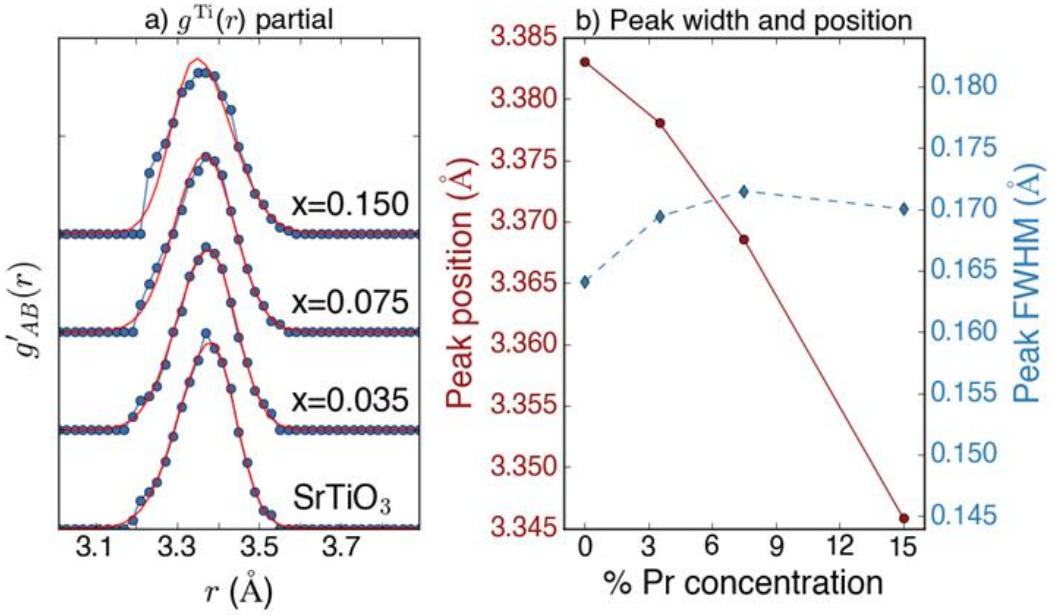

Figure 4.15: Panel A: First peak of the partial A-Ti g(r) for all four samples. In each case the average A-site cation is used instead of distinct Sr and Pr atoms. Blue circles are the calculated peak; red solid line is the fit by a split Gaussian curve. Positions and FWHM of the fitted peaks are reported in Panel B. Note that the FWHM axis has been adjusted to span the same range as the 'Peak position' axis (0.40 Å) in order to emphasize the small change in peak width.

To start with, we show the isolated contributions of Pr and Sr to the A-Ti part of the total NPDF of x=0.150. After extracting the partial $g(r)$ of Sr-Ti and Pr-Ti, the eight peaks contained in the 0-16 Å fit range are fitted with Gaussian functions; an example of fitted peaks is shown in the panel on the right of Figure 4.16 and the peak parameters are shown in the left panel. The Pr-Ti peaks are positioned consistently at a lower r-distance than the corresponding Sr-Ti peaks (Δr=0.015 Å on average), but are also broader than the Sr-Ti peaks by approximately 0.010 Å throughout the $0<r<16$ Å range. The broader, rigidly shifted distribution of Pr-Ti distances suggests that Pr is more likely than Sr to be found out of its initial position; consequently, Pr could contribute more than Sr to the small displacement of the average A-site cations (shown in Figure 4.14) despite its smaller scattering length.

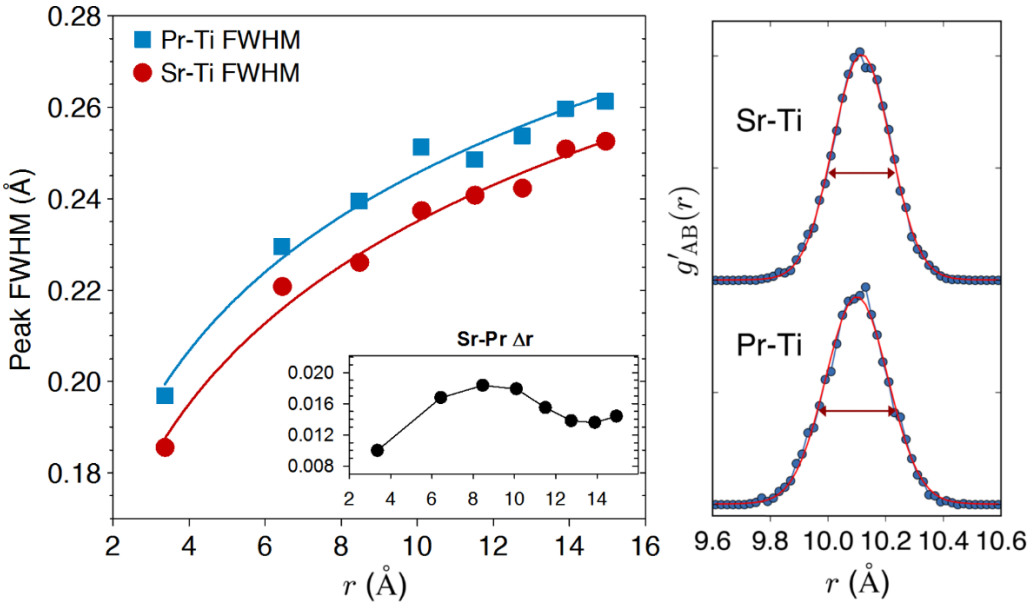

Figure 4.16: Left panel: FWHM of the peaks of the Pr-Ti and Sr-Ti partial g(r) curves for x=0.150. Inset in left panel: difference between the position of the Sr-Ti peaks and the position of the Pr-Ti peaks. Right panel: example of fitted peak in the partial g(r). Arrows represent the FWHM of the two peaks.

Next, the off-centering of Pr inside its coordination cuboctahedron is directly inspected by analysing the nearest-neighbour Pr-O correlations for x=0.150. Since off-centering could result from both a polar displacement of Pr and a rearrangement of the surrounding O atoms, the distortion is decomposed into its oxygen- and cation-related subparts. Figure 4.17 shows the density plots of the displacements $\Delta Pr_{<O>}$, ΔO, and ΔM calculated from the final merged configuration using distinct Pr and Sr sites. For a refresher of the definitions of $\Delta Pr_{<O>}$, ΔO, and ΔM, refer to section 4.3.3.

Panel A of Figure 4.17 shows a striking difference with the plots of $\Delta Ti_{<O>}$ and $\Delta Sr_{<O>}$ shown in Figures 4.13 and 4.14: the centroid of the anions is a low-density site and, instead, Pr appears to spend most of its time off-centre according to two different patterns. One comprises the sites along the <111> direction located at $\Delta Pr_{<O>}$ =0.06 Å from the centre. Another one is an eight-site (orthorhombic-like) distribution, whose circular, smeared shape strongly suggests a superposition of rotational and displacement distortions.

This $\Delta Pr_{<O>}$ distribution is broken into the subparts shown in panels B and C, corresponding to, respectively, the refined positions of the centroid of the cuboctahedron (ΔO) and the refined positions of the Pr atom alone (ΔM), both calculated with respect to the initial centre of the cuboctahedron. From the ΔO distribution shown in panel B, the superposition is evident between a large eight-site, orthorhombic-like distortion of the PrO_{12} cuboctahedron, and a smaller, more diffuse pattern; though smeared, the latter shows four distinct peaks (ΔO=0.02

Å), denoting a tetragonal-like distortion[6]. The distribution of ΔM shown in panel C, instead, reveals strong evidence only of the tetragonal-like distortion, with peaks at a distance ΔM=0.020 Å from the initial position. Still visible, but largely less likely to contain Pr atoms, are the sites along the <100> directions corresponding to a larger tetragonal distortion (ΔM=0.06 Å).

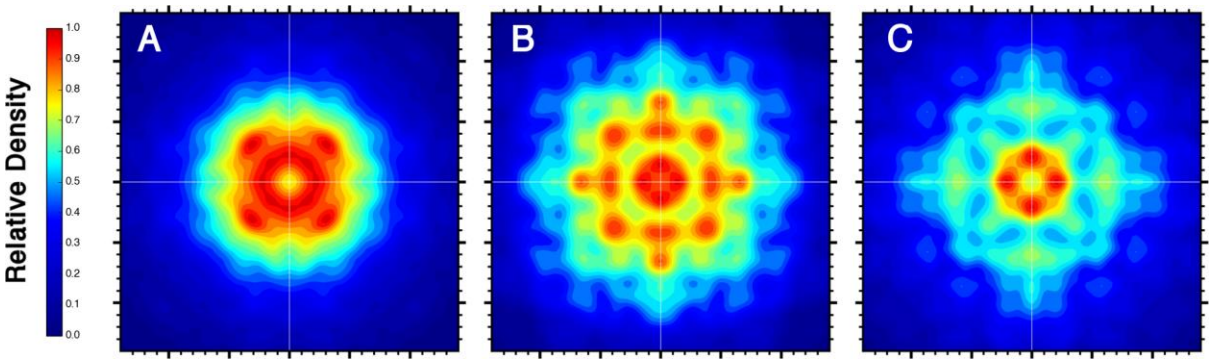

Figure 4.17: Density plots of the three types of displacement extracted from the refined positions of Pr and O atoms. Panel A: Displacement (ΔPr_O) of Pr atoms with respect to the refined centroid of the O atoms; panel B: displacement of the refined centroid of the O atoms with respect to its initial position (ΔO), i.e. from the centre of the undistorted cuboctahedron; panel C: displacement (ΔM) of Pr atoms with respect to the initial Pr position (again, with respect to the centre of the undistorted cuboctahedron). The range plotted in each panel is ±0.15 Å from the centre of the plot.

Looking back at the distribution of off-centerings $\Delta Pr_{<O>}$ in panel A, qualitative arguments can be made about the interplay between the distortion acting on O atoms and the one acting on the Pr atom. The two small, tetragonal-like distortions seem to combine positively[7], as can be evinced from a few features in the plots. First, the $\Delta Pr_{<O>}$ peaks situated along the <100> equivalent directions in the smaller distribution can be seen as the sum of collinear displacements of both <O> and Pr, since the combination of the respective displacement amplitudes is in good agreement with the position of the $\Delta Pr_{<O>}$ peaks. Second, the $\Delta Pr_{<O>}$ peaks along the diagonal in the same distribution are compatible with the combination of two displacements of <O> and Pr rotated 90° relative to each other. Third, the absence of a peak at the centre of the $\Delta Pr_{<O>}$ distribution excludes antiphase displacements of <O> and Pr, as they would cancel each other out and increase density at the centre. As to the apparent eight-site ΔO distribution, it could be the result of two different four-site distributions rotated by 45° relative to each other (see below). The four main $\Delta Pr_{<O>}$ peaks along the diagonal (at about 0.06 Å from the centre) largely reflect the ΔO peaks appearing in a similar position, although the latter

[6] A discussion based on analogous plots for $BaTiO_3$ can be found in Senn et al., 2016.
[7] It must be reminded that a displacement of the centroid of O atoms, ΔO, in the $+x+y$ sector appears as a cation off-centering, ΔPr, in the $-x-y$ sector. When talking about collinear displacements, thus, one must consider the inverse of ΔO, that is, the peak that ΔO generates in the ΔPr plot.

are slightly further off the centre (about 0.07 Å). In this case, thus, the $\Delta Pr_{<O>}$ peaks can be tentatively attributed to a negative combination of <O> and Pr displacements.

Looking further back to Figure 4.13, showing the modest off-centering of the average A-site cation, one notable difference with the case of Pr is that average A cations are not depleted from the centroid of the anions, which is instead a relatively high-probability site. More important, the absolute shifts of the average A-site cations with respect to their starting position (ΔM) do reflect the analogous displacement of Pr from its initial centre, but they do not match the off-centering of Pr inside the distorted cuboctahedron. The difference, therefore, lies in the smaller distortion affecting the average oxygen cage of AO_{12} cuboctahedra; conversely, when the environment of Pr atoms is simulated separately from that of Sr, one obtains the orthorhombic distortion cuboctahedron reported in Figure 4.17, panel B.

The last supposition is confirmed by the results of RMC refinements on x=0.150. As shown in Figure 4.18, the positions of the centroids of the anions around average A-site cations - i.e. 85% Sr and 15% Pr - and of those around Sr only are largely concentrated in the centre of the plot, i.e. very likely to retain their initial position (panels A and B, respectively). Interestingly, in both cases minor off-centre ΔO peaks hint to a distortion similar to that acting on the PrO_{12} cuboctahedra, making the high-density area roughly square-shaped. The small off-centering of the respective cation positions, however, confirms that neither of these distortions significantly breaks the symmetry of the AO_{12} cuboctahedron. A more regular SrO_{12} cuboctahedron can be also inferred by comparing the partial $g(r)$ of Sr-O and Pr-O distances (panel C in Figure 4.18). Sr-O distances appears as a sum of three subshells, in which the middle one is shifted closer to the low-r subpeak with respect to an undistorted *I*4/*mcm* model (see Figure 4.2). The Pr-O partial $g(r)$, instead, appears as a broad distribution very different from the *I*4/*mcm* model.

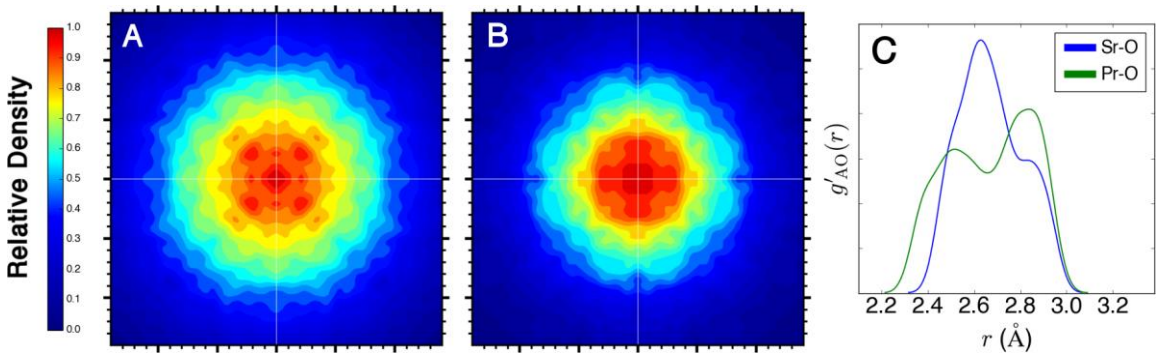

Figure 4.18: Density plots of the displacement (ΔO) of the centroid of the O atoms around the average A-site cations (panel A) and of those around Sr atoms only (panel B). Notice the increase in the mean displacement in the uniform distribution of ΔO (i.e. the part accounting for thermal motion) when Pr atoms are included (though diluted) in the average A-site cations. Panel C compares the Sr-O partial $g(r)$ calculated from the merged configuration to the analogous Pr-O partial $g(r)$.

The last part of this analysis shows how the larger distortion of the PrO_{12} cuboctahedra extends to the neighbouring TiO_6 octahedra, finally relating the off-centering of Pr and the increase in both octahedral tilt angle and Ti off-centering evidenced earlier in this chapter.

Figure 4.19 summarizes the findings on the coordination environments of Sr and Pr extended to neighbouring octahedra. To keep the analysis consistent between Sr and Pr, the respective sets of RMC configurations were sampled equally by randomly picking the same number of cations (30), thus ensuring that the solutions for Sr and Pr have the same statistical weight. Next, the polyhedral-reconstruction function (explained in 4.3.3) was adapted to recognizing the eight Ti atoms around each Sr or Pr atom picked; finally, the eight TiO_6 octahedra surrounding each Sr/Pr atom were reconstructed as usual. Sets of 300 Sr-Ti or Pr-Ti clusters (30 clusters×10 configurations for each atom type) were extracted several times to check the reproducibility of the result.

Panels A and B show typical arrangements of TiO_6 octahedra around Sr atoms and Pr atoms, respectively. The more asymmetric distortion of the octahedra surrounding Pr is demonstrated by stretched and compressed Ti-O bonds, as well as a considerable displacement of axial O atoms from their initial position. Though no particular distortion appears to dominate, the Ti-O bond distances around Sr are distorted almost as much, as measured by Baur's dispersity (d=0.0310 and 0.0318, respectively, for Sr and Pr). A model accommodating the displacements around Pr is drawn schematically in panel C, showing a single layer of octahedra for simplicity. All four octahedra are rotated by a large tilt around the *c*-axis (i.e. about the viewing direction), in accordance with the main AFD distortion mode ($a^0a^0c^-$-type tilt). But the octahedra also appear to be tilted about a second axis perpendicular to *c*, as highlighted by axial O atoms moving closer to the underbonded Pr atom (marked with purple arrows). Because of the rigidity of TiO_6 octahedra, this displacement also implies that two equatorial O atoms drift away from Pr along the <11-1> direction (marked with orange arrows); but since octahedra are not completely rigid, they distort in order to accommodate to the undercoordination of Pr. This keeps the other two equatorial O atoms close to their initial position and, thus, closer to the coordinated Pr atom (red arrows). Splitting the distribution of Pr-O distances into three groups of four (as implied by *I*4/*mcm* symmetry), the centroids of the low-*r* and high-*r* subshells are positioned farther apart than the corresponding centroids of the Sr-O distribution (panel D). In the *I*4/*mcm* structure, a broader A-O distribution translates into an increase in octahedral tilt angle, just as was observed in the XPDF analysis in section 4.2. Most important, the combined bending and tilting of the octahedra around Pr result in relative positions of the O atoms directly bonded to Pr that are still consistent with a large tilt of the type $a^0a^0c^-$ (see how the structures in Figure 4.5 and Figure 4.19 compare). This could explain why the highly distorted *I*4/*mcm* structure proposed by model-fitting the PDF is a good approximation of more complex models of disorder, such as that suggested by these RMC refinements.

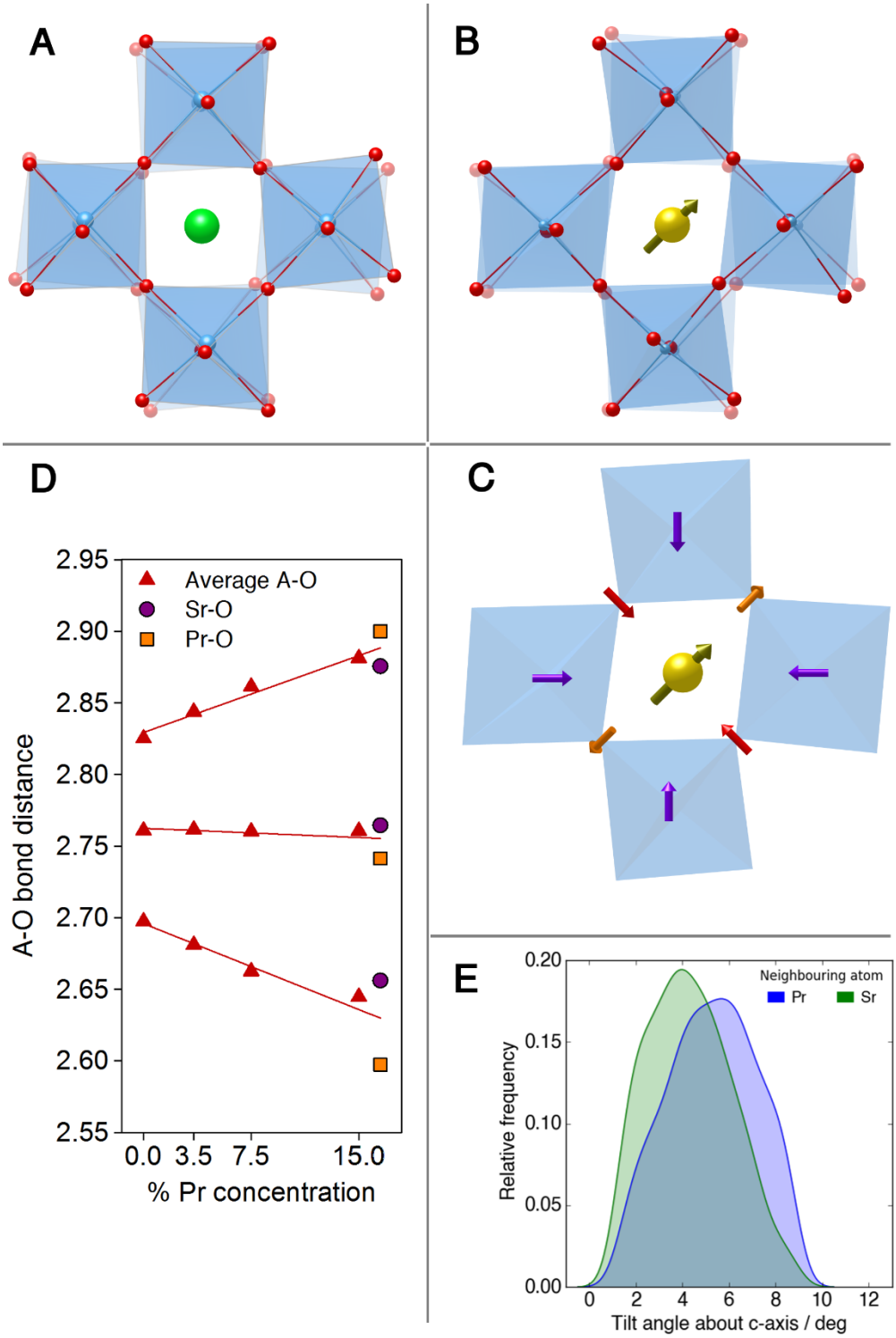

Figure 4.19: view along the c-axis of the Sr atom (green) and the Pr atom (yellow) surrounded by the neighbouring TiO_6 octahedra (panels A and B). Panel C: schematic representation of the displacements of O atoms around Pr; purple arrows represent the tilting+bending of the axial Ti-O bond towards the Pr atom; red and orange arrows show the displacement of O atoms, respectively, towards and away from the cation. Panel D: average values of A-O distances divided into three subshells for the average A cation (triangles), Pr only (squares), and Sr only (circles). Panel E: tilt angle distributions of the octahedra surrounding SrO_{12} cuboctahedra (green peak) and PrO_{12} cuboctahedra (blue peak).

Two further points must be made about octahedral tilt. First, as reported in panel E, the tilt angle of the octahedra around Pr atoms is actually larger than for Sr atoms, even when only the $a^0a^0c^-$-type tilt is considered (as explained at the beginning of 4.3.5, the tilt angle is calculated so as to be a virtually independent estimate of the $a^0a^0c^-$ tilt amplitude). Thus, regardless of the octahedral distortion, the presence of Pr atoms really enhances the amplitude of the AFD mode in the short-range; namely, the mean of the tilt distributions is 4.45° and 5.77°, respectively, in the case of Sr and Pr. Second, the octahedral distortion around Pr atoms enhances the correlation between the tilting of neighbouring octahedra along the c-axis. This is apparent by comparing the purely AFD structure in Figure 4.5 to the increasingly distorted structures shown in panels A and B of Figure 4.19. In the purely AFD structure (obtained by fitting the PDF of x=0.150 at 90 K with a $I4/mcm$ model) the tilt of octahedra situated in different layers along c is out-of-phase; this anti-correlation is largely reduced in the case of octahedra around Sr atoms (Figure 4.19.a); finally, tilt is almost completely in-phase between two adjacent layers in the case of the distorted octahedra around Pr atoms.

As to A-Ti distances, interpretation is less straightforward. The refinements suggest that the motion of both Pr and Sr is only partly coupled with the small off-centering of Ti (shown in Figure 4.13). This is apparent in the density plots of $\Delta Pr_{<Ti>}$ and $\Delta Sr_{<Ti>}$ displacements reported in Figure 4.20. Unlike the points plotted in Figures 4.13, 4.14, and 4.17, here the displacement of the central A cation (either Pr or Sr) is calculated with respect to the centroid of the eight neighbouring Ti atoms (<Ti>). The distribution of $\Delta Pr_{<Ti>}$ (panel A) has a peak in the centre of the cluster accompanied by weaker peaks situated along the <111> equivalent directions; the $\Delta Sr_{<Ti>}$ plot (panel B) shows similar off-centre peaks, mirroring the distribution of $\Delta Ti_{<O>}$ shown in Figure 4.13 (x=0.150), but also a broad high-density area around the centre. While the central peak in the overall square $\Delta Pr_{<Ti>}$ distribution points to a correlation between the motions of Pr and Ti atoms, the more uniform distribution of $\Delta Sr_{<Ti>}$ suggests that Sr positions were more likely to vary independent of Ti atoms during the RMC refinements.

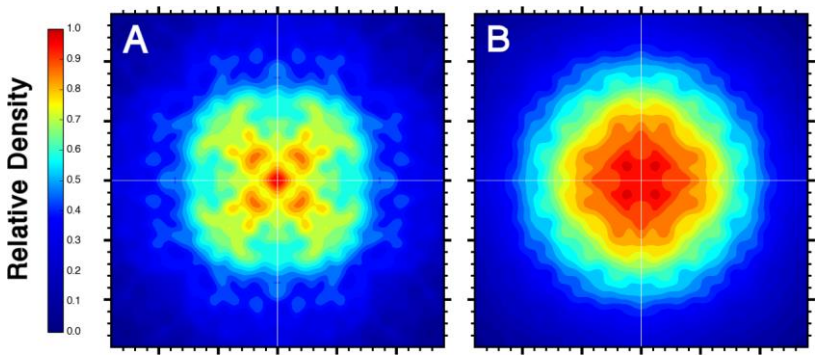

Figure 4.20: Density plots of the displacement of Pr atoms ($\Delta Pr_{<Ti>}$, panel A) or Sr atoms ($\Delta Sr_{<Ti>}$, panel B) with respect to the centroid of the eight nearest-neighbour Ti atoms.

4.4 Discussion and conclusion

Before commenting on the host of results presented, the goodness of the RMC approach used should be demonstrated on the basis of fit quality. The agreement between experimental data and the structural model provided by the RMC method is compared to the agreement attainable using direct model-fitting (as implemented in PDFGui). In Figure 4.21 the fits to the $g(r)$ carried out by RMCProfile are plotted (after conversion to the $G(r)$ function) in the left column; the fits to the $G(r)$ using a *I*4/*mcm* model are shown on the right. Least-squares refinements were carried out in the same fit range as the RMC fits ($0<r<16$ Å) by letting all structural parameters vary until convergence. Structural parameters returned by both fitting methods are reported in Table 4.2.

The RMC method returns a closer fit to the experimental NPDF than PDFGui in the case of the samples x=0.075 and x=0.150, while the agreement between data and model is comparable between the two methods for the two remaining samples, undoped $SrTiO_3$ and x=0.035 (see R_p values in Table 4.2). The dependence of fit quality on composition can be explained instinctively with a departure from an AFD structural order, at least locally, of the two samples with the highest Pr concentration. A worse fit by the *I*4/*mcm* symmetry for Pr concentration $x\geq0.075$ and, particularly, in the shortest range ($r<6$ Å) has been demonstrated through boxcar refinements in section 4.3.4. What the fitted *I*4/*mcm* model fails to capture is the correct width of the first two A-O+O-O peaks, situated around r=2.75 Å and r=4.80 Å (Figure 4.21). On the other hand, the RMC fits do not show any particular misfit, and the sine wave-like shape of the residual curves should be understood as termination ripples in the PDF not being reproduced by the function calculated by RMCProfile rather than shortcomings of the model. Nonetheless, calculated tilt angles are in good agreement between the two methods, probably as a result of reliable information from O-O peaks in the intermediate range (5-10 Å).

But even as *I*4/*mcm* fits decently the experimental PDF, the systematic superposition of distances in the perovskite structure in principle makes the fit to each $G(r)$ ambiguous. In addition, treating the occupation of a lattice site by two cations with different size and charge as an average can be a working approximation in many cases, but it makes one overlook the PDF local structural information in some others. This is the main motivation to use an unconstrained fitting procedure such as RMC. There is another shortcoming of fitting the whole 0-16 Å range with a single AFD model: the phase parameters have to adapt to a local structure that can vary sharply with r, becoming, as a result, less a quantitative measure of structural distortions than they are in limited ranges. See for instance the inconsistency of cell parameters and, thus, tetragonality values for the model-fitting method in Table 4.2.

Besides an overall closer fit to NPDF, the unconstrained model returned by RMC refinements accounts for coexistence of polar phenomena in an essentially AFD phase in SPTO.

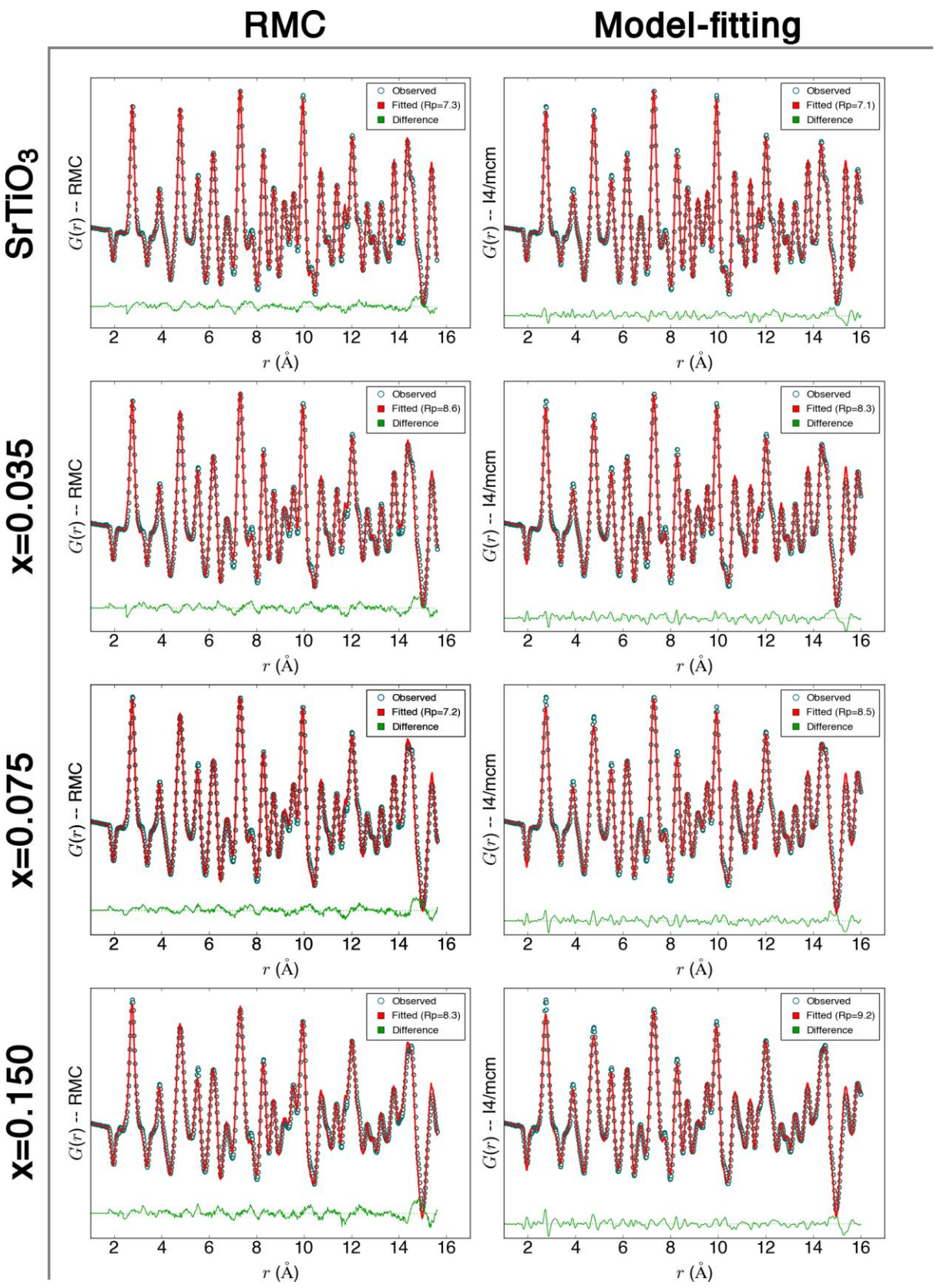

Figure 4.21: G(r) fits in the range 0-16 Å returned by RMCProfile and PDFGui (by fitting the I4/mcm model). Since the g(r) function was used for RMC analysis, the observed (circles) and calculated (solid red line) PDF curves were converted to G(r) before plotting, and fit residual curve (solid green line) and Rp were calculated accordingly, by using the appropriate scaling by r.

Table 1: Selected structural parameters returned by refinements to NPDF in the range 0-16 Å by either RMC and PDFGui fitting the I4/mcm model. The unit cell parameters reported for the RMC method were fixed on those used for reciprocal-space analysis; tilt angle was calculated as explained in 4.3.5.

	SrTiO3		**x=0.035**		**x=0.075**		**x=0.150**	
	RMC	PDFGui	RMC	PDFGui	RMC	PDFGui	RMC	PDFGui
a (Å)	5.5140	5.4939	5.5121	5.4963	5.5061	5.5017	5.5031	5.5022
c (Å)	7.8069	7.8496	7.8105	7.8425	7.8111	7.8149	7.8131	7.8057
ϕ (deg)	2.27	1.31	3.32	3.38	4.23	4.39	5.08	5.27
η	0.11	1.03	0.20	0.89	0.31	0.44	0.39	0.31
R_p (%)	7.3	7.1	8.6	8.3	7.2	8.5	8.3	9.2

The overall structure of all four sample features tilted TiO_6 octahedra and small cation displacements. While the motion of A and B cations in undoped $SrTiO_3$ and in the lightly doped x=0.035 sample appears mostly uniform, static disorder emerges clearly in the atomic configurations of the samples with x=0.075 and x=0.150.

Local tilt angle, extracted so as to reflect the amplitude of the R4+ tilt mode without interference from other distortions, matches remarkably well with the long-range tilt angle obtained by Rietveld refinements on the same data in reciprocal space. The only exception is the overestimation in the case of $SrTiO_3$, probably the consequence of instrumental-related broadening that was unaccounted for.

The remainder of the RMC analysis focuses on the highest-doped sample, x=0.150, partly because it showed appreciable cation off-centering and partly for its high Pr concentration, the only one allowing the refinement of Pr atoms as distinct species. The interatomic distances of pairs involving Pr are systematically broader than their equivalents with only Sr. This is effect is barely noticeable for Pr-Ti distances but hefty in the case of nearest-neighbour Pr-O distances. In particular, the average PrO_{12} cuboctahedron appears distorted by different modes acting simultaneously on the oxygen atoms, as evidenced by plotting all the positions taken by the centroids of the oxygen cage. The overall effect is that of an orthorhombic-like distortion that combines with a small <100> displacement of Pr to yield off-centerings directed along the <111> set of directions.

The distortion of the cuboctahedral environment of Pr necessarily propagates to the neighbouring TiO_6 octahedra, with which they share one face. These octahedra appear as more tilted according to the AFD mode, but also distorted in such a way that axial O atoms move closer to the shifted Pr atom. Future work will try to disclose whether octahedra distort as the result of multiple tilt modes or, instead, under the action of a proper ferroelectric mode. The most notable (and closest) example of multiple-irrep distortion is Ca-doped $SrTiO_3$, whose

ground state is presented by several authors as the coexistence of R- and M-point tilt instabilities and an intrinsic antiferroelectric motion of A cations (Ranjan et al., 2000; Benedek and Fennie, 2013). The resulting orthorhombic structure (space group *Pnma*) is shared with a host of other triple perovskites, but only rarely results in spontaneous ferroelectricity. Like in Ca-doped $SrTiO_3$, in SPTO ferroelectric and relaxor states may emerge at varying dopant concentration as the result of changes in the relative strength of competing local interactions (Ranjan et al., 2000).

In SPTO, in particular, the octahedral distortion observed around Pr atoms drives the Ti atoms off-centre - by forcing octahedra to tilt while being distorted - an effect more prominent as Pr concentration increases. Although it could not be proved quantitavely, the compositional dependence of Ti off-centering (Figure 4.13) matches qualitatively the local increase in the AFD order parameters (tilt angle and tetragonality) evidenced by X-ray PDF analysis. The same increase in local order parameters did not show up in neutron PDF: in fact, tetragonality was not allowed to vary in RMC refinements (since cell parameters were fixed) and local tilt angles replicated the long-range tilt angles almost exactly. But as the local increase in octahedral tilt and tetragonality is suppressed, polar atom displacements show up. This supports the picture of interdependence of large AFD distortion and FE instability, as first proposed by Aschauer and Spaldin (2014) and then experimentally observed as the correlation between polar Raman modes and local structural distortion at varying compositions.

The RMC analysis suggests that the composition-driven distortion in SPTO must be related to the increasing concentration of locally distorted clusters that form around Pr atoms. The relatively small off-centerings of A and Ti cations do, in fact, reflect the contribution of polar displacements originating from the rearrangement around off-centered Pr atoms of PrO_{12} cuboctahedra and of their neighbouring TiO_6 octahedra. The coordination environment of Sr, by contrast, shows no such distortion and is rather consistent with a pure AFD local structural order; thus, the contribution of these undistorted octahedra and cuboctahedra to the density plots of Ti and A is to place a large number of atoms in the centre of the distribution. To this point, future work will be aimed at producing partial density plots, in order to limit the analysis of the off-centering, for instance, only to distorted clusters around Pr.

Finally, a note on interlayer correlations of disorder. It was noted that the small enhancement of AFD-type octahedral tilting around Pr atoms was accompanied by a change in the interlayer correlation of octahedral tilting. The out-of-phase arrangement of tilts along the *c*-axis seen in a purely AFD structure (Figure 4.5) seems to change to an almost in-phase behaviour (Figure 4.19) in the distorted arrangement around Pr atoms. Zhong and Vanderbilt (1998) proposed correlation functions of both AFD and FE modes in strontium titanates, concluding that perfectly rigid octahedra need not be correlated along *c*, but only in the *ab* plane; conversely,

FE interactions are only weakly correlated along *a* and *b*, but those along *c* are strongly interdependent. The (purely qualitative) observation of a degree of correlation between interlayer octahedral tilts can be a hint to the mixing of AFD and FE instabilities in the local structure of SPTO.

References

Aschauer, U., & Spaldin, N. A. (2014). Competition and cooperation between antiferrodistortive and ferroelectric instabilities in the model perovskite SrTiO3. Journal of Physics: Condensed Matter, 26(12), 122203.

G. Ashiotis, G., Deschildre, A., Nawaz, Z., Wright, J.P., Karkoulis, D., Picca, F.E., and Kieffer, J. (2015). The fast azimuthal integration Python library: pyFAI, Journal of Applied Crystallography 48, 510.

Baur, W. H. (1974). The geometry of polyhedral distortions. Predictive relationships for the phosphate group. Acta Crystallographica Section B: Structural Crystallography and Crystal Chemistry, 30(5), 1195-1215.

Benedek, N. A., & Fennie, C. J. (2013). Why are there so few perovskite ferroelectrics?. The Journal of Physical Chemistry C, 117(26), 13339-13349.

Bianchi, U., Kleemann, W., and Bednorz, J. G. (1994). Journal of Physics: Condensed Matter 6, 1229.

Bianchi, U., Dec, J., Kleemann, W., & Bednorz, J. G. (1995). Cluster and domain-state dynamics of ferroelectric $Sr_{1-x}Ca_xTiO_3$ (x= 0.007). Physical Review B, 51(14), 8737.

Chong, S. Y., Szczecinski, R. J., Bridges, C. A., Tucker, M. G., Claridge, J. B., & Rosseinsky, M. J. (2012). Local Structure of a Pure Bi *A* Site Polar Perovskite Revealed by Pair Distribution Function Analysis and Reverse Monte Carlo Modeling: Correlated Off-Axis Displacements in a Rhombohedral Material. Journal of the American Chemical Society, 134(13), 5836-5849.

Coduri, M., Scavini, M., Allieta, M., Brunelli, M., & Ferrero, C. (2013). Defect structure of Y-doped ceria on different length scales. Chemistry of Materials, 25(21), 4278-4289.

Datta, K., Richter, A., Göbbels, M., Keen, D. A., & Neder, R. B. (2016). Direct mapping of microscopic polarization in ferroelectric $x(BiScO_3)$-$(1-x)(PbTiO_3)$ throughout its morphotropic phase boundary. Physical Review B, 93(6), 064102.

DiAntonio, P., Vugmeister, B. E., Toulouse, J., & Boatner, L. A. (1993). Polar fluctuations and

first-order Raman scattering in highly polarizable $KTaO_3$ crystals with off-center Li and Nb ions. Physical Review B, 47(10), 5629.

Durán, A., Martínez, E., Díaz, J. A., & Siqueiros, J. M. (2005). Ferroelectricity at room temperature in Pr-doped SrTiO3. Journal of applied physics, 97(10), 4109.

Farrow, C.L., Juhas, P., Liu, J.W., Bryndin, D., Božin, E.S., Bloch, J., Proffen, T. and Billinge, S.J.L. (2007). PDFfit2 and PDFgui: computer programs for studying nanostructure in crystals. Journal of Physics: Condensed Matter, 19(33), 335219.

Goian, V., Kamba, S., Hlinka, J., Vaněk, P., Belik, A. A., Kolodiazhnyi, T., & Petzelt, J. (2009). Polar phonon mixing in magnetoelectric EuTiO3. The European Physical Journal B, 71(3), 429-433.

Hammersley, A. P. (1998). FIT2D V10. 3 Reference Manual V4. 0. European Synchrotron Radiation Facility.

Hannon, A. C. (2005). Results on disordered materials from the GEneral Materials diffractometer, GEM, at ISIS. Nuclear Instruments and Methods in Physics Research Section A: Accelerators, Spectrometers, Detectors and Associated Equipment, 551(1), 88-107.

Hui, Q., Dove, M. T., Tucker, M. G., Redfern, S. A., & Keen, D. A. (2007). Neutron total scattering and reverse Monte Carlo study of cation ordering in $Ca_xSr_{1-x}TiO_3$. Journal of Physics: Condensed Matter, 19(33), 335214.

Keen, D. A. (2001). A comparison of various commonly used correlation functions for describing total scattering. Journal of Applied Crystallography, 34(2), 172-177.

Laurita, G., Page, K., Suzuki, S., & Seshadri, R. (2015). Average and local structure of the Pb-free ferroelectric perovskites (Sr, Sn)TiO_3 and (Ba, Ca, Sn)TiO_3. Physical Review B, 92(21), 214109.

Levin, I., Krayzman, V., & Woicik, J. C. (2014). Local structure in perovskite (Ba, Sr)TiO_3: Reverse Monte Carlo refinements from multiple measurement techniques. Physical Review B, 89(2), 024106.

Qiu, X., Thompson, J. W., & Billinge, S. J. (2004). PDFgetX2: a GUI-driven program to obtain the pair distribution function from X-ray powder diffraction data. Journal of Applied Crystallography, 37(4), 678-678.

Ranjan, R., Pandey, D., & Lalla, N. P. (2000). Novel features of Sr 1− x Ca x TiO 3 phase diagram: evidence for competing antiferroelectric and ferroelectric interactions. Physical review letters, 84(16), 3726.

Ranjan, R. Hackl, R., Chandra, A., Schmidbauer, E., Trots, D., and Boysen, H. (2007). Physical

Review B 76, 224109.

Sears, V. F. (1992). Neutron scattering lengths and cross sections. Neutron news, 3(3), 26-37.

Senn, M. S., Keen, D. A., Lucas, T. C. A., Hriljac, J. A., & Goodwin, A. L. (2016). Emergence of Long-Range Order in $BaTiO_3$ from Local Symmetry-Breaking Distortions. Physical Review Letters, 116(20), 207602.

Soper, A.K. (2012). GudrunN and GudrunX: Programs for correcting raw neutron and x-ray total scattering data to differential cross section.

Toby, B. H., & Egami, T. (1992). Accuracy of pair distribution function analysis applied to crystalline and non-crystalline materials. Acta Crystallographica Section A: Foundations of Crystallography, 48(3), 336-346.

Toulouse, J., DiAntonio, P., Vugmeister, B. E., Wang, X. M., & Knauss, L. A. (1992). Precursor effects and ferroelectric macroregions in $KTa_{1-x}Nb_xO_3$ and $K_{1-y}Li_yTaO_3$. Physical Review Letters, 68(2), 232.

Toulouse, J., Vugmeister, B. E., & Pattnaik, R. (1994). Collective Dynamics of Off-Center Ions in $K_{1-x}Li_xTaO_3$: A Model of Relaxor Behavior. Physical Review Letters, 73(25), 3467.

Tucker, M. G., Keen, D. A., Dove, M. T., Goodwin, A. L., & Hui, Q. (2007). RMCProfile: reverse Monte Carlo for polycrystalline materials. Journal of Physics: Condensed Matter, 19(33), 335218.

Vanderbilt, D., & Zhong, W. (1998). First-principles theory of structural phase transitions for perovskites: competing instabilities. Ferroelectrics, 206(1), 181-204.

Vugmeister, B. E., DiAntonio, P., & Toulouse, J. (1995). Raman Study of Cluster Dynamics in Disordered Ferroelectrics. Physical Review Letters, 75(8), 1646.

Wells, S., Dove, M., & Tucker, M. (2004). Reverse Monte Carlo with geometric analysis–RMC+ GA. Journal of Applied Crystallography, 37(4), 536-544.

Wojdyr, M. (2010). Fityk: a general-purpose peak fitting program. Journal of Applied Crystallography, 43(5), 1126-1128.

Zhong, W., & Vanderbilt, D. (1995). Competing structural instabilities in cubic perovskites. Physical review letters, 74(13), 2587.

Appendix

Neutron scattering lengths

Neutron scattering lengths are reported in 10^{-14} m (= 10 fm) units. The values in Table 4.A.1 were used to calculate the pair coefficients reported in Table 4.A.2, which were used in the RMCProfile input file to account for an average atom at a certain site. The sum at the bottom of Table 4.A.2 is the scale of the $g(r)$ function according to the definition in Keen, 2001.

Table 4.A.1: Isotope-averaged neutron coherent scattering lengths for Sr, Pr, Ti, O and their weighting by molar fraction. Coefficients for A represent the weighted average of Sr and Pr.

	$SrTiO_3$	x=0.035	x=0.075	x=0.150
Average A	0.7020	0.6934	0.6837	0.6654
Sr	0.7020			
Pr	0.4580			
Ti	-0.3438			
O	0.5803			
$b_A c_A$	0.1404	0.1387	0.1367	0.1331
$b_{Sr} c_{Sr}$	0.1404	0.1355	0.1299	0.1194
$b_{Pr} c_{Pr}$	0	0.00318	0.00684	0.01368
$b_{Ti} c_{Ti}$	-0.06876	-0.06876	-0.06876	-0.06876
$b_O c_O$	0.34818	0.34818	0.34818	0.34818

Table 4.A.2: Isotope-averaged, molar fraction-weighted pair scattering lengths. Coefficients for A represent the weighted average of Sr and Pr.

i-j	$SrTiO_3$	x=0.035	x=0.075	x=0.150
A-A	0.01971	0.01923	0.01869	0.01771
A-Ti	-0.00965	-0.00953	-0.00940	-0.00915
A-O	0.04888	0.04829	0.04761	0.04633
Sr-Sr	0.01971	0.01837	0.01688	0.01427
Sr-Pr	0	0.00043	0.00089	0.00163
Sr-Ti	-0.00965	-0.00932	-0.00893	-0.00821
Sr-O	0.04888	0.04719	0.04524	0.04159
Pr-Pr	0	0.00001	0.00005	0.00019
Pr-Ti	0	-0.00022	-0.00047	-0.00094
Pr-O	0	0.00111	0.00238	0.00476
Ti-Ti	0.00473	0.00473	0.00473	0.00473
Ti-O	-0.02394	-0.02394	-0.02394	-0.02394
O-O	0.12123	0.12123	0.12123	0.12123
$\sum_{i,j} b_i b_j c_i c_j$	0.176249	0.174828	0.173189	0.170156

Comparison to octahedral tilt angles calculated using GASP

Figure 4.A.1 shows the distribution of the tilt angles calculated by the Python program described above superposed to the distribution of the tilt angles in the same RMC configuration calculated using the program GASP. Since the GASP version used (v. 1.5) is not designed for using merged RMC configurations, the comparison is drawn on one of the 36 RMC configurations available for each dataset.

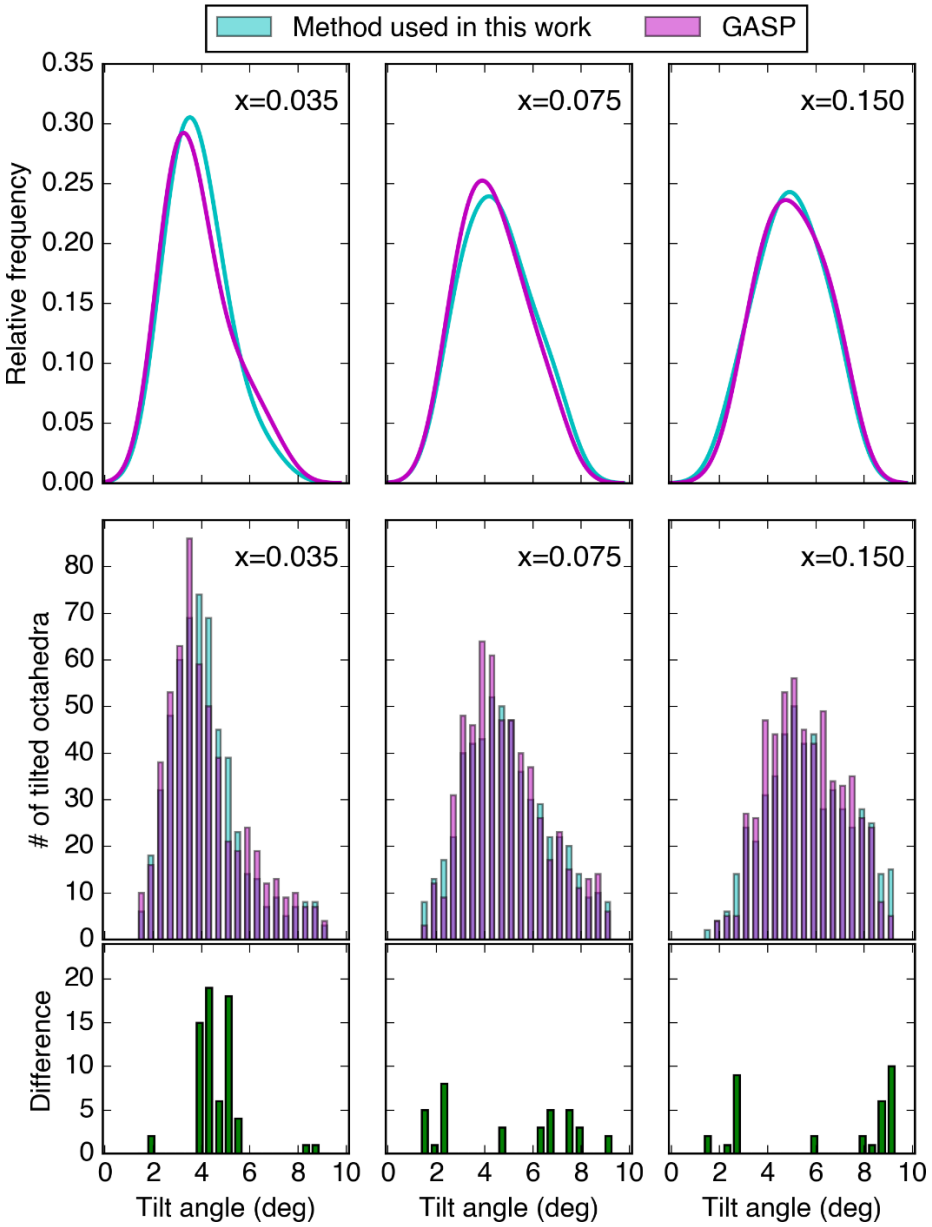

Figure 4.A.1: upper panels show the density distribution of octahedral tilt angles for all three SPTO samples as calculated by the GASP program (in magenta) and by the method used in this work (in cyan); distributions were fitted using gaussian functions with bandwith=0.75 degrees. Mid panels show the same data in histogram form (576 tilts in 25 bins). Bottom panels show the difference between the histogram values of the respective mid panels.

Flowchart of the polyhedra-reconstruction program

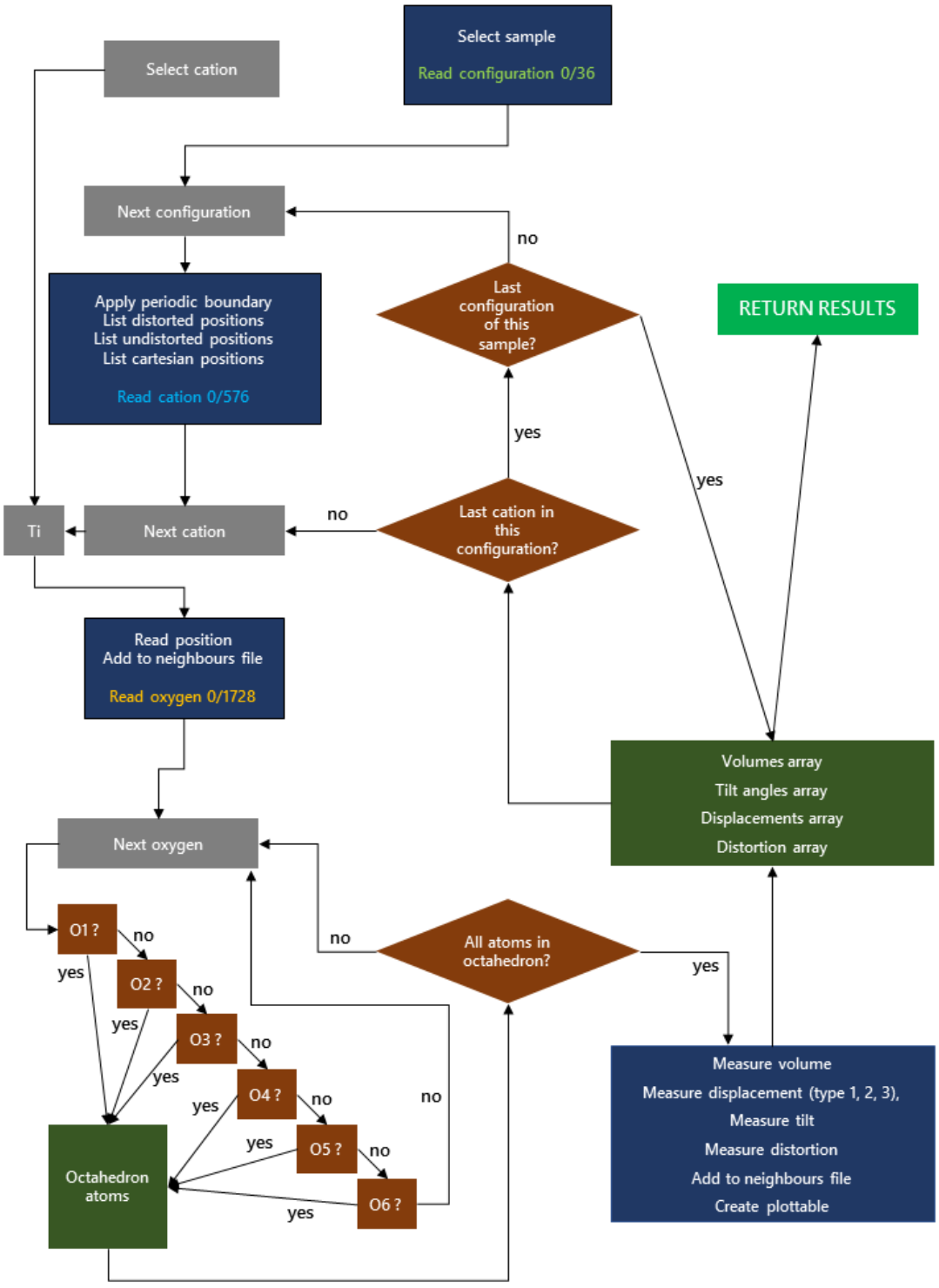

Figure 4.A.2: flowchart of the routine reconstructing octahedra in all the RMC configurations found for a sample. User inputs are sample and cation (i.e. polyhedron). Blue boxes contain calculations; green boxes are data arrays; in red boxes a condition is evaluated; grey boxes are fixed or 'continue' commands. Loops over configurations, cations, and oxygens are highlighted with a different colour.

:Chapter 5:

Symmetry-adapted PDF analysis

5.1 Introduction

5.1.1 Symmetry decomposition of cubic $SrTiO_3$

This chapter describes the analysis of neutron pair distribution function (PDF) in terms of soft phonon modes, here applied to the study of local symmetry in strontium titanate. The method used was already applied to $BaTiO_3$ by Senn and co-workers (2016), who demonstrated that polar off-centering of Ti atoms along <111> directions is maintained locally across all long-range phase transitions. As reported by some authors, the antiferrodistortive long-range symmetry of $SrTiO_3$ could be broken locally by dynamic polar clusters left behind by the incomplete freezing of the zone-centre soft mode (Hemberger et al., 1996; Blinc et al., 2005). Accordingly, some suggested that Ti could be off-centered also in $SrTiO_3$ (Uwe et al., 1989; Choi et al., 2009). From $^{16}O/^{18}O$ isotope substitution and computational studies, it was proposed that the long-range phase transition at 105 K, normally seen as purely displacive, contains an order-disorder component (Bruce et al., 1979; Zalar et al., 2005; Bussmann-Holder et al., 2007). Experimental work and first-principles calculations for $SrTiO_3$ agree that the system is unstable to both the antiferrodistortive R4+ and the polar Γ4- modes but that the absence of a ferroelectric (FE) transition is probably related to the effect of zone-centre modes being confined to short length-scales and, possibly, being dynamic. Exhaustive PDF analysis of $SrTiO_3$ as a function of temperature can help understanding the contribution of local zone-centre and zone-boundary instabilities to the average structure of $SrTiO_3$. It is therefore crucial to approach PDF analysis in terms of the separate contributions of different soft modes.

Besides the mentioned R- and Γ-point modes, there are two further low-frequency modes in $SrTiO_3$, belonging to the irreducible representations (irreps) M3+ and X5+. However, they are energetically less favourable and seem to play no role in the long-range phase transition of $SrTiO_3$. Note that these irrep labels are specific to the setting with Ti in the origin. For reasons explained below, the work presented in this chapter uses the setting with Sr in the origin, in which the four lowest-frequency modes are labelled Γ4- (unchanged), R5-, M1+, and X5-. To get all possible symmetry-breaking modes (reported in Table 5.1), full symmetry decomposition of the *Pm*-3*m* symmetry to the *P*1 space group was obtained using the program Isodistort (Campbell et al., 2006). Modes transforming as the same irrep are further divided into symmetry-adapted distortion modes. The amplitude of any of these modes is related to the order parameter of the phase transition from *Pm*-3*m* to the corresponding subgroup. With reference to the notation by Howard and Stokes (1998) introduced in paragraph 2.2.2, the modes consist of 120 degrees of freedom of atomic positions, i.e. different sets of directions and amplitudes of displacement indicated with letters from *a* to *f* . Each degree of freedom can be seen as one dimension of a global 120-dimensional parameter space or, more conveniently, of a *n*-dimensional space defined by the *n* allowed directions of the order parameter of the

mode it belongs to. As shown by Table 5.1, most of the modes are three-dimensional, but some zone-boundary modes are six-dimensional (X5+, X5-, M5+, M5-) and modes belonging to the irreps R2- and R3- irreps allow only one and two components, respectively.

Table 5.1: Full symmetry decomposition of Pm-3m obtained using the program Isodistort (Campbell et al., 2006). Irrep labels correspond to the setting with Sr in (0,0,0) used here. Irrep labels in brackets refer to the setting with Ti in (0,0,0) used in the other chapters. See text for details on notation.

Γ		**R**	
Γ4- (Γ4-)	Sr (a,b,c) T_{1u} Ti (a,b,c) T_{1u} O (a,b,c) A_{2u} O (a,b,c) E_u	R2- (R1+)	O (a,0,0) A_{2u}
		R3- (R3+)	O (a,b,0) A_{2u}
		R4- (R5+)	Sr (a,b,c) T_{1u} O (a,b,c) E_u
		R5+ (R4-)	Ti (a,b,c) T_{1u}
Γ5- (Γ4-)	O (a,b,c) E_u	R5- (R4+)	O (a,b,c) E_u
M		**X**	
M1+ (M3+)	O (a,b,c) E_u	X1+ (X3-)	Ti (a,b,c) T_{1u} O (a,b,c) E_u
M2+ (M4+)	O (a,b,c) E_u	X2+ (X4-)	O (a,b,c) E_u
M2- (M3-)	Ti (a,b,c) T_{1u} O (a,b,c) A_{2u}	X3- (X1+)	Sr (a,b,c) T_{1u} O (a,b,c) A_{2u}
M3+ (M1+)	O (a,b,c) A_{2u}	X5+ (X5-)	Ti (a,b,c,d,e,f) T_{1u} O (a,b,c,d,e,f) A_{2u} O (a,b,c,d,e,f) E_u
M3- (M2-)	Sr (a,b,c) T_{1u}		
M4+ (M2+)	O (a,b,c) A_{2u}		
M5+ (M5+)	O (a,b,c,d,e,f) E_u		
M5- (M5-)	Sr (a,b,c,d,e,f) T_{1u} Ti (a,b,c,d,e,f) T_{1u} O (a,b,c,d,e,f) E_u	X5- (X5+)	Sr (a,b,c,d,e,f) T_{1u} O (a,b,c,d,e,f) E_u

5.1.2 What method?

Chapter 4 presented two different approaches to modelling the Pair distribution function (PDF) of Pr-doped $SrTiO_3$. On the one hand, the Reverse Monte Carlo method returns unbiased structural models containing any possible distortion of the initial structure. Not only do these models often represent the best fit to the experimental data attainable, but they also can be dissected in order to identify active soft modes and evaluate their energy (Goodwin et al., 2004, 2005; Cliffe et al., 2010). On the other hand, model-fitting with PDFFit/PDFGui is a more direct approach to get quantitative structural parameters. It is normally used to evaluate the agreement between a model conjured up by the user and the experimental PDF, not unlike a Rietveld refinement (Proffen and Billinge, 1999; Farrow et al., 2007). Within a model defined

by a unit cell and a space group, some atomic positions are free to vary, and the corresponding atomic displacement should directly relate to the amplitude of a certain displacement mode in the parent structure. In fact, any symmetry-adapted mode listed in Table 5.1 is related to a phase transition from *Pm*-3*m* to one of its subgroups (Kerman et al., 2012). Therefore, fitting a model to the PDF can be seen as a particular case of measuring the amplitude of symmetry-adapted displacement modes. In the light of all this, the symmetry-adapted PDF refinements explained in the next section were planned specifically to evaluate the amplitude of all displacement modes in turn and without the bias imposed by a space group.

5.2 Description of the method

In symmetry-adapted PDF refinements, structural models representing a single set of distortions are fitted in turn to the PDF in independent PDFFit refinements. Each set of distortions is formed by the symmetry-adapted modes that belong to the same irrep (e.g. X1+). Every model is a unit cell consisting of a 2×2×2 supercell of the cubic $SrTiO_3$ structure and with *P*1 symmetry, so that the atomic positions are not related to each other by symmetry operations other than those invoked by the mode being tested. From a Rietveld perspective, this means having 8 Sr atoms, 8 Ti atoms, and 24 O atoms, each in a general *x*,*y*,*z* position, giving rise to 120 potentially refinable atomic coordinates. All atomic coordinates are kept fixed except those specific to each mode, which are controlled by the same refinable parameters. As a result, each model contains as many refinable parameters as are the degrees of freedom (a,b,c) of the modes belonging to the irrep. It must be noted that the 2×2×2 supercell size can accommodate the cell doubling brought about by any of the modes considered. The crucial step of this method is translating the 120 degrees of freedom of the *Pm*-3*m* structure into atom position constraints in the language of PDFFit. This is done using a Python 2.7 script, which is also used to set up and launch PDFFit refinements. It was necessary, however, to keep a single mode fixed. Namely, the atom situated in the cell origin need not be displaced. In view of the relevance of the zone-centre displacement of Ti to the local structure of $SrTiO_3$ structure, we decided not to keep Ti atoms fixed, but to change setting. By placing Sr in the origin, the mode Γ4- Sr (a,b,c) T_{1u}, must be switched off in every refinement.

PDF refinements were run on 11 neutron total scattering datasets collected on SrTiO3 powders at temperatures 5, 50, 75, 90, 105, 150, 200, 250, 300, 450, 600 K. Four datasets (90, 300, 450, and 600 K) were collected at the GEM diffactometer at the ISIS spallation source as described in Chapter 4. The remaining datasets were collected at GEM a few years earlier by Hui and co-workers and were first published in a RMC analysis of $SrTiO_3$ (Hui et al., 2005). Changes in instrumental resolution were taken account of by the parametrisation available in PDFFit

(Proffen & Billinge, 1999; see also Chapter 2). In addition to symmetry-adapted positional constraints defined above, other parameters refined were the lattice parameter *a*, the quadratic correlation factor of motion at low-*r* δ_2 (also described in Chapter 4), and three isotropic thermal parameters, U_{Sr}, U_{Ti}, U_O. As customary for PDFFit/PDFGui refinements the PDF function fitted was the $G(r)$, defined in Chapter 2. Initial parameter values were obtained by running few cycles refining only lattice and thermal parameters. In the case of temperatures at which the long-range symmetry of $SrTiO_3$ is tetragonal ($T \leq 105$ K), the c/a ratio was refined as well in the initial cycle, then kept fixed during the main refinement campaign. To make symmetry-adapted refinements statistically sound and unbiased with respect to the initial parameter guess, the least-squares cycle was run 500 times for each temperature-dataset, applying random shifts to the refinable parameters between each iteration. Fit quality was calculated by the residual of fit, R_p, defined in Chapters 2, 3, and 6.

All refined values and fit residuals were saved in comma-separated files and read by another Python script designed to i) merge the atomic-coordinate columns related to each mode; ii) normalise atomic coordinates to the amplitude of the corresponding mode; iii) calculate a weighted mode amplitude, the Boltzmann Weighted Mean Amplitude (BWMA) (Senn et al., 2016), calculated as $BWMA = A^*\exp[(R_{p\text{-}global}-R_p)/\sigma]$. Here, *A* stands for the sum of the mode amplitudes calculated from refined atomic coordinates; the exponential term weights refined amplitudes according to their goodness of fit (R_p) relative to the lowest fit residual ($R_{p\text{-}global}$) for the same temperature-dataset; the additional weighting factor σ (usually 0.001) is adjusted so that refinements that give poor fits or returning small refined amplitudes give arbitrary small contributions to the BWMA value. The amplitudes of three-dimensional modes are calculated by merging the columns corresponding to the *a*, *b*, *c* dimensions of the order parameter, while six-dimensional modes are arbitrarily split into two three-dimensional modes. The use of arbitrary three-dimensional basis sets is acceptable in view of the interchangeability of the displacements along the three orthogonal axes of the model cubic structure. Further tweaks to the method can include a more refined weighting system, specifying a cutoff fit residual, or limiting the number of observations. Since they have not been studied yet, they are not discussed here. However, one can get an overview of a 500-refinements cycle through diagnostic plots like those in Figure 5.1 before deciding any change to the amplitudes calculation.

Diagnostic plots of the 500-cycle PDF refinements show in practice how this approach discriminates between active and inactive modes. The top panel in Figure 5.1 shows the result for the R5- modes for the 50 K dataset, which gives the highest BWMA of R5- in the temperature series; the bottom panel shows the result of R5- at 450 K, where BWMA of R5- is zero, i.e. local octahedral tilt is absent. In Figure 5.2 the corresponding $G(r)$ fits are plotted, and the fit residuals are R_p=4.4% and 5.2%, respectively, for 50 K and 450 K. Although best-

fits are excellent at both temperatures, only the 50 K refinement denotes an active R5- mode. At 50 K virtually all refinements fall in the lowest-residual bin of the histogram, while at 450 K nearly half refinements have R_p=11% or more (out of the bounds of the plot). Additionally, scatter plots evidence that mode amplitudes tend to be smaller in the best fits at 450 K, while most refinements at 50 K converge to a single amplitude (corresponding, approximately, to a tilt angle of 2.75°, not far from the value calculated by Reverse Monte Carlo for the 90 K data, shown in Chapter 4).

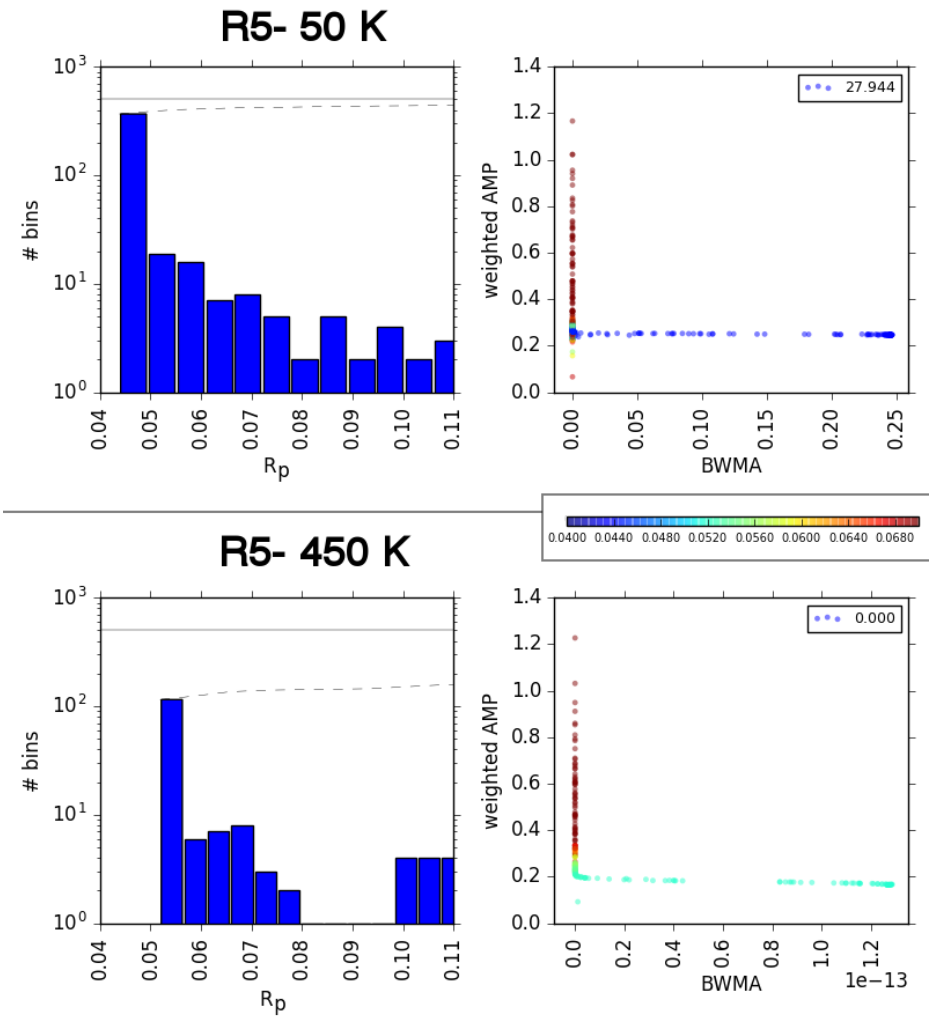

Figure 5.1: Diagnostic plots of the 500 refinement cycles of the octahedral tilt mode, R5-, at T=50 K (top) and T=450 K (bottom). The histogram on the left of each panel represents the distribution of fit residuals (R_p), in which the solid line indicates the upper limit of 500 refinements, the dashed line the cumulative sum of the histogram bins. The scatter plot on the right of each panel represents the distribution of refined mode amplitudes (weighted AMP) and their relationship to individual BWMA values through fit quality. The points are colour-coded to represent the fit residuals R_p.

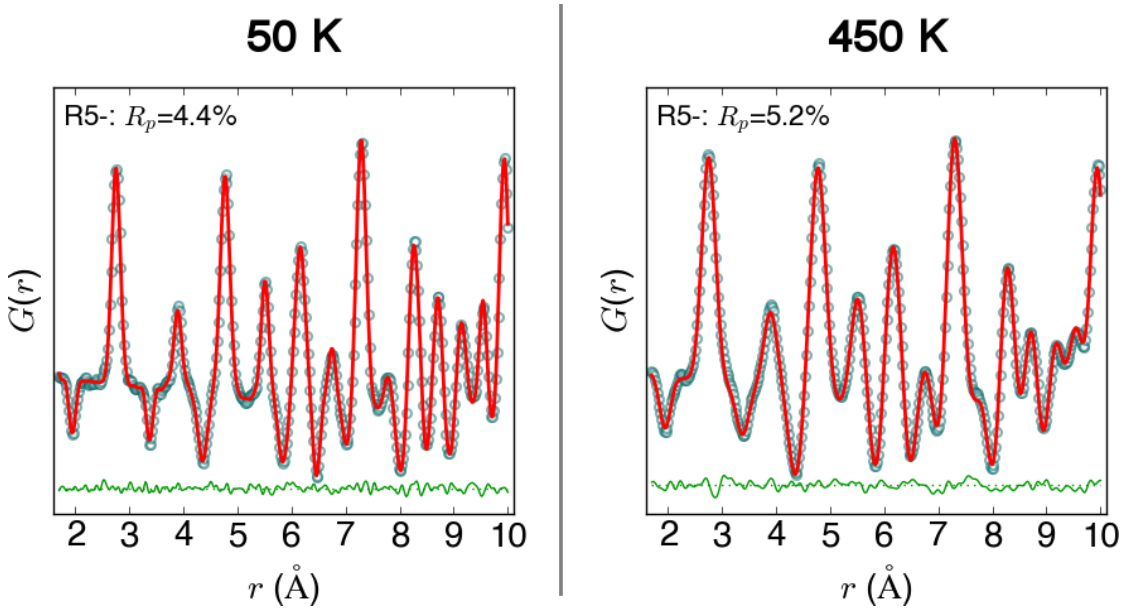

Figure 5.2: Best fits to the G(r) using the R5- model at T=50 K (left) and T=450 K (right).

5.3 Results of the symmetry-adapted refinements

Symmetry-adapted refinements were carried out for all temperature-datasets between 5 K and 600 K, highlighting the modes active in the local structure of $SrTiO_3$ in this range of temperature. Figure 5.3 shows the temperature dependence of all BWMA values of symmetry-adapted modes. The first panel shows Γ-point modes, for which, remarkably, all allowed branches of the Γ4- mode are active (note that Sr displacement is turned off), and Figure 5.4 plots the best *G*(*r*) fits attained with Γ4- at four selected temperatures. Although signatures of zone-centre modes are not a common feature in diffraction data of $SrTiO_3$, their persistence across the phase transition at 105 K and the increase in amplitude at higher temperature agree with the dynamic, order-disorder character proposed by Blinc (2005) and by Bussmann-Holder (2007). Further support comes from scatter plots of the order parameter direction for the Γ4- Ti(T_{1u}) branch, plotted in Figure 5.5. The eight-site distribution along the equivalent <111> directions points to a rhombohedral distortion like the model by Zalar et al. (2005) and the refined positions follow this pattern neatly at 600 K and 300 K. Below the cubic-tetragonal phase transition, however, each site splits into three distinct sites about the cubic threefold axis at 90 K, which become additionally inclined with respect to <111> at 5 K. An analogous pattern is exhibited by the order parameter of the branch Γ4- O(E_u) at the same temperatures. The distribution of directions about <111> can be seen as a monoclinic distortion of a local rhombohedral symmetry (i.e. increasing <110> components of displacement): this has been observed in piezolectric $Na_{0.5}Bi_{0.5}TiO_3$ at 10 K (Keeble et al., 2013) as 'bifurcated' polarization, but a local monoclinic symmetry might also arise by overlap with a rotational mode like R5- (Campbell et al., 2006). In these refinements, however, only single-irrep modes

are tested - under the harmonic approximation. This has roots also in the impracticality of combining multiple modes in a least-squares refinement, as it would overparametrise the fit, leading to unstable refinements and parameter correlation.

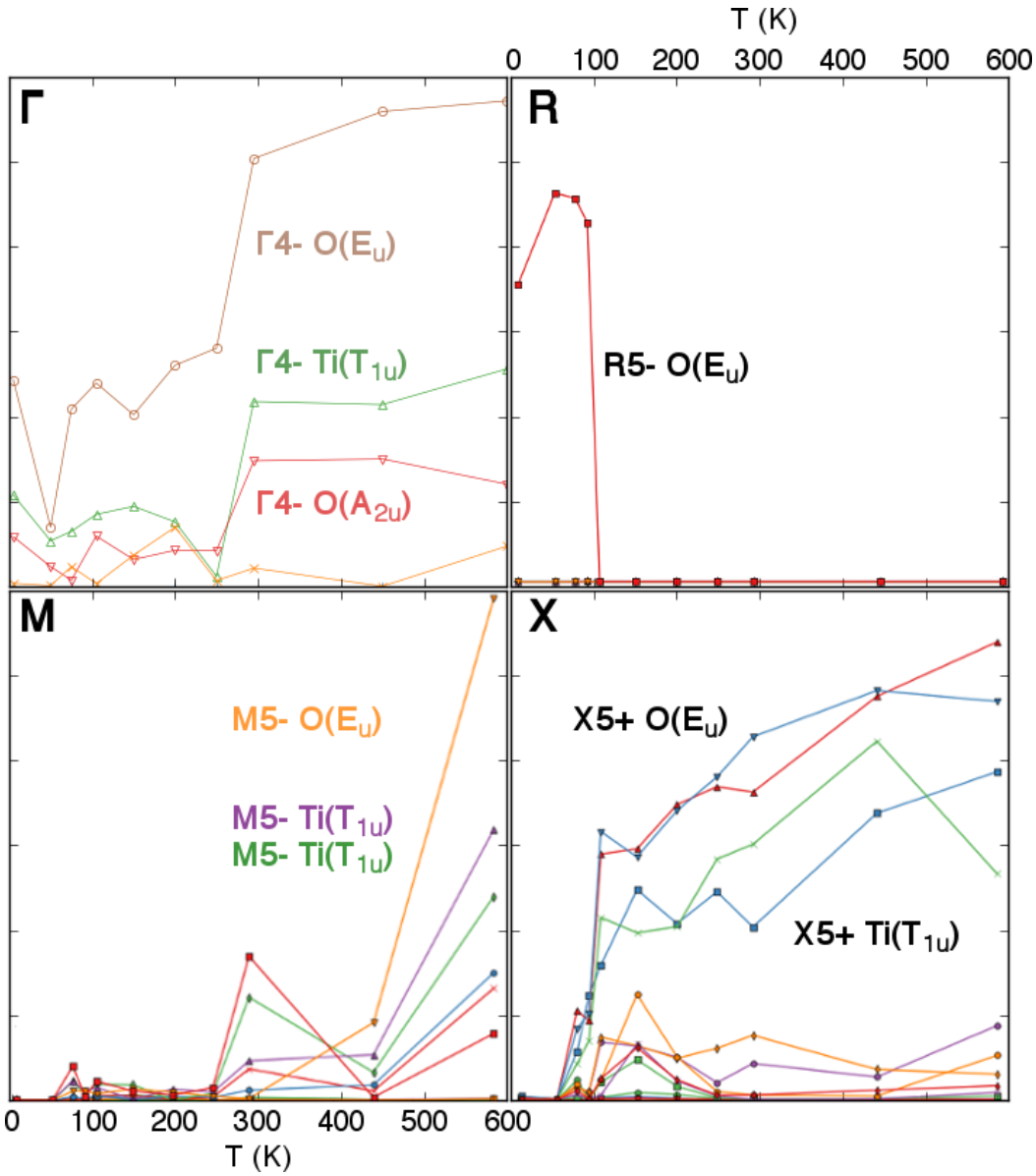

Figure 5.3: Overview of the BWMA amplitudes of all symmetry-adapted modes plotted as a function of temperature between 5 K and 600 K. The most intense modes are labelled with irrep label, atom type, and the symmetry of the irrep. In the X panel, X5+ O(E_u) comprises both the red and the blue curves, and X5+ Ti(T_{1u}) comprises both the green and the blue curves.

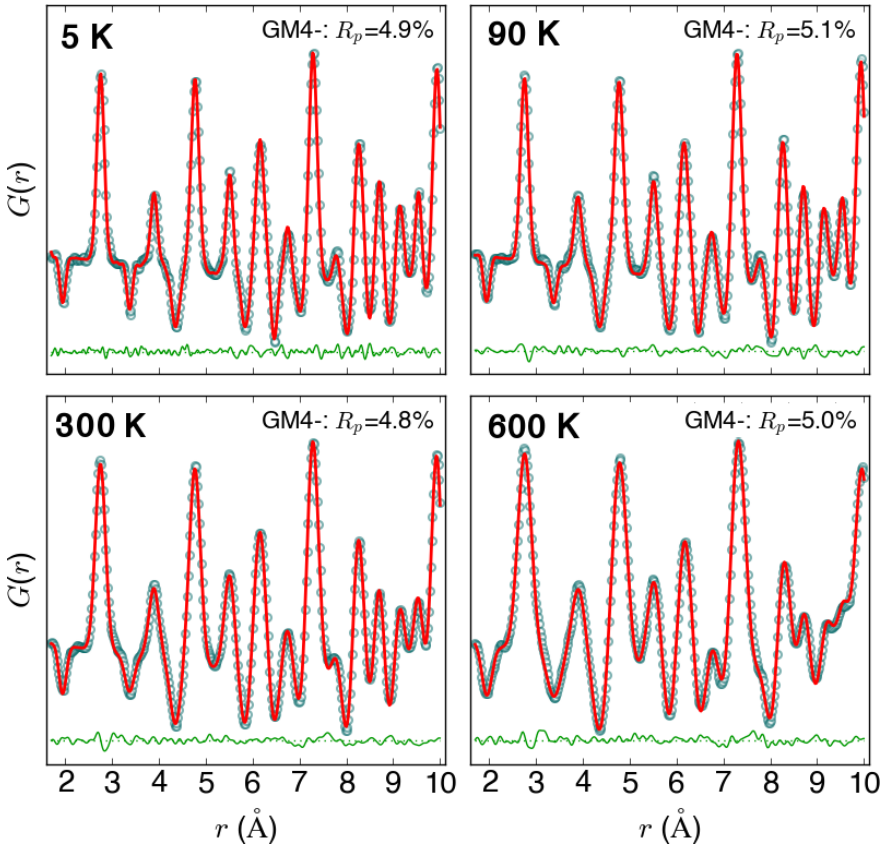

Figure 5.4: Best G(r) fits at selected temperatures using the Γ4- model.

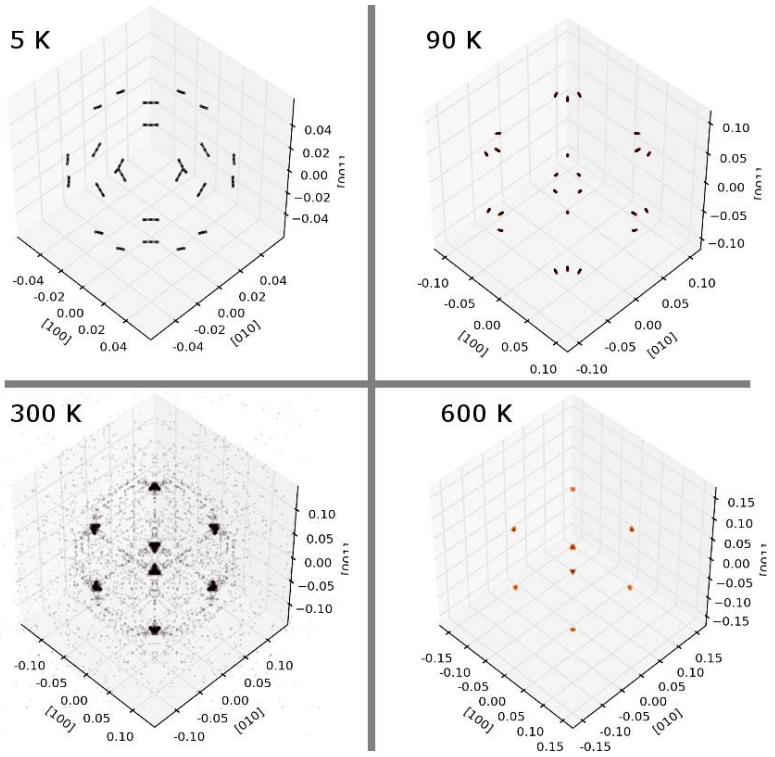

Figure 5.5: Scatter plots of the order parameter directions of the Γ4- Ti(T_{1u}) mode at selected temperatures.

The second panel (in clockwise order) in Figure 5.3 shows R-point modes. They all have zero amplitude throughout the 5-600 K range, with the exception of the soft mode R5- O(E_u). This is the mode responsible for the long-range phase transition and it shows up consistently in every $G(r)$ up to 105 K. The intensity trend and, especially, the definitive vanishing at 105 K demonstrate that the long-range octahedral tilting is not affected by either local structure or dynamics. The next panel shows X-point modes, among which only two branches of the six-dimensional X5+ have considerable amplitude. Again, the favoured distortion involves the modes O(E_u) and Ti(T_{1u}) but not the O(A_{2u}) branch. Interestingly, the BWMA amplitudes of these X5+ modes become non-zero only above T=105 K, when the long-range structure is no longer unstable to the R5- tilt mode. The zone-centre modes, by contrast, are active across the phase transition, and above 105 K coexists with a different zone-boundary mode, the antiferroelectric X5+. In analogy with X5+, the six-dimensional modes M5- O(E_u) and M5- Ti(T_{1u}) are the preferred distortions at the M-point. The apparent spike at 300 K and the abrupt increase in BWMA at 600 K, however, cast doubts on the physical significance of the M5- instability. According to the phonon structure shown in Chapter 1, M5- has a slightly higher energy than the more favourable M4+ (103 cm^{-1} vs 64 cm^{-1}). But, more important, one of the M5- components belongs to the same branch of the phonon dispersion curve as modes of the X5+, R5-, and Γ4- irreps.

5.4 Eigenvector analysis

Symmetry-adapted PDF refinements evidenced which of the modes listed in Table 5.1 are active at which temperature, and, particularly, they were sensitive to four soft modes indicated independently by DFT calculations. Although the sensible modes have been pinned down, their description is redundant. In fact, BWMA values contain the average over three dimensions of the order parameter associated with each mode. This means assuming the most general case - leading to $P1$ symmetry and indicated with the vector (a,b,c) [or (a,b,c,d,e,f) for 6-D] - in which all three (or six) degrees of freedom contribute with different amplitudes to the mode. To understand which particular order parameter direction dictates the local symmetry, we obtain the weight of the single degrees of freedoms on the mode amplitudes by eigenvector analysis. This is done by calculating the covariance matrix of every parameter matrix consisting of 500 rows by n columns, with n the number of degrees of freedom to be evaluated (i.e. the dimension of the order parameter) and 500 the number of independent observations (refinements). The covariance matrix of the n×500 is an n×n square matrix whose eigenvectors represent the favoured directions of the order parameter and the corresponding eigenvalues the scales of these directions. Put more simply, the order parameter is expressed through the covariance matrix as a linear combination of its component directions (i.e the eigenvectors).

The simplest case to apply eigenvector analysis is for extracting the actual dimension of the R5- O(E_u) order parameter. The 3×500 matrix was built using the same refined values used for BWMA calculation and the covariance matrix was calculated. The eigenvectors associated with the largest eigenvalues at each temperature are shown in Figure 5.6. It should be immediately clear that a single value in the eigenvector dominates the R5- mode, meaning that one degree of freedom contributes to mode amplitude much more than the other two. With the exception of a partial degeneracy at the phase transition (105 K) and one at 300 K, the real order parameter of the R5- mode is thus always (a,0,0), which corresponds to the transition to the *I*4/*mcm* space group. It must be reminded that i) the a,b,c components can be exchanged due to the equivalence of the orthogonal cubic axes; ii) negative and positive values are also interchangeable, since a negative tilt must be followed by a positive tilt in the successive octahedra according to the $a^0a^0c^-$ tilt system. Therefore, this analysis identified without any prior bias the octahedral tilt mode in $SrTiO_3$ only using local structure analysis.

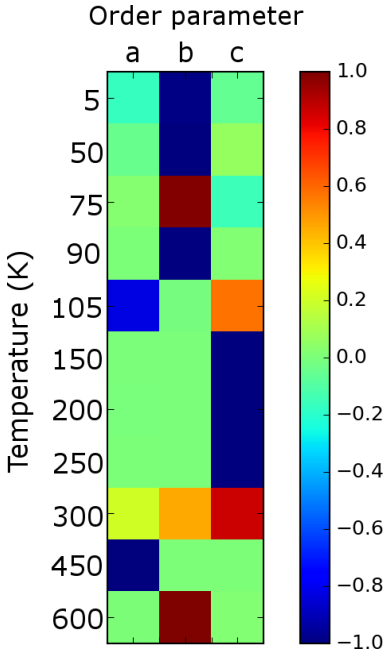

Figure 5.6: Table of the values of the eigenvectors associated with the largest eigenvalues of the covariance matrix of the order parameters of the R5- refined model at every temperature.

The other case shown here is the decomposition of the three six-dimensional branches of the X5+ irrep [Ti(T_{1u}), O(A_{2u}), O(E_u)]. For each temperature, the full 18×500 matrix was reduced to its covariance matrix and the 18 eigenvectors were plotted together sorted by the respective eigenvalues in descending order. Four selected temperatures (5, 90, 300, and 600 K) are shown in Figure 5.7. At 300 K and 600 K, the 12 largest eigenvectors are clearly different from the last 6. The 12 largest eigenvectors contain large cross-terms for the branches Ti(T_{1u}) and O(E_u) and only near-zero values for O(A_{2u}); the last 6 eigenvectors, conversely, show that when the

$O(A_{2u})$ branch contributes to the amplitude of the X5+ mode, this is the only active branch. At temperatures under the phase transition (90 K, 5 K), at which X5+ does not seem to be active, the same correlations are still present but are extremely weak, as the eigenvectors are visibly more random.

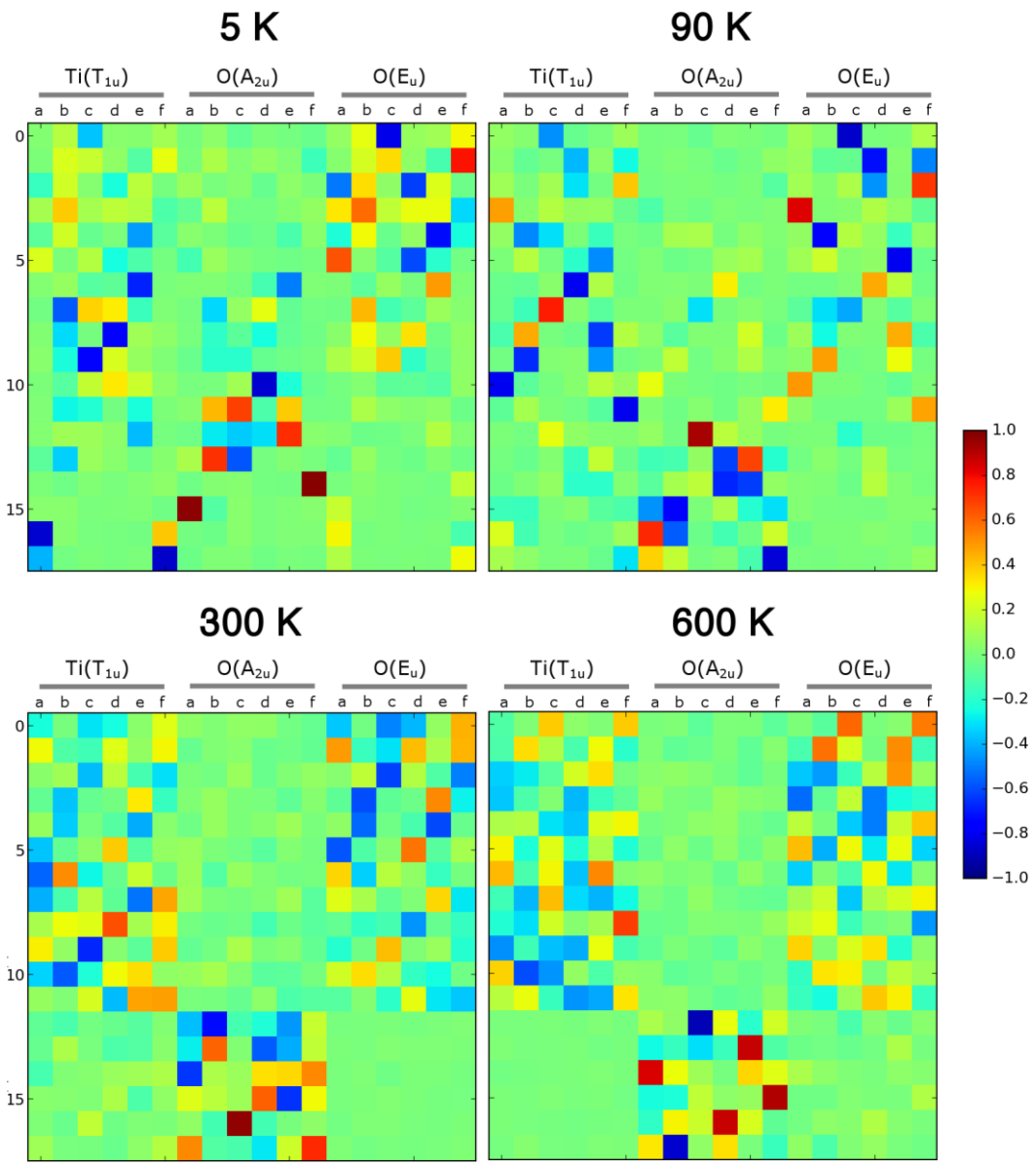

Figure 5.7: Tables of the values of all 18 eigenvectors of the covariance matrix of the order parameters of the X5+ refined model at four selected temperatures. At 5 K and 90 K, the X5+ mode has zero BWMA; instead, it is active at 300 K and 600 K. The tables should be seen as composed of three columns, indicated with the a-f components and the label of the respective branch.

Eigenvector analysis, thus, confirms that the X5+ irrep is mainly driven by the Ti(T_{1u}) and O(E_u) modes, but also that the amplitude of the O(A_{2u}) branch does not correlate with the other two. As to the dimensionality of the mode, Figure 5.8 shows the table of the eigenvectors associated with the largest eigenvalues at every temperature. It can be seen that the mode starts as two-dimensional [(0,0,*a*,0,0,0 | 0,0,*a*,0,0,0) and permutations] at low-temperature, then it splits into four large active compoonents. Some weak values of the eigenvector suggest some degree of degeneracy owing, perhaps, to parameter correlation in the least-squares refinements since 18 positional parameters were being refined together.

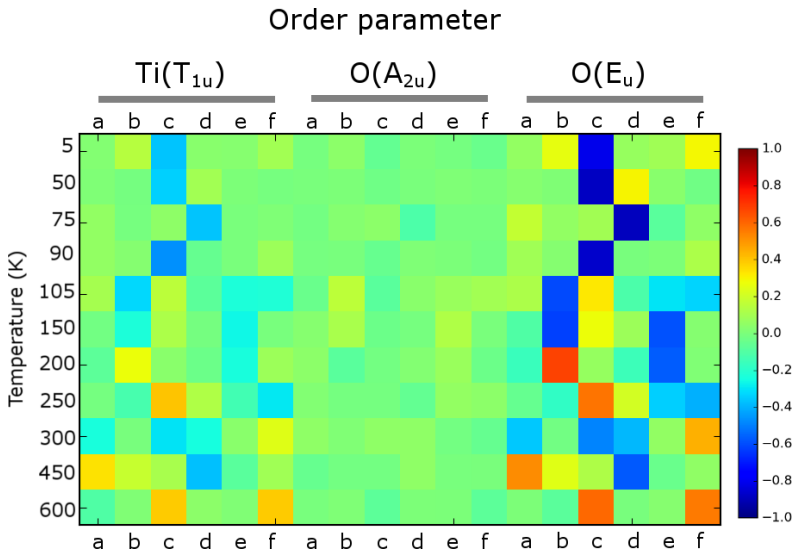

Figure 5.8: Table of the eigenvectors associated with the largest eigenvalues of the covariance matrix of the order parameters of the X5+ refined model at every temperature. The table should be seen as composed of three columns, indicated with the a-f components and the label of the respective branch.

5.5 Discussion and development

The unbiased analysis of neutron PDF by symmetry-adapted refinements gave information on the precise modes active in $SrTiO_3$ in the range of temperature 5-600 K. Although the study is still in progress and the results presented here are not conclusive, some interesting features were highlighted:

i) the local structure of $SrTiO_3$ from diffraction is compatible with a dynamic, zone-centre polar distortion; this takes the form of rhombohedrally-displaced Ti atoms, possibly combined with octahedral tilt or another Γ mode.

ii) this approach to PDF modelling has good sensitivity to the lowest-frequency modes predicted by phonon dispersion curves calculated by DFT. Modes belonging to the irreps Γ4-, R5-, X5+, and M5- were identified as the only active by their refined amplitude, BWMA.

iii) analysis of the eigenvectors of the refined parameters showed without prior bias that the rotational mode in $SrTiO_3$ has a single active component corresponding to the *I*4/*mcm* symmetry.

The final aim of this work will be to refine a model containing only the active components of the active soft modes, which would give a quantitative measure of atom displacements and tilt angle. The soft mode amplitudes thus obtained can be used to calculate the corresponding phonon energies to be compared to those calculated by DFT. A method for obtaining phonon energies from neutron total scattering data was proposed by Goodwin et al (2004, 2005).

Finally, it must be remarked that determining dynamical quantities by PDF requires measuring the inelastic, coherent component of total scattering. This can be achieved with a number of instrumental setups for both X-ray and neutron scattering, but not, for instance, when energy-discriminating analyzer crystals are used before the detector, since they cut the inelastically scattered photons.

References

Aschauer, U., & Spaldin, N. A. (2014). Competition and cooperation between antiferrodistortive and ferroelectric instabilities in the model perovskite $SrTiO_3$. Journal of Physics: Condensed Matter, 26(12), 122203.

Bruce, A. D., Müller, K. A., & Berlinger, W. (1979). Order-disorder behavior at displacive structural phase transitions. Physical Review Letters, 42(3), 185.

Bussmann-Holder, A., Büttner, H., & Bishop, A. R. (2007). Polar-Soft-Mode-Driven Structural Phase Transition in $SrTiO_3$. Physical Review Letters, 99(16), 167603.

Campbell, B. J., Stokes, H. T., Tanner, D. E., & Hatch, D. M. (2006). ISODISPLACE: a web-based tool for exploring structural distortions. Journal of Applied Crystallography, 39(4), 607-614.

Choi, M., Oba, F., & Tanaka, I. (2009). Role of Ti antisitelike defects in $SrTiO_3$. Physical Review Letters, 103(18), 185502.

Cliffe, M. J., Dove, M. T., Drabold, D. A., & Goodwin, A. L. (2010). Structure determination of disordered materials from diffraction data. Physical Review Letters, 104(12), 125501.

Goodwin, A. L., Tucker, M. G., Dove, M. T., & Keen, D. A. (2004). Phonons from powder diffraction: a quantitative model-independent evaluation. Physical Review Letters, 93(7), 075502.

Goodwin, A. L., Tucker, M. G., Cope, E. R., Dove, M. T., & Keen, D. A. (2005). Model-independent extraction of dynamical information from powder diffraction data. Physical Review B, 72(21), 214304.

Hemberger, J., Nicklas, M., Viana, R., Lunkenheimer, P., Loidl, A., & Böhmer, R. (1996). Quantum paraelectric and induced ferroelectric states in $SrTiO_3$. Journal of Physics: Condensed Matter, 8(25), 4673.

Howard, C. J., & Stokes, H. T. (1998). Group-theoretical analysis of octahedral tilting in perovskites. Acta Crystallographica Section B: Structural Science, 54(6), 782-789.

Hui, Q., Tucker, M. G., Dove, M. T., Wells, S. A., & Keen, D. A. (2005). Total scattering and reverse Monte Carlo study of the 105 K displacive phase transition in strontium titanate. Journal of Physics: Condensed Matter, 17(5), S111.

Keeble, D. S., Barney, E. R., Keen, D. A., Tucker, M. G., Kreisel, J., & Thomas, P. A. (2013). Bifurcated Polarization Rotation in Bismuth ‐ Based Piezoelectrics. Advanced Functional Materials, 23(2), 185-190.

Kerman, S., Campbell, B. J., Satyavarapu, K. K., Stokes, H. T., Perselli, F., & Evans, J. S. O. (2012). The superstructure determination of displacive distortions via symmetry-mode analysis. Acta Crystallographica Section A: Foundations of Crystallography, 68(2), 222-234.

Proffen, T., & Billinge, S. J. L. (1999). PDFFIT, a program for full profile structural refinement of the atomic pair distribution function. Journal of Applied Crystallography, 32(3), 572-575.

Senn, M. S., Keen, D. A., Lucas, T. C. A., Hriljac, J. A., & Goodwin, A. L. (2016). Emergence of Long-Range Order in $BaTiO_3$ from Local Symmetry-Breaking Distortions. Physical Review Letters, 116(20), 207602.

Uwe, H., Yamaguchi, H., & Sakudo, T. (1989). Ferroelectric microregion in $KTa_{1-x}Nb_xO_3$ and $SrTiO_3$. Ferroelectrics, 96(1), 123-126.

Zalar, B., Lebar, A., Seliger, J., Blinc, R., Laguta, V. V., & Itoh, M. (2005). NMR study of disorder in $BaTiO_3$ and $SrTiO_3$. Physical Review B, 71(6), 064107.

:Chapter 6:

Multiscale PDF refinement: the case of Y-doped CeO_2

The results presented here were published in Powder Diffraction: Checchia, S., Scavini, M., Allieta, M., Brunelli, M., Ferrero, C., & Coduri, M. (2015). Size and spatial correlation of defective domains in yttrium-doped CeO_2. Powder Diffraction, 30(S1), S119-S126.

6.1 Introduction

Cerium oxide is a compound widely investigated for its capability of forming solid solutions in the whole composition range with oxides of rare earths, transition metals (Minervini et al., 1999; Foschini et al., 2001), and group III cations (Park et al., 2000; Gregori et al., 2011). Donor-doped cerium oxides are often formed by substituting Ce^{4+} with trivalent cations from rare-earth sesquioxides in order to introduce oxygen vacancies according to the equilibrium equation (1):

$$\frac{1}{2}\, M_2O_3 \xrightarrow{CeO_2} M'_{Ce} + \frac{1}{2} V_{\ddot{O}} + \frac{3}{2} O_O \qquad (1)$$

Oxide-ion vacancies provide doped cerium oxides with an ionic conductivity as high as that of yttria-stabilised-zirconia, while electronic conductivity is kept remarkably low. This made doped ceria a prospective electrolyte layer for intermediate-temperature (800-1000 K) solid-oxide fuel cells. Because the mechanism of ionic conductivity in oxygen-deficient ceria is the diffusion of oxygen vacancies, conductivity has an inverse dependence on the activation energy needed for vacany migration. Thus, understanding the chemical environment around the oxygen vacancies is paramount to control the ionic conductivity in doped ceria. In one limiting case, two compensating defects cluster together, oxygen vacancies are trapped in the sites next to the trivalent dopant cations (Goodenough, 2003); the ensuing high activation energy barrier for vacancy diffusion is predict to suppress ionic conductivity. In the opposite scenario, oxygen vacancies are not associated with the dopant atom, but scattered randomly in the lattice; consequently, the activation barrier for migration would be low, promoting ionic conductivity.

There is no definitive agreement in the literature on how and even if the defects in doped ceria are aggregated in space. Conclusions are mainly biased by the experimental techniques used to investigate the defect structure. Bulk probes like EXAFS and solid-state NMR (Yamazaki et al., 2000; Kim and Stebbins, 2007) suggest the formation of $M'_{Ce} - V_{\ddot{O}} - M'_{Ce}$ trimers; such techniques, however, are dominated by the contribution of nearest-neighbour correlations. Conversely, electron microscopy probes like TEM, SAED and EELS (Ou et al., 2006) suggest defect clustering up to a few nanometres; in this case, however, the limited region probed may not be representative of the whole material. Partial confirmation of the clustering model came from

PDF studies of ceria doped with Gd (Scavini et al., 2012), Y (Coduri et al., 2013a; Coduri et al., 2012a) and other rare earths (Coduri et al., 2012b), also under fuel cell operating conditions (Coduri *et al.*, 2013b). The key findings of these analyses cited above can be summarized as follows: i) the first coordination spheres in doped ceria samples can be pictured as the coexistence of dopant-rich and Ce-rich 'droplets', i.e. sub-nanometre regions with a distorted fluorite (CeO_2) or C-type (M_2O_3, with M the dopant atom) structure. The relative amount of the two types of droplets mirrors the overall stoichiometry (Coduri et al., 2012a, Coduri et al., 2012b, Scavini et al., 2012, Coduri et al., 2013b). ii) at intermediate dopant concentrations ($0.25 \leq \mu < 0.50$), the dopant-rich droplets spatially average out to C-type (dopant oxide-like) 'domains', the size of which spans some hundreds of Ångstroms (Coduri et al., 2013a). iii) C-type domains grow in size with increasing dopant concentration, and connect through antiphase domain boundaries (APDB). The intensity of APDBs, which appear in the reciprocal space patterns as the selective line broadening of superstructure reflections (Coduri et al., 2013b), fades away with increasing dopant concentration.

The advantage of the PDF analysis over EXAFS demonstrated by the works cited above lies in that the PDF information can span several hundreds of Ångstroms in real space, provided the instrumental Q-resolution is very high ($\Delta Q/Q \sim 10^{-4}$). In this work, the robustness of the PDF information at , we addressed specifically the spatial correlation of defects by reviewing a few structural models by which one can describe the distribution of defects in Y-doped cerium oxide. These five structural models are compared on the basis of their ability to fit to the experimental PDF curves for different dopant concentrations in successive ranges of interatomic distances, up to a maximum of 400 Å.

6.2 Experimental

6.2.1 Synthesis of $Ce_{1-\mu}Y_{\mu}O_{2-\mu/2}$

Powdered samples of Y-doped ceria, $Ce_{1-\mu}Y_{\mu}O_{2-\mu/2}$, were prepared according to the Pechini sol-gel method (Pechini, 1967), using $Ce(NO_3)_3$ and $Y(NO_3)_3$ (99% and 99.8%, Sigma-Aldrich) in due proportions. The precursor powders from the hydrothermal synthesis were uniaxially pressed with a 7 t load to 2 mm-thick pellets, and sintered at 1173 K for 144 h with intermediate grindings. The nominal compositions are μ=0, 0.250, 0.313, 0.344, 0.438, 0.500.

6.2.2 X-ray diffraction data collection, processing and analysis

XRPD patterns were collected at the ID22 beamline (formerly ID31) of the ESRF, Grenoble. Isothermal measurements were carried out by setting T=90 K. The X-ray wavelength was λ_1=0.35413(3) Å, and data were collected up to Q_{max}=29.4 Å^{-1}. The sample with μ=0.500 was measured in a separate experiment, using a wavelength λ_2=0.3099(2) Å, reaching Q_{max}=28.0 Å^{-1}. The scattering by the empty capillary was measured and subtracted from the total diffracted intensity prior to obtaining the PDF data.

The XRPD data were fitted using both the Rietveld method via the GSAS program (Larson and von Dreele, 2000) and its graphic interface EXPGUI (Toby, 2001), and the Whole Powder Pattern Modelling (WPPM) approach as implemented by the PM2K code (Leoni et al., 2006). $G(r)$ curves were obtained through the PDFGetX2 program (Qiu et al., 2004), and modelled with the PDFgui program (Farrow et al., 2007). The PDF function used is the $G(r)$ defined in chapter 2 based on the work by Keen (2001). The r-dependent fits to the $G(r)$ curves were obtained through 'box-car' refinements: selected structural parameters were iteratively refined throughout 20 Å wide boxes covering a range up to 500 Å, depending on model and sample. Thus, the variable r in the plots stands for the centroid of the 'box-car' refinement range. The agreement between model and experimental data is measured by the fit residual (R_p):

$$R_p = \left[\frac{\sum wi(G_i^{exp} - G_i^{calc})^2}{\sum wi(G_i^{exp})^2}\right]^{\frac{1}{2}}$$

where G_i^{exp} and G_i^{calc} are the i-th point of the experimental $G(r)$ and of the calculated $G(r)$, respectively, and w_i is the weight of each point G_i^{exp} (normally the uncertainty on its value).

6.3 Results and Discussion

The fluorite structure of CeO_2 is described by the space group Fm-3m (225). In the CeO_2 cell, Ce^{4+} occupies the (0,0,0) position and has 8 coordinated O^{2-} located in (1/4,1/4,1/4). The C-type structure of Y_2O_3, space group Ia-3 (206), can be seen as a 2×2×2 fluorite supercell whose origin is shifted by 1/4,1/4,1/4. In each octant, Y^{3+} occupies the 6-fold coordinated *8b* and *24d* sites, O^{2-} is in the *48e* site, and two *16c* sites are vacant. Table 6.1 reports atom coordinates and Wyckoff positions of the pertinent phases.

TABLE 6.1: Atom positions and corresponding Wyckoff symbols for the sites in fluorite, C-type, and fluorite with C-type setting. Notice that the 16c site is vacant in pure Y_2O_3.

	Fluorite	Fluorite with C-type setting	C-type
M1	*4a*, 0,0,0	*8b*, 1/4,1/4,1/4	*8b*, 1/4,1/4,1/4
O1	*8c*, 1/4,1/4,1/4	*48e*, 3/8,1/8,3/8	*48e*, x,y,z
M2		*24d*, 0,0,1/4	*24d*, x,0,1/4
O2		*16c*, 3/8,3/8,3/8	(*16c*, x,x,x)

Hereafter, the C-type setting is applied to the fluorite structure, so that all sites are unambiguously referred to for any composition. We take the fractional *x* coordinate of the M2 site (hereafter *x*(M2)) as the reference parameter to discuss our data, as it is the only degree of freedom of the cationic substructure: when *x*(M2)=0, the cation arrangement is the same as in fluorite, while it takes negative values in C-type.

6.3.1 Reciprocal Space Analysis

Table 6.2 outlines the results from Rietveld refinements of the XRPD patterns. All of the CYO samples were single-phase, and the average structure is *Fm*-3*m* fluorite for $\mu \leq 0.250$ and *Ia*-3 C-type for $\mu > 0.250$. The cell parameter decreases with increasing yttrium concentration owing to the lower coordination and smaller ionic radius of Y^{3+} with respect to Ce^{4+} (Shannon and Prewitt, 1969; Coduri *et al.*, 2012b).

TABLE 6.2:. Selected data from Rietveld refinements and WPPM best fits. For the μ=0.250 sample the fluorite cell parameter a=5.4032(5) Å has been doubled so as to report the value of the corresponding 2×2×2 supercell. U_{mean} is the mean square displacement (msd) parameter averaged over all the sites in each structure.

μ	0.250	0.3125	0.3438	0.4375	0.500
phase	F	C	C	C	C
a (Å)	10.8064(9)	10.7917(9)	10.7853(9)	10.7738(9)	10.759(7)
x(M2)	0	-0.0027(1)	-0.00449(9)	-0.01159(3)	-0.01497(4)
U_{mean} ($Å^2$)	0.00713(2)	0.0104(4)	0.0115(5)	0.0137(8)	0.0133(8)
R_{wp} (Rietveld)	0.0509	0.0795	0.0863	0.0652	0.0703
APDB probability		0.12(2)	0.080(4)	0.006(3)	0.0025(3)
R_{wp} (WPPM)		0.0879	0.0899	0.0619	0.0698

As shown in Figure 6.1, O2 oxygen vacancies (*16c*) and Ce/Y substitutional defects cause the *x* coordinate of the C-type M2 cation to take intermediate values between those corresponding to the end members of the solid solution, that is *x*(M2)=0 for CeO_2, and *x*(M2)~(-0.032) for Y_2O_3. Such values are consistent with the distribution of M2 cations in two different chemical environments: i) the centre of 8 equidistant occupied oxygen sites (CeO_2-like cuboids, panel A in Figure 6.1), and ii) an offset position due to two vacant O2 sites (Y_2O_3-like cuboids, panel C inFigure 6.1).

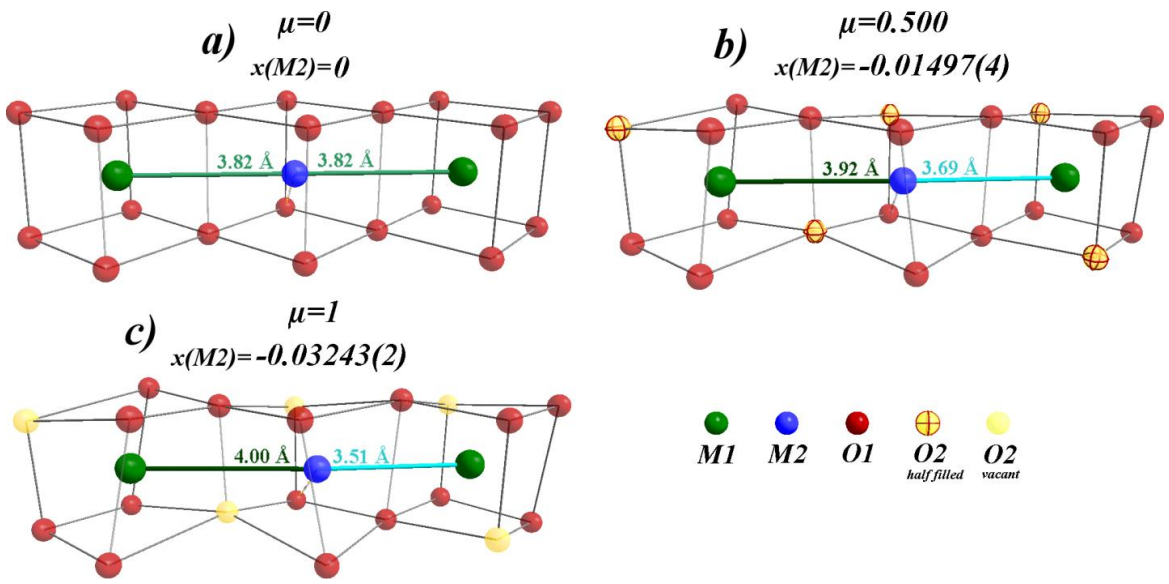

Figure 6.1: (a) CeO_2 cuboid, where the Ce^{4+} cation (M1=M2) is centred in the 8-coordinated position; (b) $Ce_{0.5}Y_{0.5}O_{1.75}$ cuboid, with 0.5 probability for a vacancy to be in the 16c site and a displaced M2 cation; (c) Y_2O_3 cuboid, in which every 16c site is empty. For each panel x(M2) yielded by the respective Rietveld fit is indicated.

The C-type structure of the samples with μ=0.313, μ=0.344, and μ=0.438 is largely distorted with respect to reference Y_2O_3. The atomic mean square displacement (msd) peaks at μ=0.438 (see Table 6.2). Since measurements were performed at 90 K, the trend in the msd parameters is due to static disorder only.

Also recalled in Table 6.2 are the results of the WPPM best fits to XRPD patterns of the μ=0.313, 0.344, 0.438 samples, obtained using PM2K. Accurate fit of the superstructure peaks were attained only by accounting for antiphase domains with dopant-like structure. Ordering of defects starting at non-equivalent sites could have yielded unmerged domains splicing at APDBs. A similar

mechanism was proposed for the Cu_3Au alloy (Scardi and Leoni, 2005). A possible relationship between the APDB probability and the spatial extent of such domains prompted us to employ PDF analysis in order to measure the domain correlation distance.

6.3.2 Real Space Analysis

The effect of composition on the cation environment is witnessed by the metal-metal (MM) nearest neighbour distances in Figure 6.2. At the lowest dopant concentration already, the single MM distance of CeO_2 (panel A in Figure 6.2) splits into a shorter (MMa ~ 3.75 Å) and a longer distance (MMb ~ 4.10 Å). The $G(r)$ of all the samples was fitted in the range between 1.5 and 5 Å. With reference to μ=0.250, μ=0.344, and μ=0.500 samples, Figure 6.2 (panels B-D) shows the $G(r)$ in the $3<r<5$ Å range as fitted by fluorite (μ=0.250) and C-type (μ=0.344 and μ=0.500) long range models. As to the μ=0.250 sample, a fluorite phase could not reproduce the MMb peak. In fact, the MMb interatomic distance tallies with an atom pair involving the C-type M2 site (see Y_2O_3 in Figure 6.2, panel H). However, in the $G(r)$ of the μ=0.344 and μ=0.500 samples, the MMb peak is equally mismatched when a C-type phase is fitted into it.

Either single phase fitted poorly the $G(r)$ in this range, as neither of them could be adapted to fit $G(r)$ peaks originating from the other phase. A reasonable solution was provided by a two-phase model, which considers the first atomic coordination shells as a combination of the fluorite and C-type chemical environments (Scavini *et al.*, 2012, Coduri *et al.*, 2012b). The fit by the two-phase model of the $G(r)$ curves is depicted in Figure 6.2 (panels E-G) together with the partial contributions from the fluorite and C-type phases. An overview of the refined parameters is given in Table 6.3 (see 'relaxed two-phase'). The change in the relative intensity and position of the MMa and MMb peaks upon increasing μ, i.e. the lesser occurrence of pairs involving Ce replaced by Y-M pairs is accounted for not only by the phase scale-factor parameters, but also by x(M2). At μ=0.250 already, the value of x(M2) refined by the two-phase model is close to that in Y_2O_3 despite the fluorite average structure of this sample.

This limited spatial extent over which C-type and fluorite interatomic distances are described by the two-phase model was defined as 'droplet' (Scavini et al., 2012a, Coduri et al., 2013a). As a result of both the tiny coherence length and random orientation, droplets average out to zero in the reciprocal space and do not constitute a secondary phase in the XRPD patterns. Thus, using a two-phase model for describing the first few atomic distances is consistent with the observation in the diffraction patterns that every CYO sample is single-phase.

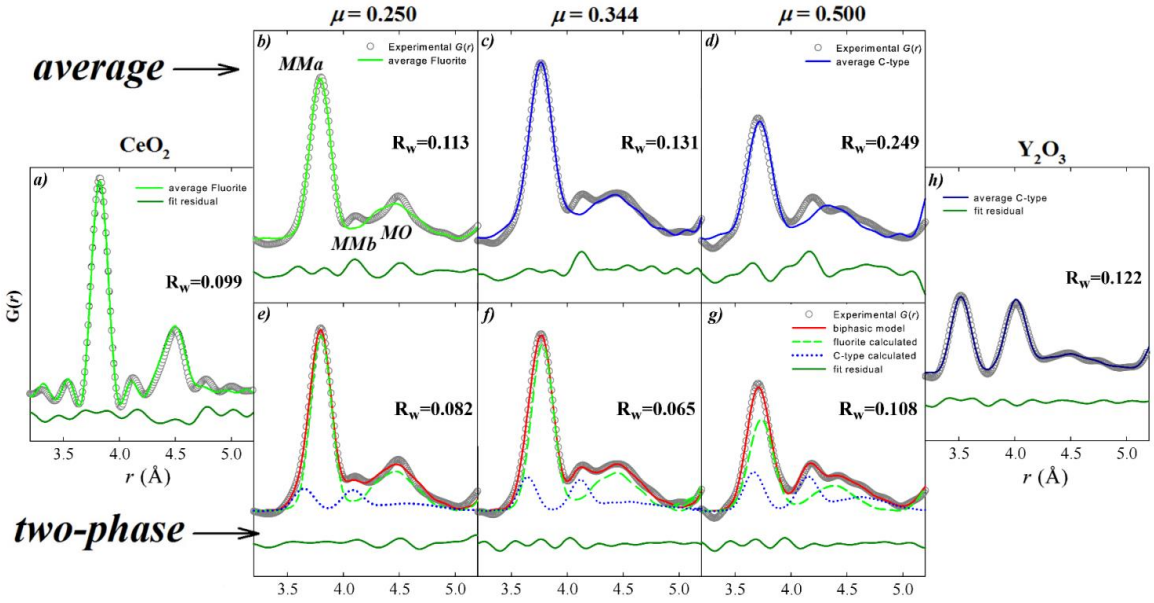

Figure 6.2:. Experimental (circles) PDF curves in the 3<r<5 Å range for samples μ=0.250, 0.344, 0.500 composition fitted above (b-d) by the fluorite (green dashed line) and C-type (blue solid line) average models; below (e-g) by the two-phase model (red solid line), to which the partial contributions of the fluorite (green dashed line) and C-type (blue dotted line) phases are also plotted. (a) Best fit based on the single-phase fluorite structure for CeO_2 (solid line); (h) Best fit based on the single-phase C-type structure for Y_2O_3. Fit residuals are indicated in each frame (solid line below the fitted curves and right-hand side of the frame).

To find out how the dopant-like atomic environment relaxes out of the first coordination shell, C-type and fluorite contributions must be probed further in the *r* space for each sample. High quality PDF data were needed to apply different models to the experimental $G(r)$ on a wide *r* range. Figure 6.3 reports the $G(r)$ up to 600 Å for the μ=0.250, μ=0.313, μ=0.344, μ=0.438, μ=0.500 samples. The slow falloff of the $G(r)$ amplitude owes to the narrow instrumental resolution function of the ID31 diffractometer. Noise in the PDF data was minimized by increasing counting statistic thanks to: i) long collection time, especially in the high-*Q* range, ii) low temperature of the experiment (90 K), which reduced thermal motion.

TABLE 6.3: Overview of the structural assessed in this work with the respective box-car refinement parameters. Scale (f,c) stands for the relative phase fractions; a_F and a_C are the cell parameter of fluorite and C-type phases, respectively; U_{iso} indicates the isotropic mean square displacement (when U_{iso} is applied to two atoms, both share the same value); U_{ii} is an anisotropic component of msd.

Model	Unrelaxed Two-phase	Relaxed Two-phase	C-type Isotropic	C-type Anisotropic	Fluorite
N. of parameters	4	7	6	10	4
Refined parameters	Overall scale Scale (f,c) U_{iso}(M1-M2) U_{iso}(O1)	Overall scale Scale (f,c) x(M2) a_F a_C U_{iso}(M1,M2) U_{iso}(O1)	Overall scale a_C x(M2) U_{iso}(M1) U_{iso}(M2) U_{iso}(O1,O2)	Overall scale a_C x(M2) U_{xx}(M1) U_{xy}(M1) U_{11}(M2) U_{22}(M2) U_{33}(M2) U_{23}(M2) U_{iso}(O1,O2)	Overall scale a_F U_{iso}(M) U_{iso}(O)

Signal-to-noise ratio and peak resolution in the $G(r)$ were satisfactory even at 400 Å. For instance, we could detect a shift in position, shape, and width of the two peaks of the doublet at ~397 Å depicted in Figure 6.3. The traces of this doublet upon increasing μ match the shortening of the interatomic distances and the increase in the DW factor at μ=0.438 worked out in reciprocal space. In the following paragraphs, structural parameters refined against $G(r)$ in successive 20 Å ranges (box-car refinements) are discussed through their trends as a function of r. A list of the refined parameters for the models introduced is given in Table 6.3.

Since it provided the best solution on the local scale, the two-phase model was tested on further interatomic distances. This was done in two different ways: i) by keeping the positional degrees of freedom (cell parameters and x(M2)) fixed, as in the local scale (r<5 Å) refinement - referred to as 'unrelaxed two-phase'; ii) by refining the positional degrees of freedom - referred to as 'relaxed two-phase'. Hereafter we will call the refined scale-factor of the C-type phase as 'C-fraction'.

Panel A in Figure 6.4 shows the unrelaxed two-phase model fitted against the $G(r)$ of the μ=0.250 sample in the 5<r<15 Å range. It can be noted from the misshapen peaks and the high fit residual that such model becomes unreliable as soon as the fluorite and C-type distances are not resolved. Actually, for r>10 Å, the $G(r)$ vectors span over the length of a droplet, and thereby they cannot be decomposed into the distinct contributions from two different coordination environments. By

letting also phase cell parameters and *x*(M2) be refined, the fit quality improved significantly (panel B in Figure 6.4), hence, the *r*-dependent structure refinement was carried up to hundreds of Å out using the relaxed model.

The trends of *x*(M2) and of C-fraction as a function of *r* obtained using the relaxed two-phase model are plotted in Figure 6.5 (panels A,B). The cell parameters of the two phases correlate strongly when refined. Notably, C-fraction for the μ=0.250 sample vanishes just over 100 Å, while the corresponding *x*(M2) value becomes unphysically negative. A similar observation can be made for the μ=0.344 sample. In particular, in this case, the C-fraction cut-off is shifted to a higher *r* value (~210 Å), but it is poorly determined as its value declines to zero very slowly. Unlike this trend, in the sample μ=0.313, *x*(M2) goes neatly to zero while C-fraction is almost constant with *r*. Despite the large fluctuation in the values due to high parameter correlation, this trend suggests a structural evolution from C-type to fluorite with increasing *r* in the samples μ=0.250, μ=0.313, μ=0.344. Indeed, the vanishing of either the C-fraction or *x*(M2) supports the only presence of the fluorite phase at high *r*. On the other hand, the μ=0.438 sample shows no fluorite character even at 500 Å. Bearing in mind that both the *x*(M2) and C-fraction parameters express the deviation from the fluorite structure, and that the two parameters exhibit a major negative correlation, we derived a C-type-to-fluorite order parameter by multiplying x(M2) by C-fraction through the whole refinement range. The *x*(M2)×C-fraction parameter, plotted in Figure 6.5 (panel C), becomes zero at *r*~120 Å, *r*~110 Å, and *r*~200 Å, respectively, for μ=0.250, μ=0.313, and μ=0.344. As expected, at μ=0.438, the x(M2)×C-fraction parameter does not approach zero at any distance.

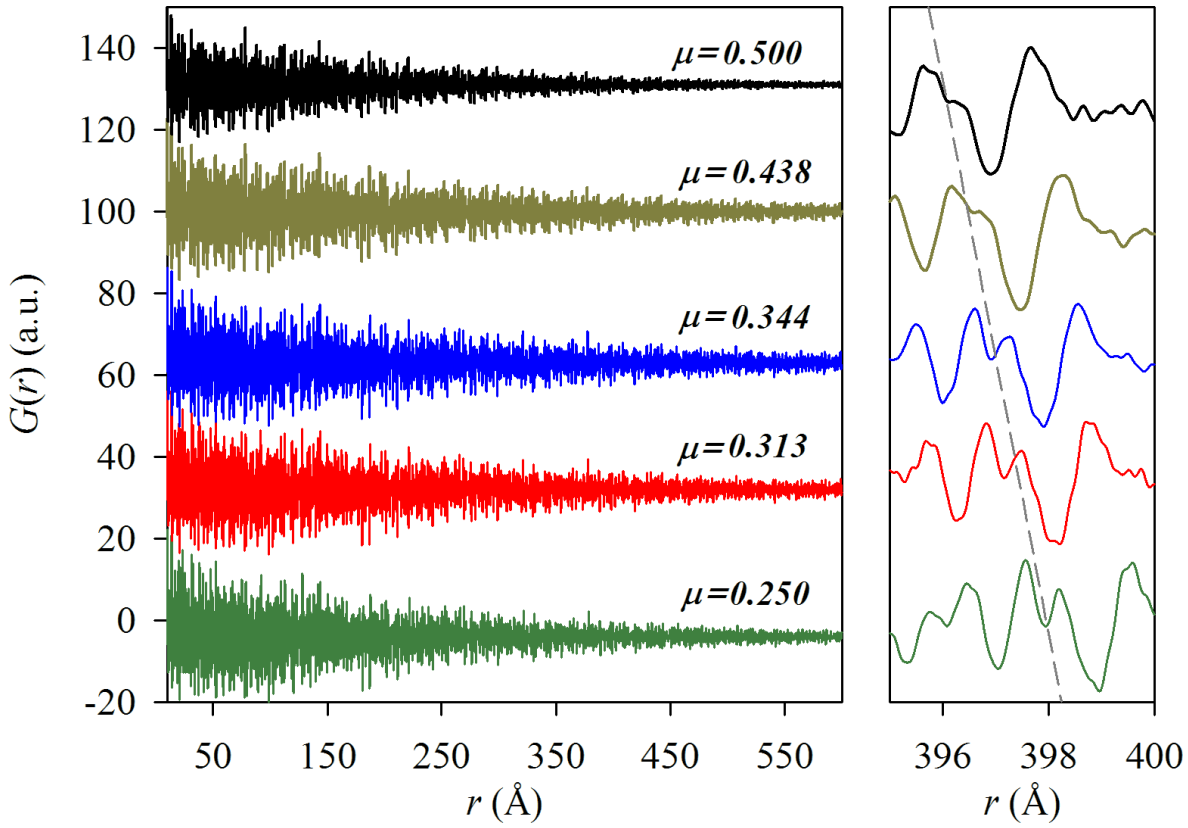

Figure 6.3: Experimental G(r) curves up to r=600 Å (left) for the CYO samples. Details of the curves in the range 395 < r < 400 Å are also shown (right). The dashed line is a guide to the eye tracing the peak position.

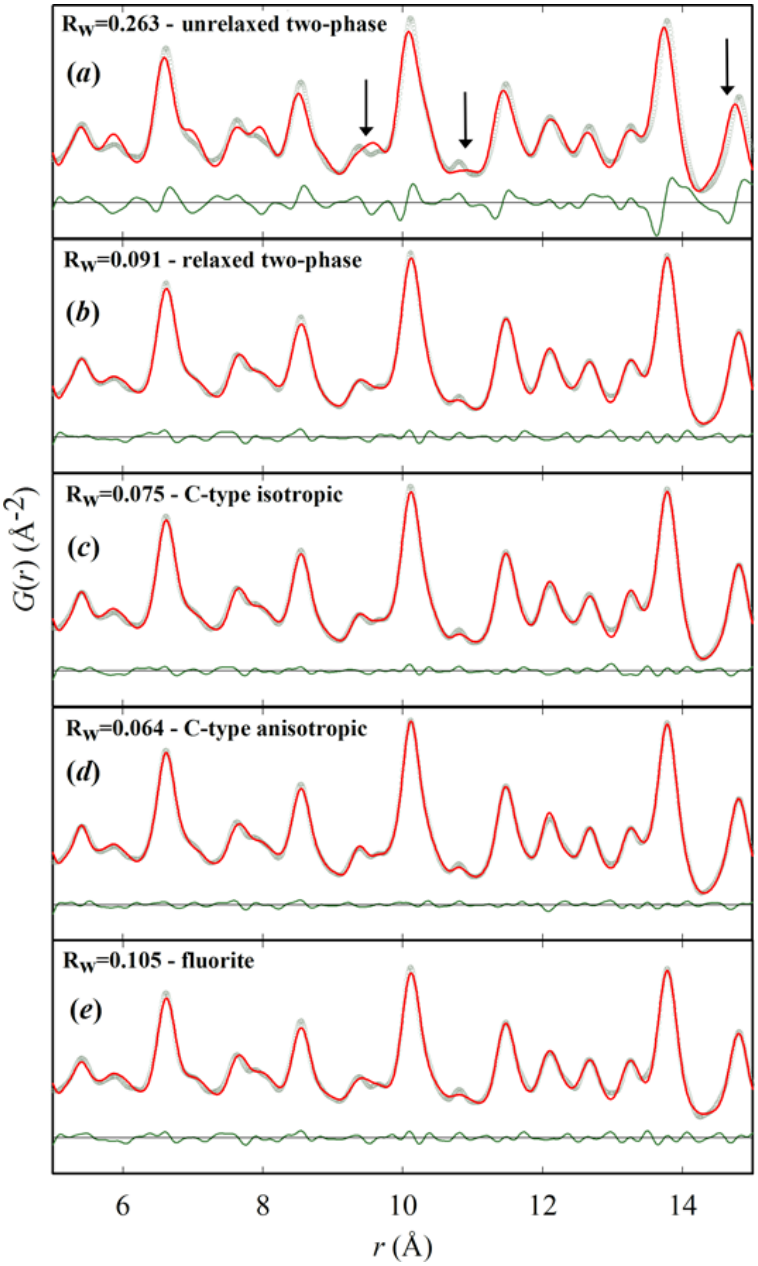

Figure 6.4: Experimental (circles) and model fitted PDF curves in the 5<r<15 Å range for the sample with μ=0.250 composition: (a) unrelaxed two-phase model; (b) relaxed two-phase model; (c) isotropic C-type model; (d) anisotropic C-type model; (e) fluorite model. Below each fitted curve the fit residual (green solid line) is shown along with its zero-point line (dotted line).

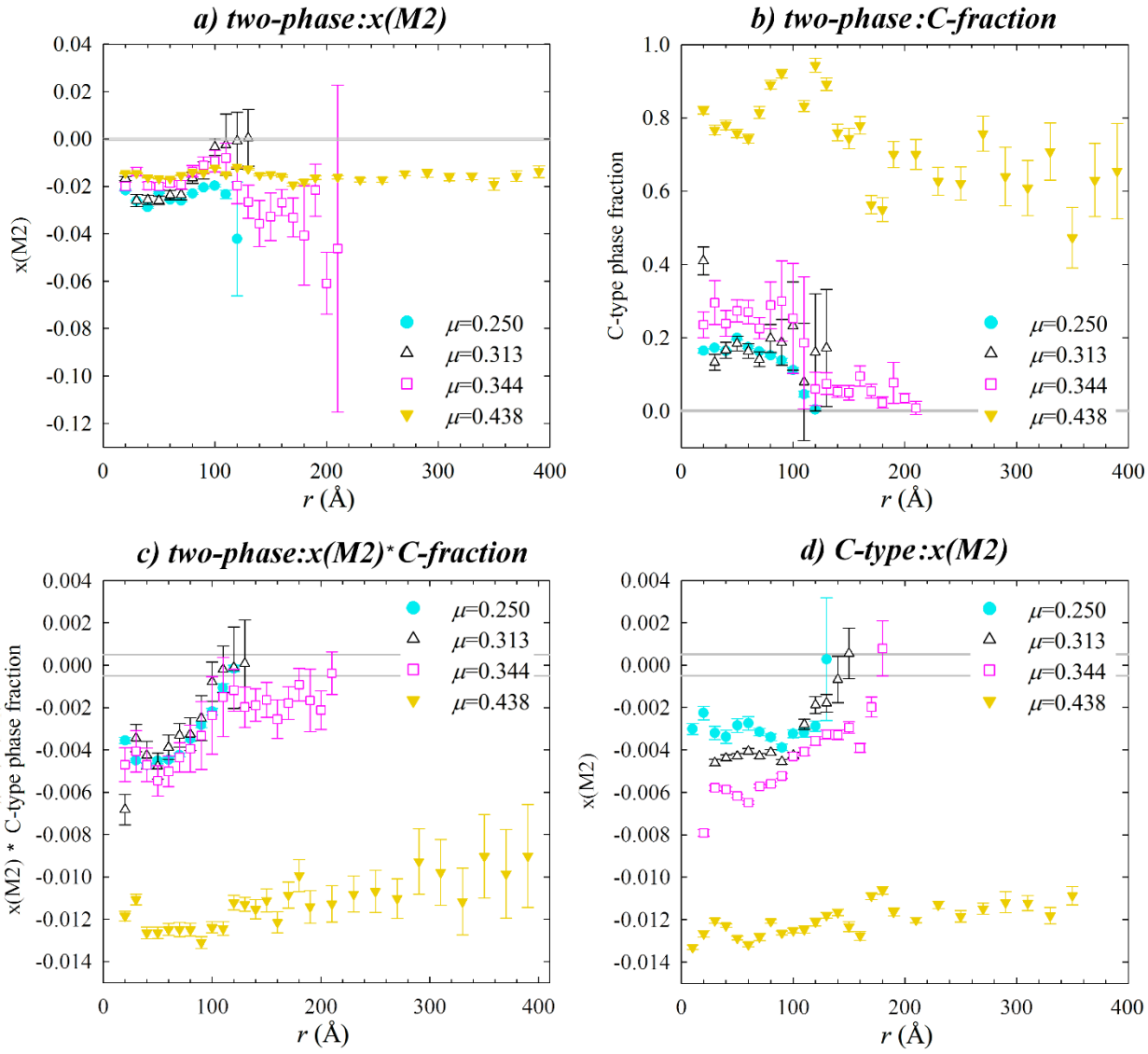

Figure 6.5: Plots of the refined parameters versus r for the samples μ=0.250, μ=0.313, μ=0.344, μ=0.438 as from: (a-c) the relaxed two-phase model, (d) the isotropic C-type model. Horizontal solid lines in the plots indicate x(M2)±0.004 as a reference.

In the refinements against the relaxed two-phase model, the C-type cell parameter converged to a value twice the fluorite cell parameter. Therefore, a meaningful description of the structure could be achieved using a single C-type model (Figure 6.4, panel C), thereby cutting the correlation between fluorite and C-type structural parameters. In the C-type model, site occupancy factors of Ce and Y atoms mirror the sample composition, and the *16c* site is filled accordingly. As a result,

the *x*(M2) parameter returned by the refinement was averaged over the two unalike positions of Ce and Y in their chemical environment, thus including the relative weights of the fluorite and C-type phases. While this was not satisfying on the local scale, it afforded a good fit at the nanometre scale.

Lower fit residual was achieved as compared to the relaxed two-phase model. The cell parameters evolve negligibly along *r* in all of the samples, and closely resemble the respective values from Rietveld refinements: *a*~10.807, *a*~10.787, *a*~10.780, and *a*~10.769 Å for μ=0.250, μ=0.313, μ=0.344, and μ=0.438. No correlations involving *x*(M2) were found and, therefore, the C-type domain size could be accurately estimated by only using the *r*-dependence of *x*(M2).

The trends of *x*(M2) vs *r* yielded by the C-type model are plotted in panel D of Figure 6.5. For μ=0.250, μ=0.313, and μ=0.344, *x*(M2) averages out to zero at *r*~120 Å, *r*~140 Å, and *r*~180 Å, respectively. On the contrary, μ=0.438, *x*(M2) slopes in the range -0.014<*x*(M2)<-0.010 but does not become zero within a range of 500 Å. This result points out that the C-type phase virtually achieves long-range coherence at μ=0.438, whereas the same ordering is confined in 100-200 Å-sized domains at lower dopant concentrations. As can be noticed in Figure 6.5 (panel D), the value of *x*(M2) within the domain gets more negative the higher the Y concentration in the sample. With increasing μ, fewer fluorite-like interatomic distances in the *G*(*r*) curve must be fitted by the C-type phase. Accordingly, the refined *x*(M2) parameter resembles more closely the value of *x*(M2) in Y_2O_3.

A possible improvement of the fitting model could be achieved by using a C-type phase along with anisotropic displacement parameters. Strong anisotropic static disorder is indeed typical of doped ceria compounds (Scavini *et al.*, 2012, Coduri *et al.*, 2013b). Panel D in Figure 6.4 shows the *G*(*r*) fit by this model in the 5<*r*<15 Å range for the μ=0.250 composition. Lower fit residual with respect to the previous C-type model (i.e. isotropic C-type) was attained using anisotropic thermal factors (i.e. anisotropic C-type). The refined cell parameter matched the value obtained by the isotropic C-type model for any composition and *r* range.

For the μ=0.344 and μ=0.438 samples, the *r*-dependence of *x*(M2) parameter followed almost the same trend yielded by the isotropic model. Conversely, for the μ=0.250 and μ=0.313 samples a lower *x*(M2) cut-off resulted (~40 Å) which totally disagrees with isotropic model results. This discrepancy is explained by the strong correlation between the *x*(M2) position and the U_{11} parameter, which made this model inconsistent. By using the anisotropic C-type, the uncertainties on *x*(M2) were greater by an order of magnitude than those found using the isotropic C-type. For these reasons, we retained the isotropic C-type as the reference model for estimating domain size.

By inspecting the refined C-type phase of the samples μ=0.250, μ=0.313, μ=0.344, it must be pointed out that the uncertainty on x(M2) increased considerably as x(M2) approaches zero. Such an increase suggests that the $G(r)$ might be fitted more accurately in the r range encompassing the domain boundary and further in r. Thus, a simple fluorite structural model was fitted against the $G(r)$ up to 400 Å, so that the refined C-type and fluorite phases could be compared throughout r.

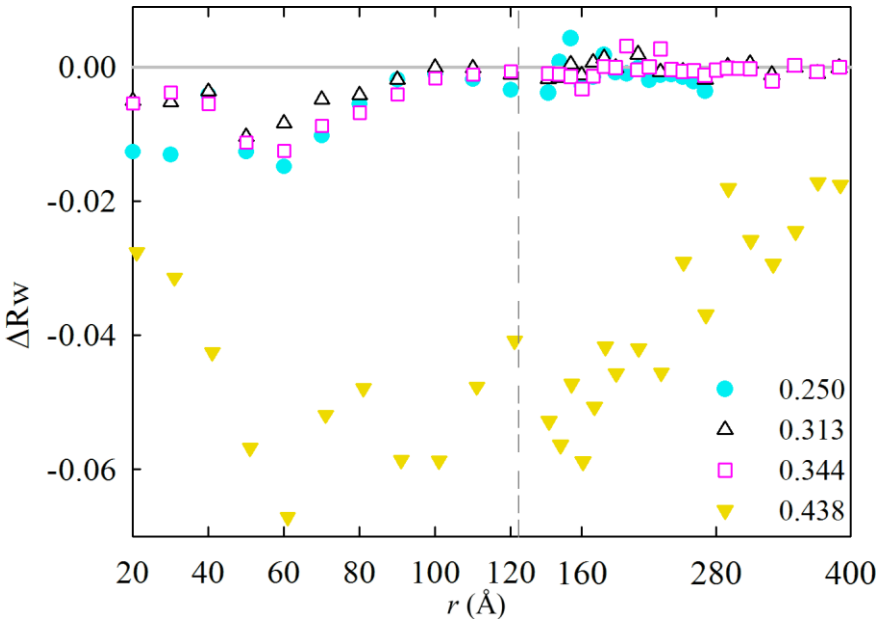

Figure 6.6: Plot of the difference, ΔRw, between the fit residual as from the C-type isotropic model and from the fluorite model as a function of r for the samples μ=0.250, μ=0.313, μ=0.344, μ=0.438. On the left of the dashed vertical line the r axis scale is expanded.

The difference, ΔRw[=Rw(C-type)- Rw(fluorite)], between the residual of fit by C-type and that by fluorite is plotted in Figure 6.6 for the four compositions μ=0.250, μ=0.313, μ=0.344, and μ=0.438. The ΔRw difference is negative in the samples μ=0.250, μ=0.313, μ=0.344 within the respective domain size, indicating the better agreement of the C-type model with the observed $G(r)$. The two fit residuals cancel each other out approximately at the domain boundary, then, ΔRw oscillates around zero in the further range of r, at which the refined phases virtually equate to each other. In fact, when a C-type phase was fitted against $G(r)$ in a r range outside the C-type domain, x(M2) equalled 0 within the uncertainty. In the μ=0.438 sample, the fit residuals never cross in the whole range of r, reflecting the trend of x(M2) versus r.

Finally, the respective best fits in the range of interatomic distances between 390 and 410 Å are displayed in Figure 6.7 for all the samples. Although the absolute $G(r)$ intensity is decreased with respect to the local scale due to the instrumental contribution (see Figure 6.3), no noteworthy fit residual was observed. The randomly distributed difference curve accounts for some noise, at a minimum, though, thanks to the high counting statistics. The good quality of the fit further supports the goodness of our approach.

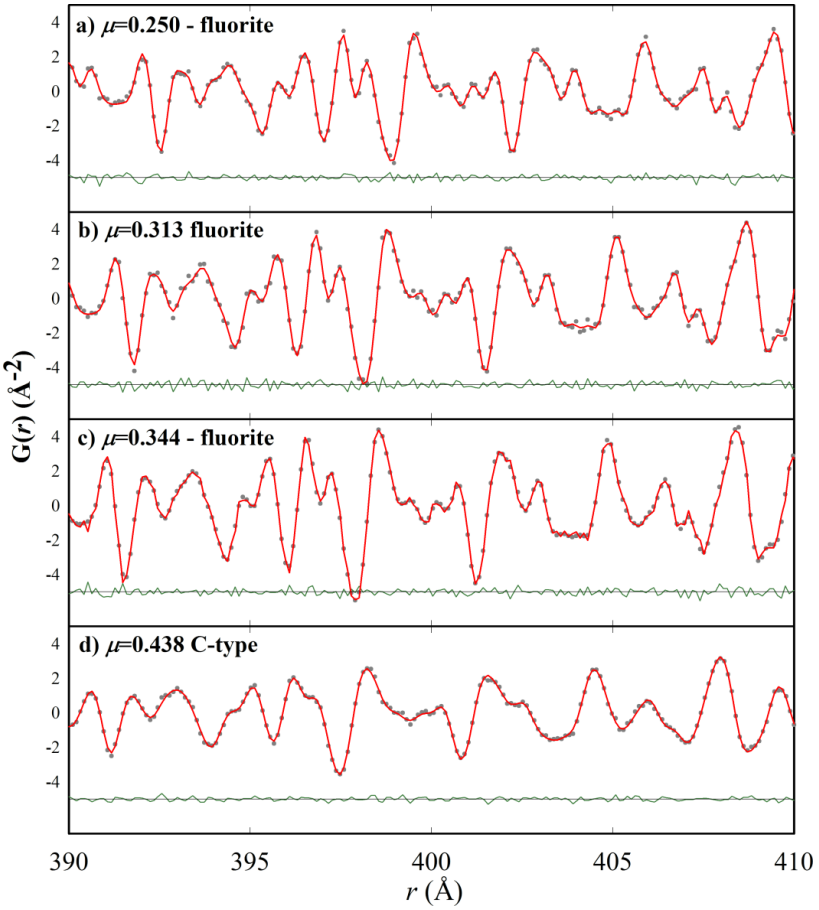

Figure 6.7: Experimental (circles) PDF curves in the 390<r<410 Å range for the samples (a) μ=0.250, (b) μ=0.313, (c) μ=0.344, (d) μ=0.438 with the corresponding calculated profile (solid red line) based on the respective best fitting model. Below each fitted curve the fit residual (solid green line) is shown along with its zero-point line (dotted line).

6.4 Conclusion

PDF analysis of $Ce_{1-\mu}Y_{\mu}O_{2-\mu/2}$ samples with μ=0.250, μ=0.313, μ=0.344 and μ=0.438 composition was carried out. Several models conceiving the structural relationship between fluorite (CeO_2-like) and C-type (Y_2O_3-like) phases were evaluated through box-car refinements: i) a two-phase model (i.e. coexisting Y_2O_3-like and CeO_2-like phases), in which cell parameters and the *x*(M2) cation coordinate were either fixed or free to refine. ii) a single C-type phase, refining either isotropic or anisotropic displacement parameters. iii) a single fluorite phase.

The model best describing the *G*(*r*) curves up to high *r*, attaining both accurate fits and meaningful structural parameters, is a simple C-type phase with isotropic displacement parameters. Nanometre-sized dopant domains were determined as the range in real space in which the C-type phase best fitted the experimental *G*(*r*). Gradual transformation of C-type into fluorite was observed with increasing *r* in the μ=0.250, μ=0.313, μ=0.344 samples. Different models, however, generally agree in the estimate of the C-type domain sizes, that is, nearly 100-140 Å for μ=0.250 and μ=0.313, ~180-200 Å for μ=0.344, and in excess of 500 Å for μ=0.438.

References

Balazs, G. B., & Glass, R. S. (1995). AC impedance studies of rare earth oxide doped ceria. Solid State Ionics, 76(1), 155-162.

Billinge, S. J., & Levin, I. (2007). The problem with determining atomic structure at the nanoscale. Science, 316(5824), 561-565.

Coduri, M., Scavini, M., Allieta, M., Brunelli, M., & Ferrero, C. (2013). Defect structure of Y-doped ceria on different length scales. Chemistry of Materials, 25(21), 4278-4289.

Coduri, M., Brunelli, M., Scavini, M., Allieta, M., Masala, P., Capogna, L., & Ferrero, C. (2012). Rare Earth doped ceria: a combined X-ray and neutron pair distribution function study. Zeitschrift für Kristallographie Crystalline Materials, 227(5), 272-279.

Coduri, M., Scavini, M., Allieta, M., Brunelli, M., & Ferrero, C. (2012). Local disorder in yttrium doped ceria ($Ce_{1-x}Y_xO_{2-x/2}$) probed by joint X-ray and Neutron Powder Diffraction. In Journal of Physics: Conference Series (Vol. 340, No. 1, p. 012056). IOP Publishing.

Coduri, M., Scavini, M., Brunelli, M., & Masala, P. (2013). In situ pair distribution function study on lanthanum doped ceria. Physical Chemistry Chemical Physics, 15(22), 8495-8505.

Farrow, C. L., Juhas, P., Liu, J. W., Bryndin, D., Božin, E. S., Bloch, J., & Billinge, S. J. L. (2007). PDFfit2 and PDFgui: computer programs for studying nanostructure in crystals. Journal of Physics: Condensed Matter, 19(33), 335219.

Foschini, C. R., Souza, D. P. F., Paulin Filho, P. I., & Varela, J. A. (2001). AC impedance study of Ni, Fe, Cu, Mn doped ceria stabilized zirconia ceramics. Journal of the European Ceramic Society, 21(9), 1143-1150.

Gateshki, M., Niederberger, M., Deshpande, A. S., Ren, Y., & Petkov, V. (2007). Atomic-scale structure of nanocrystalline CeO_2–ZrO_2 oxides by total x-ray diffraction and pair distribution function analysis. Journal of Physics: Condensed Matter, 19(15), 156205.

Goodenough, J. B. (2003). Oxide-ion electrolytes. Annual review of materials research, 33(1), 91-128.

Gregori, G., Rahmati, B., Sigle, W., Van Aken, P. A., & Maier, J. (2011). Electric conduction properties of boron-doped ceria. Solid State Ionics, 192(1), 65-69.

Kim, N., & Stebbins, J. F. (2007). Vacancy and cation distribution in yttria-doped ceria: An ^{89}Y and ^{17}O MAS NMR study. Chemistry of Materials, 19(23), 5742-5747.

Larson, A. C., & Von Dreele, R. B. (1986). GSAS General Structure Analysis System, Report LAUR 86-748. Los Alamos National Laboratory, Los Alamos, NM..

Leoni, M., Confente, T., & Scardi, P. (2006). PM2K: a flexible program implementing Whole Powder Pattern Modelling. Z. Kristallogr. Suppl, 23, 249-254.

Minervini, L., Zacate, M. O., Grimes, R. W. (1999). Defect cluster formation in M_2O_3-doped CeO_2. Solid State Ionics, 116(3–4), 339-349.

Mittemeijer, E. J., & Scardi, P. (Eds.). (2013). Diffraction analysis of the microstructure of materials (Vol. 68). Springer Science & Business Media.

Ou, D. R., Mori, T., Ye, F., Takahashi, M., Zou, J., & Drennan, J. (2006). Microstructures and electrolytic properties of yttrium-doped ceria electrolytes: Dopant concentration and grain size dependences. Acta Materialia, 54(14), 3737-3746.

Park, Y. S., Sohn, H. Y., & Butt, D. P. (2000). Thermal removal of gallium from gallia-doped

ceria. Journal of nuclear materials, 280(3), 285-294.

Pechini, M. P. (1967). U.S. Patent No. 3,330,697. Washington, DC: U.S. Patent and Trademark Office.

Qiu, X., Thompson, J. W., & Billinge, S. J. (2004). PDFgetX2: a GUI-driven program to obtain the pair distribution function from X-ray powder diffraction data. Journal of Applied Crystallography, 37(4), 678-678.

Scardi, P., & Leoni, M. (2005). Diffraction whole-pattern modelling study of anti-phase domains in Cu 3 Au. Acta materialia, 53(19), 5229-5239.

Scavini, M., Coduri, M., Allieta, M., Brunelli, M., & Ferrero, C. (2012). Probing Complex Disorder in $Ce_{1-x}Gd_xO_{2-x/2}$ Using the Pair Distribution Function Analysis. Chemistry of Materials, 24(7), 1338-1345.

Toby, B. H. (2001). EXPGUI, a graphical user interface for GSAS. Journal of applied crystallography, 34(2), 210-213.

Yamazaki, S., Matsui, T., Ohashi, T., & Arita, Y. (2000). Defect structures in doped CeO_2 studied by using XAFS spectrometry. Solid State Ionics, 136, 913-920.

Conclusion

Pr-doped strontium titanate (SPTO) is a perovskite with a high-symmetry ground state and a large mismatch between the Sr/Pr ionic radii, and, thus, a model system to study the relation between locally broken symmetry and microscopic polarization. This has been studied predominantly by one technique, powder diffraction, albeit in multiple, complementary ways. Thanks to exceptional counting statistics and angular resolution of synchrotron data, Rietveld analysis revealed tiny distortions in SPTO with respect to undoped strontium titanate, which allowed drawing an accurate phase diagram. While the crystallographic phase of SPTO is increasingly antiferrodistortive (AFD), rotational at higher Pr concentrations, analysis of the pair distribution function (PDF) showed a large local AFD distortion that could be seen as the effect of a ferroelectric (FE) mode meddling in the local structure.

The high sensitivity of neutron scattering to oxygen nuclei added insight into a distortion tangled with the motion of oxygen atoms; this is why selected SPTO samples were measured using spallation neutron radiation. In a robust approach, the same neutron data were analysed in reciprocal space and in real space, respectively, for Rietveld and PDF analysis. While the former confirmed the AFD long-range phase seen in X-ray data, PDF modelling by Reverse Monte Carlo simulations revealed disordered regions around Pr atoms compatible with microscopic polarization, since orthorhombically distorted PrO_{12} polyhedra force the surrounding octahedra to rotate out of axis.

The last two chapters introduced two further approaches to PDF analysis. The first one involves a symmetry decomposition of the cubic perovskite structure of $SrTiO_3$, yielding 120 possible positional degrees of freedom that were used as atomic positional parameters of a *P*1 supercell, refined against the neutron PDF of undoped $SrTiO_3$ and converted to amplitudes of soft modes. These parameters were grouped by the symmetry of the corresponding distortion (i.e. irreducible representation) and refined in turn, evidencing the highest-likelihood static and dynamic modes in the local structure of $SrTiO_3$. The second and last one concerns the spatial extent of dopant-rich domains in CeO_2. Crystalline CeO_2 is known to have a cubic fluorite phase with extremely high spatial coherence. Yttrium introduced as a dopant has a tendency to cluster into lower-symmetry ‘droplets’, signalled by the displacement of a set of cations and which, remarkably, show up in the PDF of the doped compounds even at distances beyond 100 Å. Structure refinements to high-*Q*-resolution and high-*r*-resolution X-ray PDF allowed finding the range of interatomic distances at which dopant-rich droplets dissolve into the CeO_2-like fluorite matrix.

Model fitting, as carried out by the PDFFit/PDFGui code, is the most direct method to test the agreement between model and data and to get structural parameters. The user normally has a set of likely models that should be tried; prior knowledge of the material is generally useful. A strength of this method is the parametrisation of the basic instrumental contributions to the PDF. It is customary to analyse a standard material before the actual samples in order to get the right parameters for intensity damping and peak broadening. Provided that the phase(s) fitting the PDF is (are) good enough, the immediacy of small-box models makes it easy to obtain octahedral tilts, atom displacements, or thermal motions for a set of temperatures and compositions. On the other hand, it is impractical to refine complex models, like a fully parametrised monoclinic phase or more than two phases but the simplest. A successful refinement owes much to the way the least-squares problem is set up. Parameters with a similar effect on the calculated PDF can be fatally correlated; and parameters with little weight (e.g. O atoms in X-ray PDF or very small atom displacements) can stray from reasonable values.

By contrast, **Reverse Monte Carlo** (RMC) is capable of handling any kind of distortion and is completely unbiased by symmetry assumptions. The large-box models used have no internal symmetry, so that atomic positions are not correlated by anything but features in the data. Moves to the atoms are random and thus able to accommodate any blip or asymmetry related to structure distortion. Besides PDF, the the method as implemented in the RMCProfile code is able to model the total scattering function, $F(Q)$, and Bragg peaks. Therefore, the RMC configurations are likely to give the best possible fit to the data and are potentially sensitive to any distortion in the material. High sensitivity can be also a problem: in the case of experimental noise (termination ripples, low count rates, etc), some atom positions will try to accommodate the spurious signal as well as the meaningful part of the data. Since there is no explicit correction for instrumental sources of error, the calculated function is based solely on the positions of the atoms in the large box. Thus, the final model inevitably reflects some problems with the data. Additionally, being a very general (thus powerful) method, RMC has no ad-hoc procedures. This means that some necessary ‘soft’ constraints, like first-neighbour distance windows and the weights of different function datasets, must be adjusted by trial and error.

Symmetry-adapted refinements, based on the PDFFit least-squares engine, try to get the best of both worlds. Refinement is pseudo-random, in that the starting model has no symmetry and is repeated an arbitrary number of cycles with random starting values, but it also gives quantitative results, since it contains a single distortion related to a precise symmetry mode. It also uses the instrument parametrisation of PDFFit. The high level of abstraction of this method, however, could lead the user to overlook data quality when interpreting the solution.

Acknowledgments

This work owes much to the contributions of other people.

I am greatly indebted to my supervisor, Dr. Marco Scavini, for a number of things from laboratories to beamtime, from discussions to collaborations. Not least, for proving that good work can start as a casual chat. I also acknowledge the people from the Department of Chemistry in Milan who were of great help and support. In alphabetical order, Dr. Mattia Allieta, Mr. Dario Bozzetti, Ms. Serena Cappelli, Dr. Davide Ceresoli (from CNR-ISTM), and Dr. Paolo Masala.

At the ESRF in Grenoble, Dr. Michela Brunelli provided excellent support during beamtime and kindly hosted me at the Swiss-Norwegian BeamLines for a long and fruitful time in 2016. At the ID22 beamline, Dr. Mauro Coduri gave invaluable help on everything X-ray. Also, Dr. Andy Fitch, Dr. Carlotta Giacobbe, and Dr. Christina Drathen made many of these measurements possible. Also, Dr. Claudio Ferrero offered precious technical support during data analysis.

I am indebted to Dr. Matthew Tucker and Dr. David Keen from the GEM diffractometer at ISIS. Not only my understanding of neutrons owes massively to them and they made all these neutron measurements possible, but they also retrieved past data that make up most of the chapter on symmetry-adapted refinements.

I also wish to thank Dr. Mark Senn and Prof. Andrew Goodwin of the Inorganic Chemistry Laboratory at Oxford University. To benefit from their tremendous knowledge was a singular opportunity, only second to benefiting from their superb hospitality for a few weeks during the second half of 2016.

Finally, I am grateful to the Italian Ministry of Education and Research, which provided me with the financial resources to carry out this project, and to Prof. Emanuela Licandro at the University of Milan, the coordinator of the Ph.D. course.